The large-scale radio continuum environment of the prototypical binary active galactic nucleus system, NGC 6240

By

Isaac Selaelo Magolego

UNIVERSITEIT VAN PRETORIA
UNIVERSITY OF PRETORIA
YUNIBESITHI YA PRETORIA
Denkleiers • Leading Minds • Dikgopolo tša Dihlalefi

Department of Physics
University of Pretoria

Submitted in partial fulfilment of the requirements for the degree of Master of Science (MSc) in Physics in the Faculty of Natural and Agricultural Sciences.

August 22, 2022

Supervisor: Prof. Roger Deane and Dr. Kshitij Thorat

UNIVERSITY OF PRETORIA

Abstract

Faculty of Natural and Agricultural Sciences
Department of Physics

Master of Science (MSc) in Physics

The large-scale radio continuum environment of the prototypical binary active galactic nucleus system, NGC 6240

by Isaac Selaelo Magolego

Supervisor: Prof. Roger Deane and Dr. Kshitij Thorat

Diffuse radio sources are best studied at low radio frequencies ($\lesssim$ 1 GHz) as they typically have steep radio spectra, resulting in higher flux densities at lower frequencies. However, this requires high surface brightness sensitivity, which is challenging at low frequencies due to a variety of instrumental and propagation effects. Two diffuse radio sources of interest are radio halos and relics, which are typically found in the vicinity of galaxy clusters. The origin of radio halos have been historically debated between the following models: hadronic (secondary electron) and turbulent re-acceleration models, whereas that of radio relics is believed to arise from outgoing merger shocks. Due to the exceptional sensitivity of MeerKAT, we are able to explore diffuse radio sources with high fidelity. In this thesis we report the discovery of the extended diffuse radio continuum around NGC 6240 at redshift of $z = 0.0245$ using MeerKAT data at 1.28 GHz. We discuss the morphology, location, and linear size of the extended diffuse continuum, however, due to technical issues, we could not classify the nature of the extended diffuse emission. We detect what we argue to be a radio shock with an arc-like morphology with a radio power of 6.3×10^{22} W Hz^{-1} at 1.28 GHz. Our results show that even in low mass systems, MeerKAT is capable of detecting radio relic-like components. The combined analysis of this extended radio continuum halo together with that of the HI, cold molecular gas, and ionized gas will lead to a more holistic understanding of NGC 6240.

Keywords: diffuse emission: radio halos, radio relics, re-acceleration, merger shocks.

Declaration of Authorship

I, Isaac Selaelo Magolego, declare that the thesis, which I hereby submit for the degree of MSc in Physics at the University of Pretoria, is my own work and has not previously been submitted by me for a degree at this or any other tertiary institution.

Signature: Isaac Magolego

Date: 22/08/2022

Acknowledgements

I would like to thank both my supervisors, Prof Roger Deane and Dr Kshitij Thorat, for their counsel, encouraging efforts and positive feedback throughout this project. I hope to engage in some interesting projects with you both in the future.

To Boitumelo Mocumi, I wish to convey my special appreciation for your support, encouragement and taking interest in my work. To Leon Mtshweni, thank you for teaching me everything I needed to know about UP Astro group, particularly the use of ilifu cloud computing and some coding lessons.

To Dr Buyisiwe Sondezi, Prof Aletta Prinsloo and Prof Chris Engelbrecht, my lecturers and mentors at the University of Johannesburg. Thank you for inspiring and encouraging me to go further with my studies in Astrophysics.

Finally, I would like to thank both my parents, who have always supported and encouraged me throughout my academia years. Much love for you guys.

A special thanks to the South African Radio Astronomy Observatory (SARAO) for funding this project throughout. The ilifu/IDIA cloud computing facility is also hereby acknowledged, for providing necessary tools to complete this project.

Contents

List of Figures

List of Tables

List of Abbreviations

AGN	**A**ctive **G**alactic **N**uclei
ULIRGs	**U**ltra-luminous **I**nfrared **G**alaxies
VLA	**V**ery **L**arge **A**rray
MERLIN	**M**ulti-Element **R**adio **L**inked **I**nterferometer **N**etwork
UFO	**U**ltra-fast **O**utflows
Fe	**I**ron
HI	**N**eutral **H**ydrogen
BCG	**B**rightest **C**luster **G**alaxy
CR	**C**osmic **R**ays
ICM	**I**ntra-cluster **M**edium
DSA	**D**iffuse **S**hock **A**cceleration
VLBI	**V**ery **L**ong **B**aseline **I**nterferometry
EVN	**E**urope **V**LBI **N**etwork
ALMA	**A**tacama **L**arge **M**illimeter **A**rray
LOFAR	**L**ow **F**requency **A**rray
SKA	**S**quare **K**ilometre **A**rray
CASA	**C**ommon **A**stronomy **S**oftware **A**pplications
1GC	**F**irst **G**eneration **C**alibration
2GC	**S**econd **G**eneration **C**alibration
MS	**M**easurement **S**et
MFS	**M**ulti **F**requency **S**ynthesis
HST	**H**ubble **S**pace **T**elescope
ACIS-S	**A**dvanced **C**CD **I**maging **S**pectrometer
CALDB	**C**alibration **D**atabase
SARAO	**S**outh **A**frican **R**adio **A**stronomy **Observatory**
PFS	**P**oint **S**pread **F**unction
CARTA	**C**ube **A**nalysis and **R**endering **T**ool for **A**stronomy
WCS	**W**orld **C**oordinate **S**ystem
IC	**I**nverse **C**ompton
CMB	**C**osmic **M**icrowave **B**ackground
FR-I	**F**anaroff-Riley **1**
Myr	**M**illion **Y**ears
Gyr	**G**iga **Y**ears
MHD	**M**agneto-hydrodynamical

Chapter 1

Introduction

1.1 Galaxy formation and evolution

Over the years studies have shown that galaxies evolve through minor and major mergers, as well as interacting with galaxies in close proximity (Barnes and Hernquist, 1992). Bower et al. (2016) reported that there are two distinct types of galaxies, namely: active, blue-sequence galaxies that form young stars rapidly, and passive red-sequence galaxies in which star-formation has nearly entirely ceased. Blue-sequence is normally followed by low mass galaxies with a tense, nearly direct, correlation between star formation rate and stellar mass (Brinchmann et al. 2004, Tacconi et al. 2020), whereas red-sequence is followed by massive galaxies with nearly invisible levels of star formation (Bower et al., 1992).

1.2 Basic overview of the big bang

For almost a century The Big Bang Theory has been used to describe the beginning of the universe. The Big Bang Theory states that all the matter in the Universe, current and past, came into existence simultaneously, approximately 13.8 Gyr ago (e.g., Steiner 2006). It was around the 1950s and 1960s when The Big Bang (hot) model was gradually developed. The model was supported by the studies of the cosmic helium abundance (Hoyle and Tayler, 1964), where they found out that the abundance of helium is everywhere by mass ($\sim 1/3$ that of the hydrogen). Then the model was further supported by the studies of the network of nuclear reactions (Wagoner et al., 1967) and also by the detection of the cosmic microwave background (Penzias and Wilson, 1965; Dicke et al., 1965; Hirschmann, 2011).

1.3 Dark matter halos and galaxy components

Cosmological models have shown that approximately $5/6$ of the mass contained by our universe is made of dark matter (Planck Collaboration et al., 2016). This dark matter is believed to form the skeleton on which galaxies form, evolve and merge (Wechsler and Tinker, 2018). Cosmological models suggest that dark matter and gas were well blended initially; as the universe evolved , gas dissipated and fell to centrals of dark matter halos (Wechsler and Tinker, 2018). The power spectrum of matter shows that first formation is that of small objects, and halos should grow and merge gradually, as the galaxies inside these continues to form stars and to grow via merging, because their dark matter halos merge (Wechsler and Tinker, 2018).

1.4 Feedback processes and ionized IGM/CGM

It is believed that after the activity of an AGN is triggered and the SMBHs reach a certain mass (Ishibashi and Fabian, 2012), they release energy to the local medium through jets, winds and radiation, which can enrich the circum-galactic medium (CGM; Rubinur et al. 2019b). The winds also trigger star-formation beyond the Active Galactic Nuclei (AGN) by shocking gas and suppress gas infall by blowing out gas, and this is collectively called AGN feedback (Rubinur et al., 2019b). AGN outbursts found in smaller dark matter halos (with shallower gravitational potentials) are believed to generate a huge impact on the intergalactic medium (IGM; Pandge et al. 2019). The feedback effect of AGN-driven outflows is now incorporated into galaxy evolution models and has been used to describe the relative dearth of galaxies with high mass (Benson et al., 2003; Bower et al., 2006), as well as the association between the properties of the host galaxy and black hole mass (Fabian, 1999; Di Matteo et al., 2005; Tadhunter, 2008).

1.5 Observations of IGM/CGM

Zwicky (1957) and Karachentsev and Lipovetskii (1969) were the first to point out the presence of dust in the IGM, when observing the extinction of distant clusters behind rich galaxy clusters. Ever since then, galaxy clusters have been used as cosmological guidelines to indicate the previous history of IGM (Borgani et al., 2008; Kaastra et al., 2008). A major premise of galaxy formation theory has long been the existence of extensive gaseous halos around galaxies, as a result of collapsing gas in hierarchical build-up of structure (White and Rees, 1978; Machado et al., 2018). It is believed that the large-scale IGM and ISM are linked together by the CGM (Machado et al., 2018). Circumgalactic medium plays two roles in the chemical history of galaxies: it acquires the enhanced matter that was ejected in the form of outflows, and also functions as a tank of fuel for upcoming star-formation (Machado et al., 2018).

1.6 Galaxy mergers and dual AGN

Over the years cosmological theory and models have indicated that gas accretion on SMBHs can be triggered by mergers, which lead to the formation of AGN pairs or sometimes AGN-star forming nuclei pairs (Rubinur et al., 2019a). The AGN pairs are called dual AGN when the separation between them ranges from approximately 0.1 to 10 kpc, and at a few ≤ 10 pc, the SMBHs become gravitationally bound and form binaries or a binary AGN (Rubinur et al., 2019a), which ultimately descend into the centre of the merger remnant, release gravitational waves and unite (Johnson et al., 2016; Müller-Sánchez et al., 2018).

1.7 Starbursts and ultraluminous infrared galaxies (ULIRGs)

About 25% of the massive stars in the present-day universe are produced by starbursts (Heckman, 1997; Pasquali et al., 2003). There is a variety of galaxy types in the class of starbursts which includes: spiral galaxies, blue compact galaxies, interacting galaxies, merging galaxies and ultraluminous infrared galaxies (ULIRGs) (Pasquali et al., 2003), suggesting that starburst and nuclear activity are set off by mergers and interactions of gas-rich galaxies (Max et al., 2005). Star formation rate is exceptionally strengthened in ultraluminous infrared galaxies (Evans et al., 2001), they are thought to be made of two merging galaxy disks of almost identical mass (mass ratio $<$ 3:1, Sanders 2001, Pasquali et al. 2003). The central regions of these ULIRGs are known to exhibit spiral structure, and bright knots in their circumnuclear structure (e.g., see figure 1.1) which are identified by concentrations of younger stars whose age ranges from 10^7 to 10^8 yr (Pasquali et al., 2003).

The following section introduces the most important ULIRG for this project. This ULIRG is at a post-merging state, which is believed to play a role in the extended radio diffuse emission, detected around its large-scale environment.

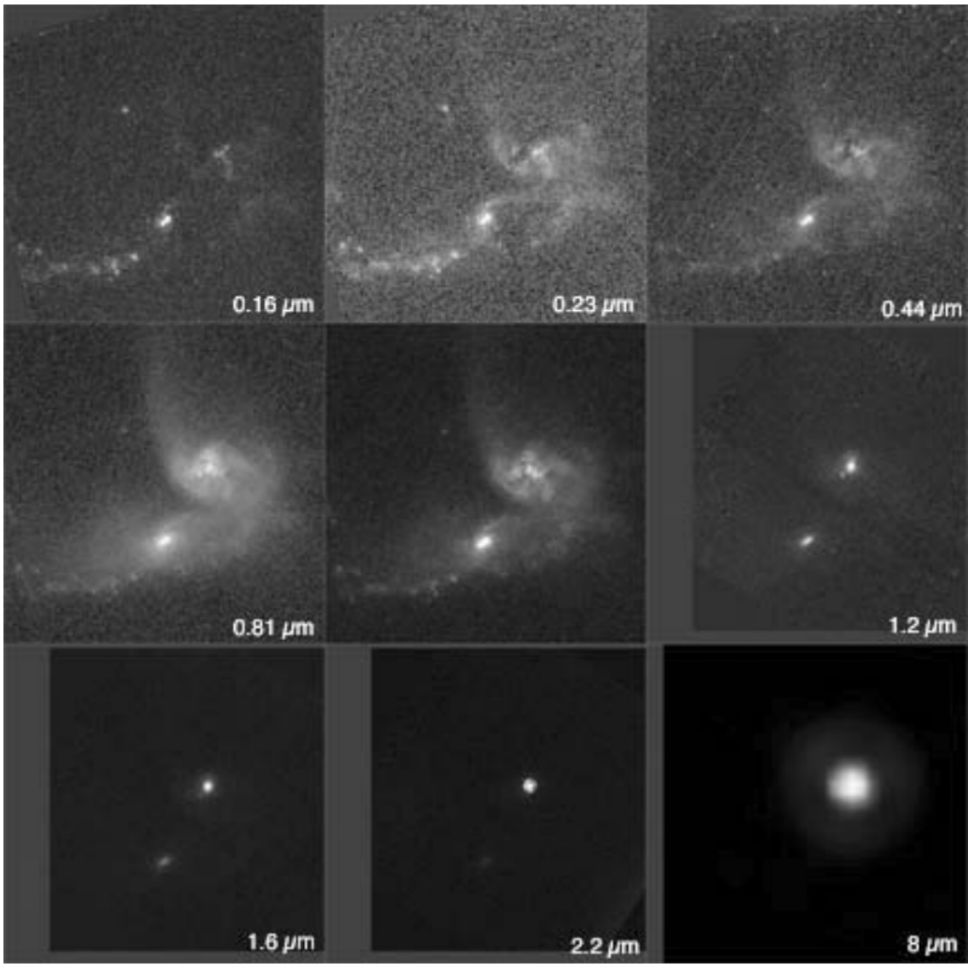

FIGURE 1.1: Ultraluminous infrared galaxy, IRAS 08572+3915, observed at multiple wavelengths (far-UV to the near-IR). The figure is taken from Lonsdale et al. (2006).

1.8 Brief introduction of NGC 6240

NGC 6240 is well known as a merging pair of galaxies (Komossa et al., 2003), at a redshift of $z = 0.0245$, a distance of ~ 100 Mpc for Hubble constant $H_0 = 73\,\mathrm{km\,s^{-1}\,Mpc^{-1}}$ where $1'' = 513$ pc. It is considered a post merger system, with AGN and star formation related ionized gas outflows (Müller-Sánchez et al., 2018). At arc-second resolution, the radio nuclear form of NGC 6240 is seen to comprise three sources (see figure 1.2); two of which indicate the locations of the parent nuclei (northern and southern nuclei), the third being an amorphous extended structure found in the north east of the southern nuclei (Gallimore and Beswick 2004; e.g., Colbert et al. 1994; Baan et al. 2007).

Subsequent Chandra observations observed and resolved both the parent nuclei of NGC 6240 as compact (Gallimore and Beswick, 2004), hard X-ray sources (e.g., Komossa et al. 2003). Together with observations of the MERLIN telescope (see figure 1.3), it was concluded that both AGNs of NGC 6240 are active (Gallimore and Beswick, 2004), and Komossa et al. (2003) classified NGC 6240 as a binary AGN. The projected separation between the parent nuclei of NGC 6240 is approximately 0.7 kpc (Müller-Sánchez et al., 2018; Fyhrie et al., 2021). In time, the binary AGN of NGC 6240 are expected to unite to form one nucleus (Komossa et al., 2003), within an elliptical galaxy.

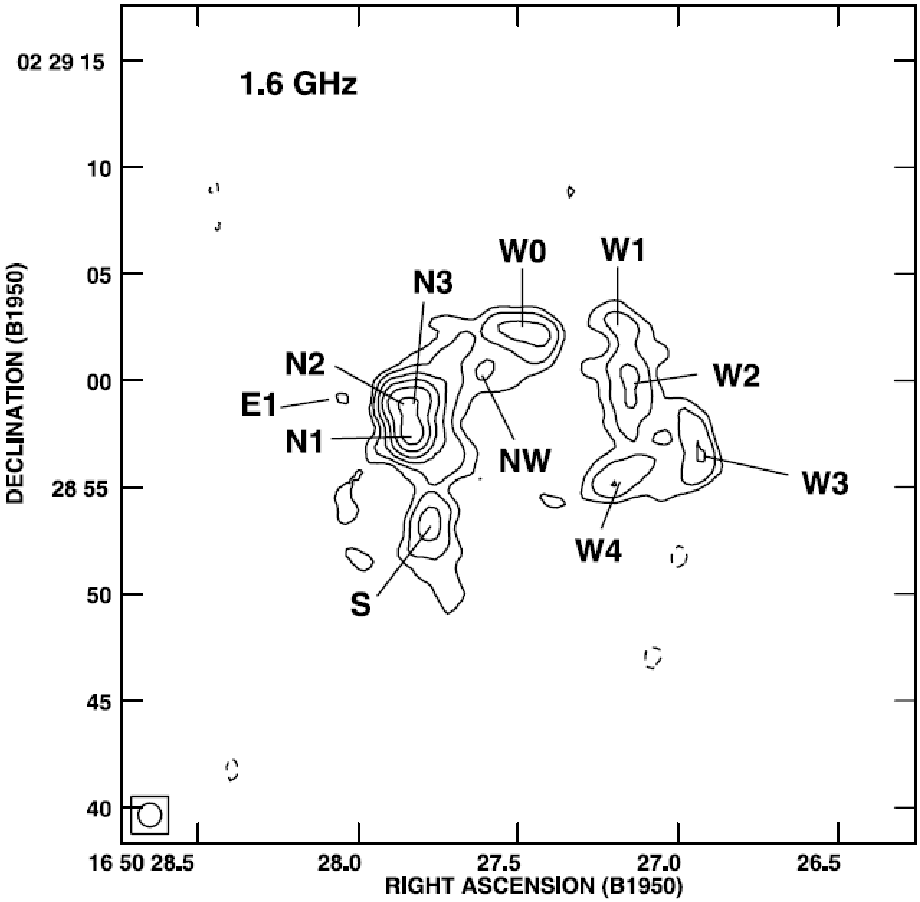

FIGURE 1.2: The higher resolution 18 cm map of NGC 6240, observed with VLA at 1.6 GHz. The contour levels are set from -1 and 1 to 64 by factors of 2 times 1.1 mJy beam^{-1}. The figure is taken from Fig. 1; Baan et al. (2007).

Using the Chandra X-ray telescope, Komossa et al. (2003) managed to extract the contribution to the hard X-ray luminosity from the parent nuclei of NGC 6240; $S_{\mathrm{L_x}} = 1.9 \times 10^{42}$ ergs s^{-1} for southern nucleus and $N_{\mathrm{L_x}} = 0.7 \times 10^{42}$ ergs s^{-1} for the northern nucleus, revealing that the most prominent AGN is located in the southern (Baan et al., 2007) galaxy. For the radio band at 2.4 GHz, Gallimore and Beswick

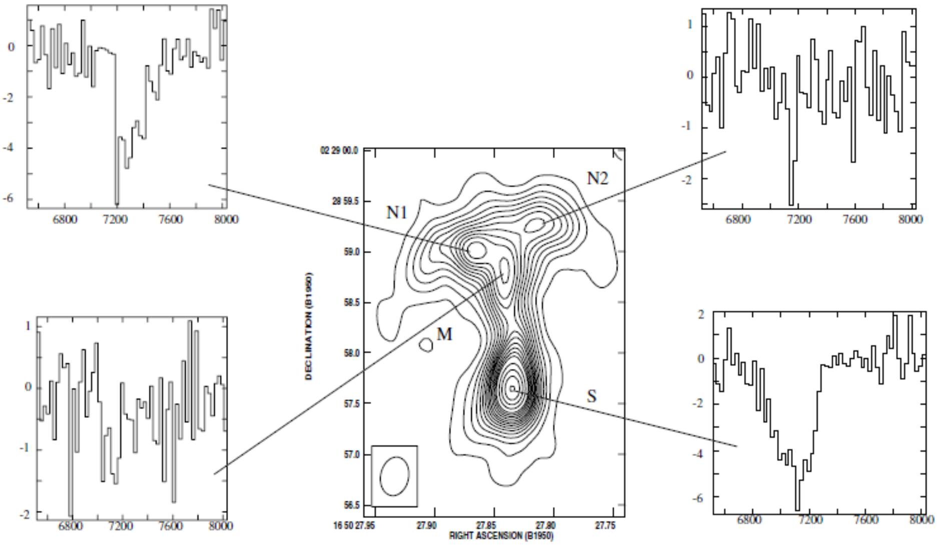

FIGURE 1.3: The MERLIN 1400 MHz naturally weighted continuum image of the centre of NGC 6240 with selected absorption spectra superposed. Figure adopted from Fig. 1; Beswick et al. (2001).

(2004) reported that the southern nucleus has a radio power of $S_{\mathrm{P}} = 3.9 \times 10^{21}$ W Hz^{-1} with a brightness temperature exceeding $S_{\mathrm{T}} = 1.8 \times 10^{7}$ K, whereas for the northern nucleus the radio power is $N_{\mathrm{P}} = 6 \times 10^{21}$ W Hz^{-1} and its brightness temperatures exceed $N_{\mathrm{T}} = 7 \times 10^{6}$ K, and both these parent nuclei have inverted radio spectrum. Within the far-infrared band, NGC 6240 is known to produce luminosity of $L_{\mathrm{IR}} \sim 6 \times 10^{11}$ L$_{\odot}$ (Baan et al., 2007), which is about half of the luminosity produced by Arp 220 (Sanders et al., 1988), and compares to the bolometric output of quasars (Gallimore and Beswick, 2004).

Komossa et al. (2003) regard NGC 6240 as a key representative of the local ultraluminous infrared galaxies (ULIRGs), and an important laboratory to understand the physics of superwinds driven by the nuclear starbursts, the processes of IGM enrichment, the physics of galaxy formation, and to explore the existence of unrevealed AGNs. Hence, NGC 6240 is observed across the electromagnetic spectrum.

Recently, Ishibashi et al. (2021) reported that both the ultra-fast outflows (UFO) and the molecular outflows seen in NGC 6240, places it in the 'forbidden' region of the N_{H}-λ plane, determined by the column density versus the Eddington ratio (Magliocchetti et al., 2018), reinforcing the notion that the radiation pressure on dusty regions of NGC 6240 may have an impact in driving its galactic outflows. The N_{H}-λ plane is normally examined observationally by plotting non-identical samples of active galactic nuclei (AGNs) with measured column density (N_{H}) and Eddington ratio (λ), derived from X-ray observations (Ishibashi et al., 2018). Other observations include the reported detection of a potential third nucleus in the ultimate stage of merging of NGC 6240 (Kollatschny, W. et al., 2020). With Chandra's angular resolution, they detected significant extended emission in both continuum and Fe lines in the $\sim 2''$ (~ 1 kpc) region surrounding the nuclei (Fabbiano et al., 2020; Paggi et al., 2022), but they were unable to gather sufficient X-ray emission data to support the identification of the third nucleus indicated by Kollatschny, W. et al. (2020).

1.9 Synchrotron emission

Synchrotron emission is caused by gyrating ultra-relativistic electrons in magnetic field (see figure 1.4), for that reason, it is the simplest and straight forward method to find magnetic fields within astronomical objects (Govoni and Feretti, 2004). The lower the strength of magnetic field, the higher the energy of an electron needed to generate emission at a specific frequency (and vice versa) (Feretti et al., 2012). The power released by these relativistic electrons depends on their magnetic field strengths and their energy (Feretti et al., 2012). The total energy content in a synchrotron radio source depends on the contributions from relativistic particles (electrons plus protons) and from magnetic fields, taking into consideration the portion of the source volume covered by magnetic fields (Feretti et al., 2012).

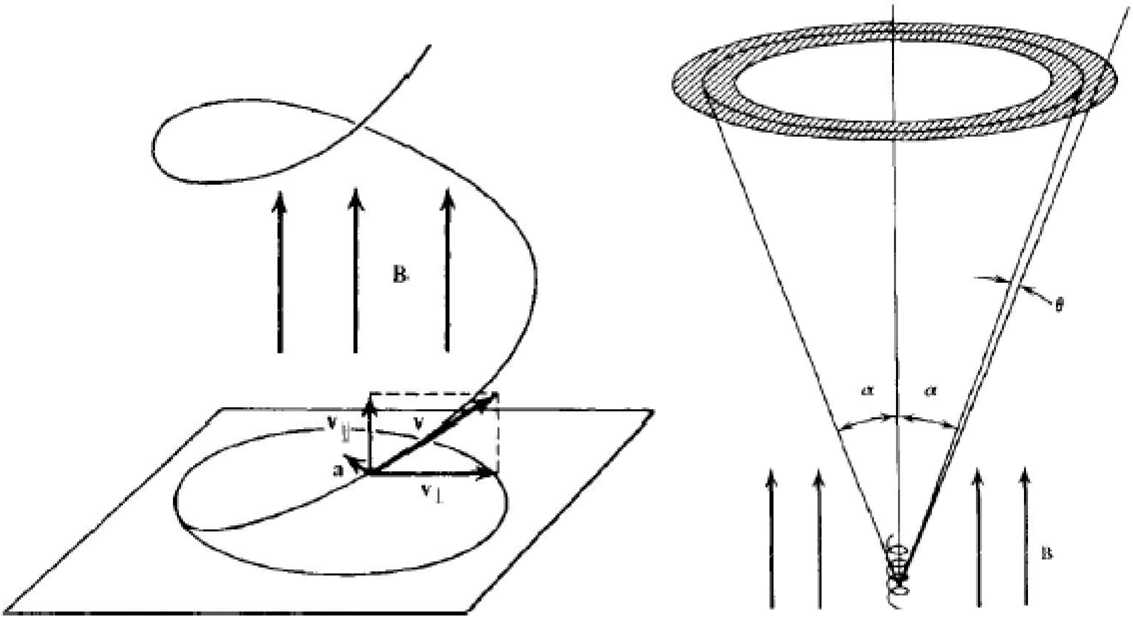

Figure 1.4: Left: A charged particle undergoing helical motion in an homogeneous magnetic field. Right: Synchrotron emission from a particle at pitch angle α restricted to the gray region. Both figures taken from Donnert (2011).

Consider an electron with energy, given by $\epsilon = \gamma \ \mathrm{m}_e \mathrm{c}^2$ where γ represents the Lorentz factor, spiraling in magnetic field **B** under the influence of $\mathbf{v} \times \mathbf{B}$ force that forces its motion to be helical along the field lines, therefore the acceleration of this electron generates emission which is radiated out from the electron over the beam, hereafter (Govoni and Feretti, 2004).

This radiation can be seen as a continuum with a spectrum that peaks in proximity of the critical frequency:

$$v_c = c_1 B \sin\theta \epsilon^2. \tag{1.1}$$

A relativistic electron emits a synchrotron power given by

$$-\frac{d\epsilon}{dt} = c_2 B \sin\theta^2 \epsilon^2, \tag{1.2}$$

where the angle between the velocity of the electron and its magnetic field is given by θ while c_1 and c_2 are typical physical constants

$$c_1 = \frac{3e}{4\pi m_e^3 c^5}; c_2 = \frac{2e^4}{3m_e^4 c^7} \tag{1.3}$$

Equations (1.2) and (1.1) shows that the power given by relativistic electrons depends on their energy (γ) and on the strength of its magnetic field. If the magnetic field is high, the electron will require low energy to emit emission at a specific frequency.

The power-law energy distribution for electrons/particles with density between ϵ and $\epsilon + d\epsilon$ given by

$$N(\epsilon)d\epsilon = N_0\epsilon^{-\delta}d\epsilon \tag{1.4}$$

the total intensity spectrum, in optically thin regions, varies as:

$$S(\nu) \propto \nu^{-\alpha}, \tag{1.5}$$

where the spectral index $\alpha = \frac{(\delta-1)}{2}$. And in optically thick regions, the spectrum is given by:

$$S(\nu) \propto \nu^{+\frac{5}{2}} \tag{1.6}$$

1.10 Diffuse radio emission associated with massive halos

There are three known morphological categories of diffuse radio emission found in clusters, namely; radio relics, giant radio halos, and mini halos (Cantwell et al., 2016; Martinez Aviles, 2017). Radio relics are normally found in the cluster peripheral regions in the form of elongated structures that can be highly polarized (Cantwell et al., 2016), whereas giant halos and mini halos are known to permeate the cluster centres (Kuo et al., 2004). Both giant halos and radio relics have steep spectra, and typical physical sizes of 1 Mpc, whereas in radio mini halos the diffuse emission have steep radio spectrum ($\alpha <$ -1, with $S_\nu \propto \nu^\alpha$) and extends over regions of ~ 100 - 500 kpc (van Weeren et al., 2014). The diffuse radio emission in these halos is believed to result from synchrotron radiation of relativistic electrons (Kuo et al., 2004), and this diffuse emission surrounds the central radio source associated with the Brightest Cluster Galaxy (BCG) (van Weeren et al., 2014; Feretti et al., 2012; Giacintucci et al., 2014).

Recently, Mazzotta and Giacintucci (2008); ZuHone et al. (2012), suggested that the turbulence found in the cores of clusters due to sloshing motions produced by mergers is able to re-accelerate electrons, and when these electrons encounter magnetic field, they emit synchrotron emission that is capable of forming a mini halo. Feretti et al. (2000) reported that clusters that have X-ray substructures are the only ones that host radio halos. X-ray substructures in galaxy clusters indicates their ongoing merging status, and the generation of radio halos is anticipated to be associated to the processes of merging galaxy clusters (Kuo et al., 2004).

1.10.1 Role of magnetic fields

Magnetic fields play key roles in almost all astrophysical events throughout the universe. Our home planet, Earth, exhibit ~ 0.3 G of bipolar magnetic field strength at the equator and ~ 0.6 G at the North and South poles (Carilli and Taylor, 2002).

The strongest magnetic field of ~ 4 G is observed at the equator of Jupiter (this can also be seen in magnetars), and this field is influenced by its fast angular rotation (Smith et al., 1974). However, within galaxy clusters and intergalactic medium, magnetic fields play essential roles in accelerating particles and on large-scale structure formation processes, having effects on large-scale motions, collapse of clouds, turbulence, heat, etc (van Weeren et al., 2019). To this present date, the origin of these fields is uncertain. It is believed that they originate from the addition of very weak pre-existing seed fields through turbulence/dynamo or shock/compression amplification in the course of the merger events and structure formation, and various magnetic fields scales pull through due to turbulent motions (Kahniashvili et al., 2013).

Measuring these magnetic fields is not an easy task to do. However, the most promising technique to estimate magnetic field strengths is assuming that CR and magnetic fields have the same energies within radio emitting volumes ("equipartition condition"; Beck and Krause 2005, van Weeren et al. 2019). With this condition applied, the magnetic field strengths in kpc-scale extended radio lobes is $\sim$ a few μG, and $\sim$ mG in pc-scale jets (Carilli and Taylor, 2002). Ensslin et al. (1997) reported that radio relics exhibit equipartition field strengths that ranges from 0.4 - 3.0 μG, similar to the field strengths found in radio halos (eg., Bonafede, A. et al. 2009 & references therein).

1.10.2 Mini radio halos

Unlike giant radio halos which are normally located in disturbed cores, mini radio halos are found in clusters with relaxed cool regions (see figure 1.5), composed of radio emission spreading out from the cluster centres, encompassing the central radio loud Biggest Cluster Galaxy (BCG; Gitti et al. 2014, Parekh et al. 2016, van Weeren et al. 2019). Their linear sizes are typically less than 500 kpc (e.g., see figure 1.6), which are comparable to the cooling regions in the central cluster (van Weeren et al., 2019). It was in 1975, when Miley and Perola (1975) discovered a prototypical mini-halo in the constellation of Perseus cluster. About less than 30 cases of mini radio halos have been published to date, making them very rare (Richard-Laferrière et al., 2020). Feretti (2002) confirmed that radio halos (mini and giant) only occur in clusters with X-ray substructures, since X-ray substructures in clusters indicates ongoing merging (Kuo et al., 2004) between galaxy clusters. Therefore, it would be extremely difficult to classify halos without any X-ray data (Bagchi et al., 2009). Even though mini-halos are smaller than giant-halos, they still require in-situ acceleration since synchrotron emitting electrons have a short lifetime, suggesting that the central active galactic nuclei is not the source of radio emission seen in mini-halos (van Weeren et al., 2019). At 1.4 GHz, the radio power released by radio mini-halos ranges from 10^{23} to 10^{25} W Hz^{-1}, whereas for giant halos it ranges from 10^{23} to 10^{26} W Hz^{-1} (van Weeren et al., 2019). Previous authors have reported that the most brightest mini radio halos are found in the PKS0745-191 and RX J1347.5-1145 clusters (Baum and O'Dea, 1991; Gitti et al., 2007). The farthest known mini radio halo is located in the Phoenix cluster (van Weeren et al., 2019), however, Knowles et al. (2019) recently found a promising radio mini halo in a cluster called ACT-CL J0022.2-0036 at a redshift of $z = 0.8050$, which makes it the most distant mini-halo to date.

Radio mini-halos generally have higher synchrotron volume emissivities than radio giant-halos (Cassano, R. et al., 2008a; Murgia, M. et al., 2009). Due to the smaller sizes of mini-halos most of their emission is restricted to the cooling region of X-ray,

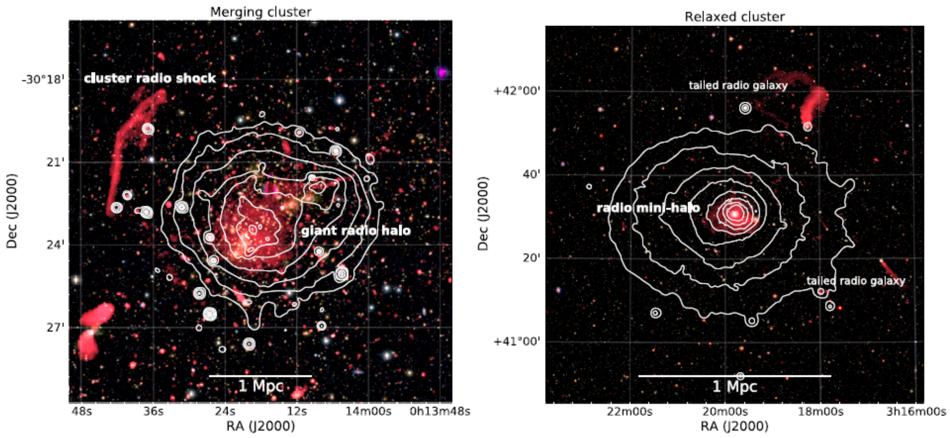

FIGURE 1.5: This figure demonstrates the difference between the relaxed and disturbed clusters, in which mini and giant halos are found. Left panel: Giant radio halo in Abell 2744 cluster was observed with VLA at 1 - 2 GHz, and it is overlaid with Chandra X-ray contours (in white). Right panel: Radio mini halo in Perseus cluster was observed with VLA at 239 - 470 MHz, it is overlaid with XMM-Newton X-ray contours (in white). Both figures adopted from Fig. 3; van Weeren et al. 2019.

suggesting that compared to giant halos, they have little e-folding radii (r_e) (Murgia, M. et al., 2009).

Due to their rare incidence and unclear origin of the radiating relativistic particles (Giacintucci et al., 2009). Historically, the birth of radio halos have been discussed between these two models: hadronic (secondary electron) and turbulent re-acceleration models (van Weeren et al., 2019).

Hadronic model involves relativistic electrons from secondary products of the hadronic interactions of CR with ICM, their radio emission is expected to be dominated at any given moment by the accumulation of CR protons in the course of the merger history of the galaxy cluster, instead of the most recent merger incident, hence radio halos in this model are expected to live longer (Cassano, R. et al., 2008b). On the other hand, since the relativistic electrons accountable for synchrotron radio emission have a shorter lifespan than the diffusion time required to reach the kpc - Mpc galactic scales of radio halos, some form of re-acceleration is invoked (Giacintucci et al., 2009). Re-acceleration model involves re-energized electrons (in situ) that are injected in the ICM by several mechanisms related to the turbulence produced by major merger incidents, hence radio halos in this model are anticipated to be have short lifespan ($\leq$ 1 Gyr) due to the limited dissipation lifetime of the turbulence (Cassano, R. et al., 2008b).

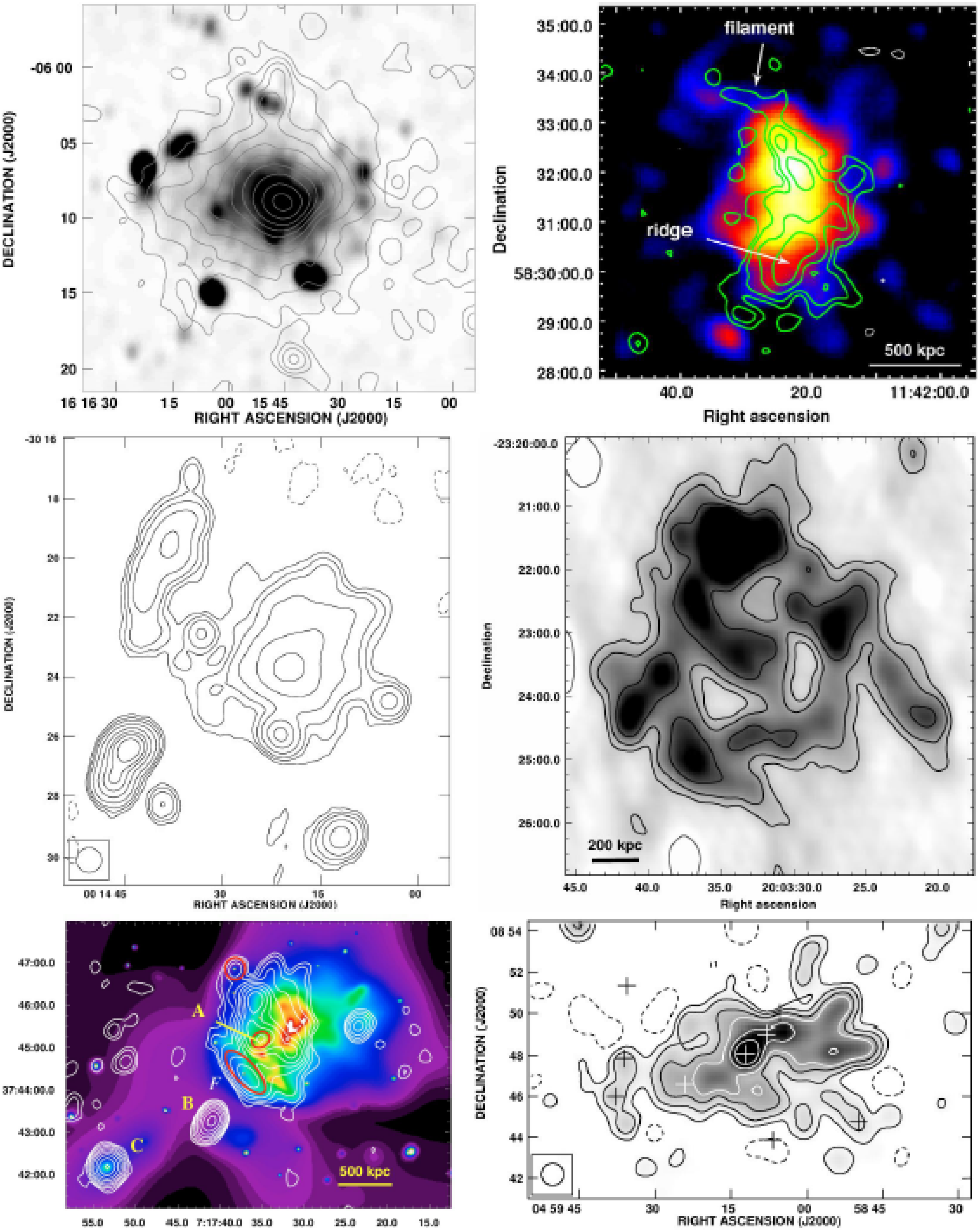

FIGURE 1.6: Examples of radio halos at 1.4 GHz (Figure 2.11; Donnert 2011). From top left to bottom right: A2163, gray represents radio emission, contour lines represents X-ray (Feretti et al., 2001); A1351, radio emission in contours, colour map is X-ray from (Giacintucci et al., 2009); A2744 from (Govoniet al., 2001); RXCJ2003.5-2323 at 610 MHz from (Venturi et al., 2007); MACSJ J0717.5+3745, contour lines are radio emission, colour map is X-ray emission (Bonafede et al., 2009); A523, radio emission from (Giovannini et al., 2011). Image Credit: Julius Donnert

1.10.3 Radio relics

Radio relics are defined as sources with extended diffuse emission, akin to low surface brightness radio halos (Feretti et al., 2012). Unlike radio halos, relics are normally located in the cluster peripheral regions and have the form of elongated structures that can be highly polarized (Cantwell et al., 2016), and they exhibit steep spectra ($\alpha \gtrsim 1$), and typical physical sizes of 1 Mpc (Feretti et al., 2012). However, these relics can be found in both cool-core and merging clusters, implying that there is a possibility that they are associated with off-axis or minor mergers, and major mergers (Feretti et al., 2012). However, not all of them are found in all merging clusters, implying that shock waves in cluster mergers are not enough to describe the mechanism behind diffuse emission of relics (Bonafede et al. 2014, Parekh et al. 2016). Prior proposed models for these relics, suggest that they are the indicators of shocks in merger events (Feretti et al., 2012).

Studies of galaxy clusters over the years have shown us that at least two types of relics are found in clusters (Kempner et al., 2004). In 1979, Jaffe and Rudnick (Jaffe and Rudnick, 1979), identified the first prototypical relic 1253+275 in the Coma cluster, and after this discovery, relics with dissimilar morphologies have been reported, namely elongated, regular, and roundish structures (Feretti et al., 2012). Kempner et al. (2004) later created a scheme on how to classify radio relics and according to their origins and observed properties, they were divided into two categories: AGN relic/radio phoenix and radio gischt.

Radio gischts (also known as radio shocks, see figure 1.7) are found in the periphery/outskirts ($\sim$ 0.5 and 1.5 Mpc away from the central cluster) of merging galaxy clusters and believed to be generated by merger driven shocks, and they are normally identified by their steepening radio spectral index behind the shock, elongated shapes, linear sizes of 0.5 - 2 Mpc, high polarization fraction of $\geq$ 20% at frequencies $\geq$ 1 GHz and power-law integrated radio spectra (Kang and Ryu, 2016). They have been seen recently in 1RXS J0603.3 and CIZA J2242.8 (van Weeren et al., 2010, 2012). In contrast, AGN relics are fossil radio plasma that is passively developing gradually from an AGN that has been shut down and radio phoenix are AGN fossil plasma compressed and revived by merger shocks (see figure 1.8; van Weeren et al. 2019). AGN relics/radio phoenix are usually located at smaller cluster centric distances (Feretti et al., 2012) and characterized by smaller linear sizes ($\leq$ 300 - 400 kpc), lower radio power, morphologies ranging from roundish shapes to elongated and filamentary (van Weeren et al., 2019). Such relics are reported by Clarke et al. (2013) and de Gasperin et al. (2015) in A1033 and A2443.

Normally, the shocks found in these relics, expand with high velocities having a Mach number $\sim$ 1 - 3, and are able to accelerate electrons to higher energies and compress magnetic fields, which causes synchrotron radiation to be emitted from large scales (Parekh et al., 2016). Out-going merger shocks are believed to be the main trajectory of these relics, whereas their relativistic electrons are thought to be diffuse shock acceleration (DSA) located near these shocks. Furthermore, both the thermal pond of electrons and mildly relativistic fossil electrons give rise to the seed electrons (Dwarakanath et al., 2018; Markevitch et al., 2005) of these sources. However, this DSA model encounters challenges in the test particle regime by several observations (Nuza et al., 2017). When dealing with relics, we focus mainly on the magnetic field scales and pre-accelerated cosmic particles pool at the cluster outskirts. Kang and

Ryu (2011) and Botteon et al. (2020) reported that the difficulty to describe detected radio luminosity of relics arises if the electrons are accelerated directly from the thermal pond, which requires high acceleration efficiency (First-order Fermi process).

The main origins of these pre-accelerated particles are believed to be AGN of radio galaxies and supernovae, the statement suggest that electrons are expelled from activities of radio galaxies (and/or supernovae), dispersed into ICM, after which the processes of cluster merger re-energises the pre-existing electrons to advance over ∼ kpc/Mpc distances (Parekh et al., 2020). These relics (and radio halos) can be detected at redshift range ∼ 0.2 - 0.4, but this is not a limit as they can also be detected at higher redshifts (Feretti et al., 2012).

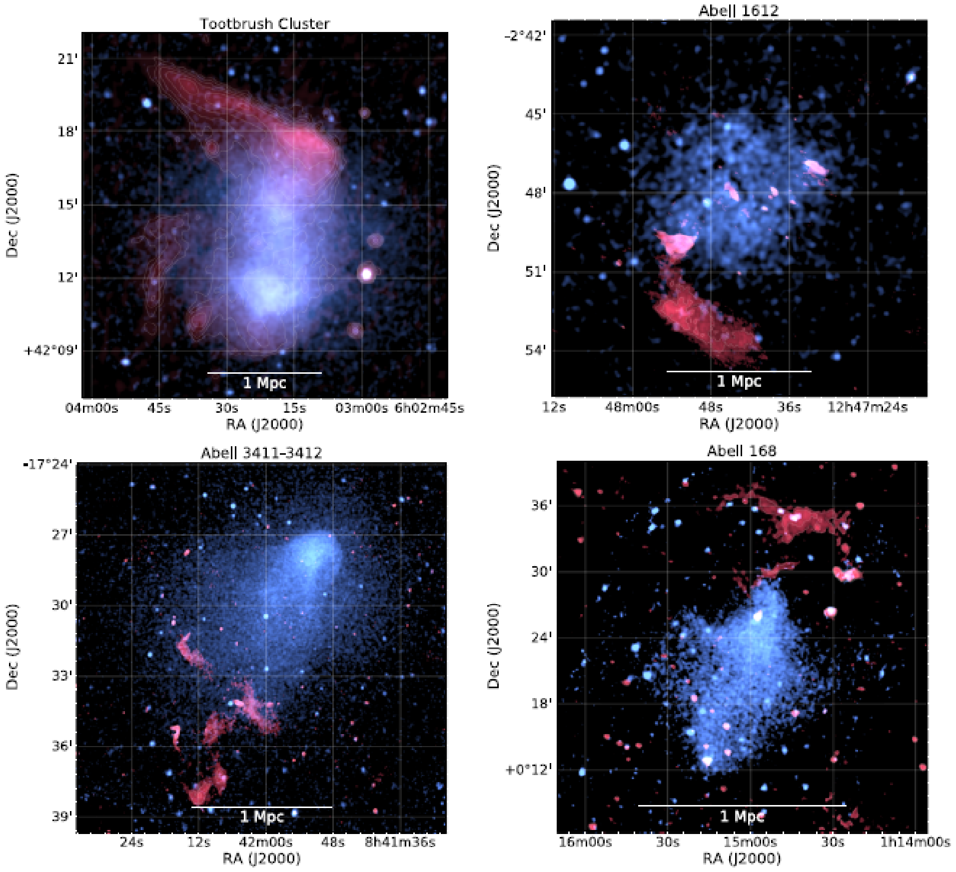

FIGURE 1.7: This figure illustrates some of the known radio gischts. The blue color represents X-ray emission, whereas the red color represents radio emission. Abell 1612 and Abell 3411 - 3412 are observed with GMRT at 610 MHz and Chandra at 0.5 - 2.0 keV. Toothbrush cluster is observed with LOFAR at 120 - 180 MHz and Chandra at 0.5 - 2.0 keV. Abell 168 is observed with GMRT at 323 MHz and also with XMM - Newton at 0.4 - 2.3 keV. This figure is adopted from Fig. 13: van Weeren et al. 2019.

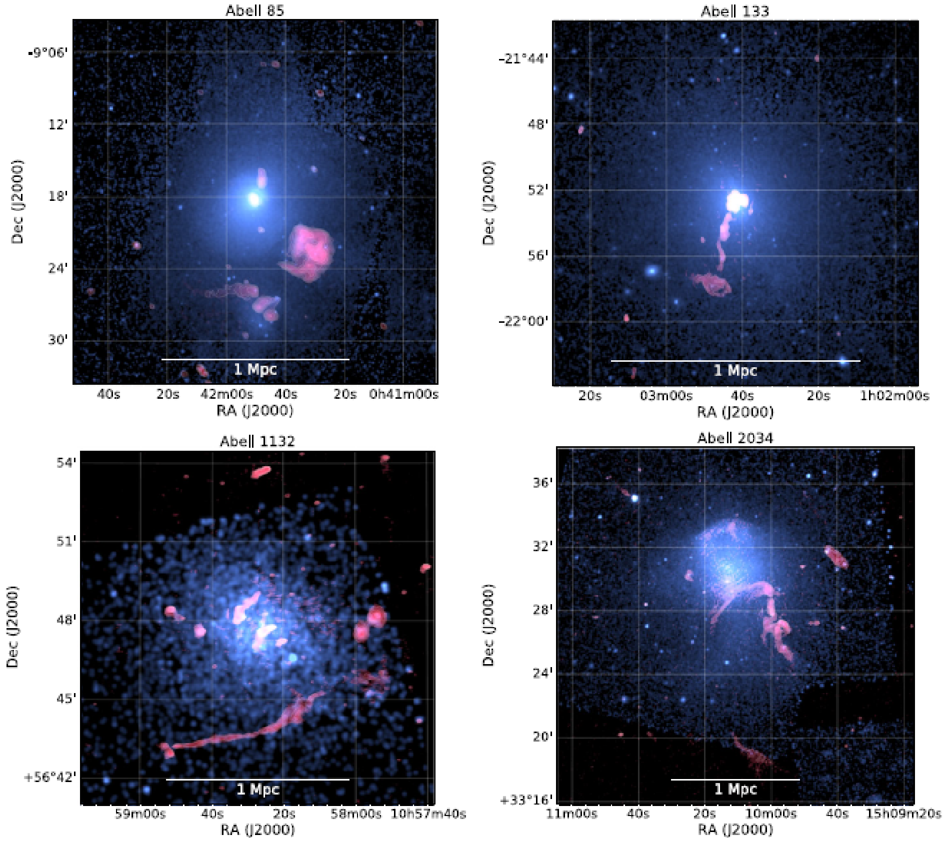

Abell 85

Abell 133

Abell 1132

Abell 2034

FIGURE 1.8: This figure exhibits some of the known radio phoenix and AGN relics. The blue color represents X-ray emission, whereas the red color represents radio emission. Abell 133 is observed with GMRT at 325 MHz; Abell 85 with GMRT at 148 MHz; Abell 1132 is observed with LOFAR at 144 MHz; and Abell 2034 is observed with LOFAR at 118 - 166 MHz. Their X-ray emission is observed with Chandra at 0.5 - 2.0 keV. This figure is adopted from Fig. 28; van Weeren et al. 2019.

1.11 Objectives and aims

The aim is to understand the nature of the diffuse emission discovered with MeerKAT. The primary objective of this project is to map the MeerKAT-discovered radio shock in proximity of NGC 6240 at multiple scales and constrain its origin and energetics. The combined analysis of the HI, cold molecular gas, ionized gas, and this radio shock will lead to a more holistic understanding of this complex, yet prototypical source.

1.12 Thesis structure

This thesis is arranged as follows:

- Chapter 2: This chapter introduces radio interferometry, calibration methods, and imaging techniques. It also highlights the exceptional capabilities of the MeerKAT instrument, particularly for the studies of this project.
- Chapter 3: This chapter presents the results obtained with MeerKAT, as well as those from the ancillary data: Hubble Space Telescope (HST), Wide-field Infrared Survey Explorer (WISE), and Chandra X-ray Observatory. These results include the discovery of the extended diffuse emission around the post-merger system of NGC 6240, the radio diffuse source, and the four radio galaxies (bright discrete sources) blended in the extended diffuse emission. Furthermore, we explore the complex jet morphology of NGC 6240 at high resolution.
- Chapter 4: This chapter provides a detailed analysis of the newly discovered extended diffuse emission and radio diffuse source in proximity of the post-merger system of NGC 6240. Using various relevant physics calculations and measurements, we classify the newly discovered diffuse sources and interpret their nature, using prior proposed models in literature.
- Chapter 5: This chapter summarises and conclude the results of this project, and highlights future works.

Chapter 2

Radio Interferometry, Calibration and Imaging

This chapter delineate the radio synthesis fundamentals as practiced to producing maps of radio galaxies, as well as describing all the techniques that were applied to processing and analysing the MeerKAT data to create images for the large-scale radio extended continuum environment of NGC 6240. The methods described in this chapter, are important to radio astronomers who wishes to perform data reductions on continuum images.

2.1 Radio interferometry

Radio Interferometry refers to an array of radio antennas, used to observe astronomical objects simultaneously to create a discretely sampled one telescope with a large aperture. Radio Interferometry uses many compact antennas to improve the data in radio astronomy research and permits a use of inexpensive radio telescopes.

In 1946, Ryle and Vonberg (1946) used the first radio interferometer to study cosmic radio emission that were first detected by Jansky, Reber and others a few years earlier. At only 175 MHz, they were able to operate an array of two dipole antennas, with the longest distance between the antennas being 240 m and the shortest distance being 17 m (Ryle and Vonberg, 1946). They used a transit-interferometer to determine the Right Ascension, which required antennas to point towards the local meridian at a definite altitude, and wait for the Earth's rotation to move the observed object along the Right Ascension (Smirnov 2011 & references therein). Figure 2.1 demonstrates a 2-element interferometer, where the zenithal angle for the observed object is θ and is not equal to zero, B is the antenna that receives the electromagnetic waves first and antenna A thereafter with a delay $\tau = (D/c)\sin\theta$ where c is the speed of light. The detector of the receiver, integrated over time, will produce a feedback proportional to the square sum of the voltages of the two signals comparable to the trace in figure 2.2 (Pluchino and Bradaschia, 2020).

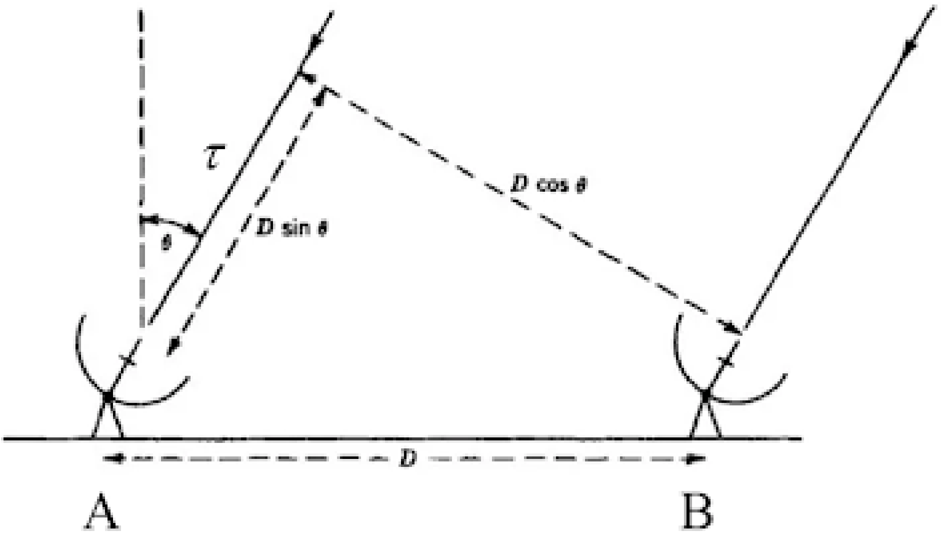

Figure 2.1: Ryle and Vonberg interferometer showing how signals reach two dipole antennas separated by baseline D (Pluchino and Bradaschia, 2020).

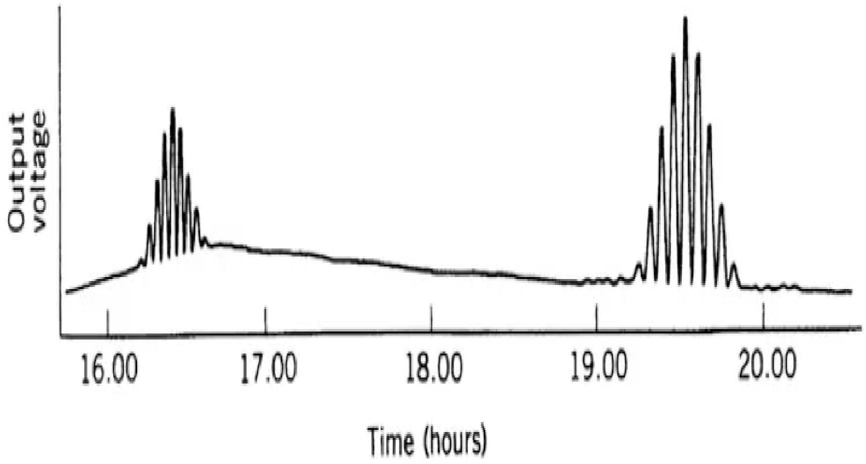

Figure 2.2: Shows the feedback produced by the transit interferometer detector, during the passage of two powerful radio sources at the meridian, at about 16:30 and 19:30 respectively (Pluchino and Bradaschia, 2020).

2.2 MeerKAT

The MeerKAT telescope is an array composed of 64 antennas that are joined together using the modern radio interferometry technique, located in the high and dry land of South Africa, Northern Cape. The objective of MeerKAT is to enable astronomers to monitor the sky in an unmatched detail and survey the entire sky many times faster than any system currently in existence. Due to these science objectives, the antennas are placed in a unique manner; 48 of these antennas are located in the central area called the core with $\sim$ 1 km diameter, and the rest of the antennas (16) permeate to longest distances of $\sim$8 km (see figure 2.4 below). Each of these antennas is composed of the main reflector with an effective diameter of 13.5 m and a sub-reflector with a diameter of 3.8 m (Campbell, 2014). At the central frequency of 1.283 GHz, MeerKAT array can recover wide range ($5''$ to $27'$) of angular resolution (Jonas and MeerKAT Team, 2016).

FIGURE 2.3: The MeerKAT telescope rising in the high and dry lands of Northern Cape, South Africa. Image credits: SARAO

2.3 Calibration and imaging

The primary objective of calibration is to be able to amend for effects that may obstruct the scientific outcome of a measurement (an observation) due to the telescope and/or local temporary conditions so that these measurements can be compared to other measurements (at other times, other telescopes, other frequencies, etc.) and theoretical predictions (Perreault, 2021).

2.3.1 Calibrating MeerKAT data

For processing and reducing our MeerKAT data we used the OXKAT[1] pipeline (Heywood, 2020) in combination with modified scripts of procedures of our own. OXKAT is a set of PYTHON-based scripts that semi-automatically process MeerKAT data. It is most used for full-band Stokes-I continuum imaging at L-band. The data reductions

---

[1] https://github.com/IanHeywood/oxkat

performed with OXKAT pipeline depends on various astronomy packages like Common Astronomy Software Applications package (CASA[2]; McMullin et al. 2007) which does averaging, splitting, flagging, cross and self calibration; TRICOLOUR[3] which does flagging; WSCLEAN[4] (Offringa et al., 2014) which does imaging and model prediction; CUBICAL[5] (Kenyon et al., 2018) which does DI / DD self-calibration; DDFACET[6] (Tasse et al., 2018) which does imaging with direction-dependent corrections (3GC); SHADEMS[7] which plots visibilities; and RAGAVI[8] which plots gain solutions. These packages are found in the ILUFU/IDIA cluster that we use to run OXKAT scripts.

NGC 6240 was observed by MeerKAT between the 1 June 2019 and 2 June 2019. Its entire large-scale continuum environment was observed, using a total of 60 antennas at L-band (856 - 1712 MHz), supplying a maximum length of 8 km between 2016 baselines. The antenna pairs are separated by a minimum distance of 29 m, therefore, at the central frequency of 1.283 GHz, MeerKAT is able to cover angular scales ranging from $5''$ to $27'$, which enables us to get a detailed analysis of NGC 6240 at $\sim 10''$ angular resolution, however, MeerKAT's zenith observation may become insensitive for sources exceeding 0.46°.

The entire observation for NGC 6240 took 7.36 hours, including all the necessary calibrator sources. Each visibility point had a correlator configured for an 8 second integration time. The SKARAB correlator was used to perform data correlation in 4k mode with a bandwidth of 856 MHz, and a channel width of 209 kHz for each of the 4096 channels. The summary of this observation is given by Table 2.1.

TABLE 2.1: Observational and calibration details for MeerKAT data

Date	01 - 02 June 2019
Time range	18:38 to 02:14
Time on target	7.36 hr
Channel width	209 kHz
Number of channels	4096
Integration time	8 seconds
Number of antennas	60
Bandpass/flux calibrator	PKS1934-63
Gain calibrator	J1550+0527
Image rms	$10\,\mu$Jy beam^{-1}
Image size	10240 × 10240
Restoring beam	$6''.9 \times 6''.9$
Pixel scale	1.1 arcsec
Pointing centre (J2000)	RA 16:52:59 Dec +02.24.04

Below is a brief description of the steps used by OXKAT pipeline:

---

[2] https://github.com/casangi
[3] https://github.com/ska-sa/tricolour
[4] https://gitlab.com/aroffringa/wsclean
[5] https://github.com/ratt-ru/CubiCal
[6] https://github.com/saopicc/DDFacet
[7] https://github.com/ratt-ru/shadeMS/
[8] https://github.com/ratt-ru/ragavi/

Cross-calibration (1GC)

The steps in this process are all carried in CASA as follows; Firstly, the OXKAT pipeline used CASA to average our MeerKAT data from 4096 (4K) channels to 1024 (1k) channels. The second step examined our measurement set (MS) contents (field list), and the target, primary and secondary calibrators were determined. The third step, applied basic flagging to the known calibrators and bad antennas, and any frequency bands corrupted by RFI were flagged out. From here calibrators were automatically flagged, prior to the model creations of the secondary calibrator fields. Then both primary and secondary calibrator solutions were applied to the target fields, from there, the corrected target data are split out into measurement sets. Prior imaging with WSCLEAN, TRICOLOUR was used to take these corrected target data through automatic flagging. To do imaging, WSCLEAN used multi-frequency synthesis (MFS) to generate the map (full bandwidth map), and a Briggs weighting of robust -0.3. A synthesized beam of $6''.9 \times 6''.9$ was attained from the last step, and from this a regular clean was applied, where we used the rectangular shape in a source free region to obtain the lowest rms value of 10 μJy beam^{-1} which was then used to calculate the 3σ threshold, giving the detection level of 30 μJy beam^{-1} in our maps.

Figures (2.4) and (2.5) shows that the length of the longest distance (baseline) is about 35500 wavelengths, which gives a rough estimate of the resolution and pixel (cell) size: From the length of the maximum baseline, we can estimate the resolution of MeerKAT,

$$R \sim \frac{\lambda}{D}, \tag{2.1}$$

where R is the resolution in radian, λ is the wavelength and D is the maximum baseline in wavelengths. Since our baseline is in wavelengths, equation (2.1) becomes:

$$R \sim \frac{1.0}{D}, \tag{2.2}$$

respectively. Therefore, substituting our longest baseline, we get:

$$R \sim \frac{1.0}{35500} \sim 2.82 \times 10^{-5} \text{ rad} \tag{2.3}$$

To get the resolution in arcsec units, we multiply the factor below:

$$R \sim 2.82 \times 10^{-5} (60 \times 60 \times \frac{180}{\pi}) \sim 5'' \tag{2.4}$$

Finally, for pixel size we divide the resolution by a factor of 4.5:

$$\text{Pixel-size} \sim \frac{R}{4.5} \sim \frac{5}{4.5} \sim 1.1'' \tag{2.5}$$

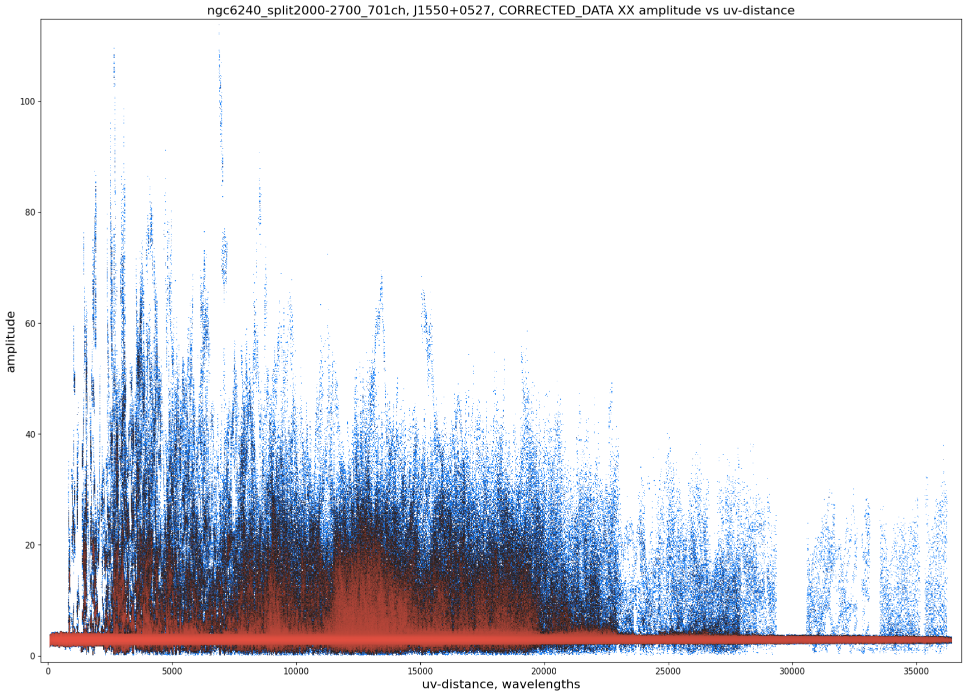

Figure 2.4: Amplitude vs. uv-distance for NGC 6240. The large scale emission of our source peaks at short baselines (indicated by high amplitude points), implying that amplitude is higher at shorter baselines.

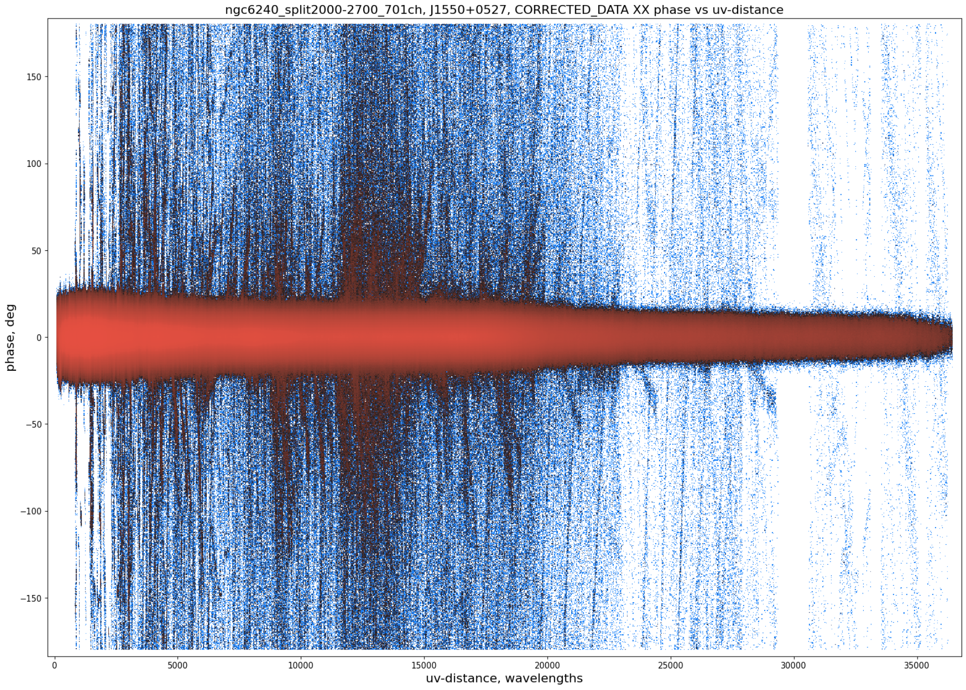

Figure 2.5: Phase vs. uv-distance for NGC 6240, with a phase calibrator centred at zero. The phase of our source is wider at short baselines and narrower at longer wavelengths.

Subtraction of Hercules A

At a redshift of $z = 0.154$, Hercules A is well known as the strongest and brightest radio galaxy (Dreher and Feigelson, 1984), with an angular extent of 2 - 3 arcmin (Maltby et al., 1962). In our MeerKAT image shown in figure 2.8, the angular extent of Hercules A is $\sim$ 4 arcmin and its morphology resembles that seen in VLA image (see figure 2.6), showing uncommon jet-dominated morphology with no compact hotspots but two different jets (Gizani and Leahy, 2003). The VLA observations have shown that the unresolved core of Hercules A, exhibit the flux density of 41 mJy at 18 cm (Gizani and Leahy, 2003). With MeerKAT, the unresolved core of Hercules A is $\sim$ 135 μJy at 1.28 GHz. At low frequencies ($\lesssim$ 1.4 GHz), Hercules A remains the fourth brightest double radio-source associated with galactic nucleus (DRAGN) in the sky, giving a total radio luminosity of $\sim 3.8 \times 10^{37}$ W in the 10 MHz - 100 GHz band (Gizani and Leahy, 2003).

With such a powerful luminosity, the emission of Hercules A overlaps/dominates that of nearby sources, in our case the target source NGC 6240. The overlap causes analytical challenges for our target source NGC 6240, these challenges include obscuring and limiting attainable dynamic range when performing calibration and imaging techniques. Since we are able to model the extended diffuse emission of the obscured NGC 6240 (in the presence of Hercules A), we then subtracted Hercules A from the data-set and thus disengaging its brightest emission. Although we focus on this, we end up subtracting several bright sources outside of the 10k image. The subtraction procedure for the latter is illustrated by the flowchart in figure 2.7.

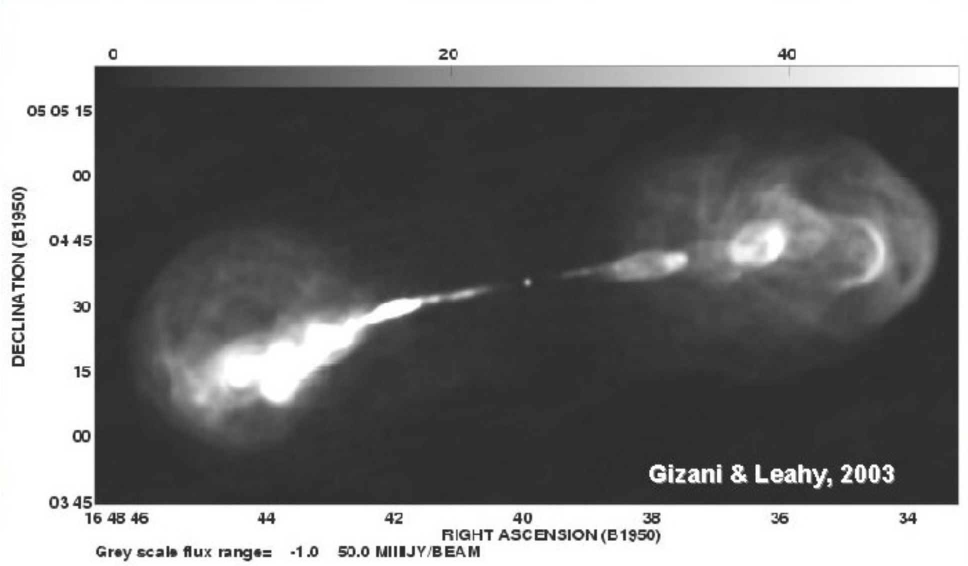

FIGURE 2.6: The VLA A+B+C image of Hercules A at 18 cm at 1.4 arcsec resolution (Gizani and Leahy, 2003).

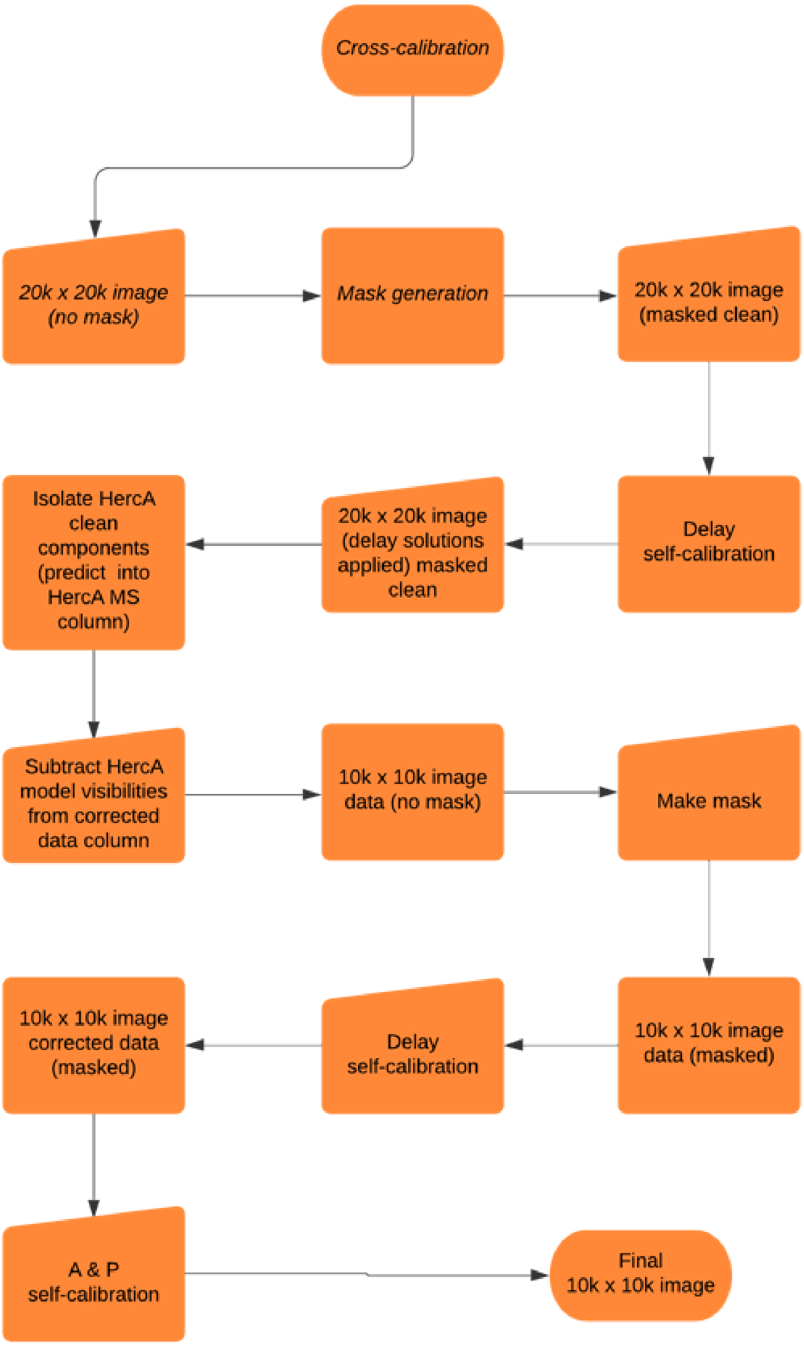

FIGURE 2.7: Flowchart illustrating the calibration and imaging processes for Hercules A.

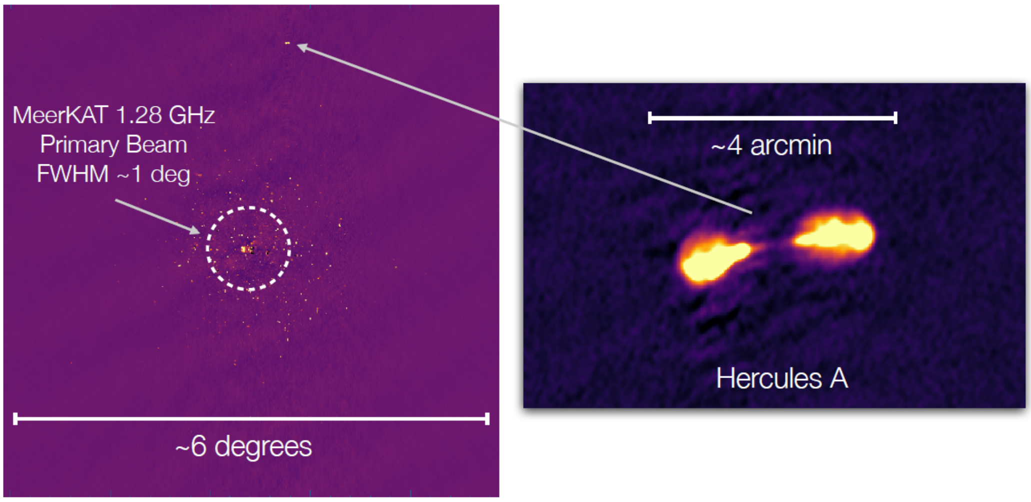

FIGURE 2.8: Diagram illustrating the 20k × 20k image, emphasizing the vast large-scale environment of NGC 6240 which include HerculesA located approximately 2 degrees from NGC 6240. There is the presence of a low-frequency sinusoidal component running in a north-east to south-west direction, which is as yet not fully understood, but does not impact our core results.

Self-calibration (2GC)

The steps in this process uses CASA and WSCLEAN as follows; Firstly, the corrected data was re-imaged using the mask from the last imaging step of 1GC. During the re-imaging process the mask gets updated, and from this the sky model of the target was predicted. Then CASA used the sky model to do self calibration on the target data, which in turn provided calibration solutions (single-direction). Using these calibration solutions, 2GC data was corrected and re-imaged, giving refined models for both the mask and the sky.

We also used KILLMS[9] to analyse our data; however 3GC (Tasse et al., 2018) techniques did not improve the image drastically while at the same suppressed the large-diffuse emission of interest. Because this negatively impacted our science goals, we chose to stay with 2GC calibration. The RFI environment of the observations is not extremely different from the known RFI for MeerKAT observations, but there may still be non-obvious low-level RFI present. It is also possible that pointing errors may be responsible for the image artefacts, but for now the solution is beyond the scope of this thesis.

2.3.2 Imaging MeerKAT data

Source subtraction

Even at the presence of various individual number of bright sources, the diffuse emission in our radio extended halo continuum is clearly apparent. However, since our objective is to retain the image fidelity of the entire diffuse emission in proximity of NGC 6240 and measure its flux, we had to subtract these bright sources in our uv plane. To accomplish this, we used CRYSTALBALL[10] together with DS9 and CASA to do the subtraction of the unwanted sources. CRYSTALBALL makes use of the deconvolved model generated by WSCLEAN, from this generated model we selected the unwanted bright sources using region selection in DS9. The selected regions (in the form of circles) used for the subtraction had an uncertainty ranging from ∼ 0.29 - 0.68 %.

We agree that robust estimation of all the uncertainties need to be captured, the quantification and inclusion of this subtraction error is sub-dominant and is deemed to be beyond the scope of the thesis. The regions were then used in CRYTALBALL to limit the re-prediction of visibilities from our original deconvolved model and to store the predicted visibilities in model data column, then we used the uv-sub task in CASA to subtract the model from our corrected data column. This resolved out the extended diffuse emission in our map (see fig 3.12).

2.3.3 Ancillary data

The multi-wavelength data introduced here are used for purely qualitative, morphological comparisons and so we aim for brevity in their description.

Optical data

The first ancillary data we used is from the Hubble Space Telescopes (HST) archives (PI: R. van der Marel, cf. Gerssen et al. 2001). The HST NGC 6240 image was

---

[9] https://github.com/saopicc/killMS

[10] https://github.com/paoloserra/crystalball

observed with a WFPC2 camera on 28th March 1999. Due to our science objective, we only selected the F673N (narrow) filter since it can trace the low-ionization Hα gas for low redshift galaxy state wavelength. For the redshift of $z = 0.0245$, this F673N filter covers the entire Hα ionized gas emission in NGC 6240.

X-ray data

THe archival data used is from the Chandra X-ray Archival Centre (ObsID 12713; PI: G. Fabbiano, cf. Nardini et al. 2013). The X-ray image of NGC 6240 was observed with the Advanced CCD Imaging Spectrometer (ACIS-S) instrument (on-board of the Chandra X-ray Observatory). Four pointings of observations were carried out between the 29 July 2001 and 31 May 2011 with effective exposure times of 36.7, 141.2, 157.0, and 145.4 ks. The telescope was pointed in such a way that NGC 6240's X-ray photons were imaged on the black-illuminated S3 chip of ACIS. The Chandra_repo script was used to reprocess all the ACIS-S data from the four pointings using the v4.4.6 Calibration Database (CALDB), and analyzed with the following software packages; CIAO v4.4 and HEASOFT v6.12.

Infrared data

The infrared archival data is from the Wide-field Infrared Survey Explorer (WISE), obtained through NASA/IPAC Infrared Science Archive (IRSA) catalogue access tools. Wide-field Infrared Survey Explorer is a Medium Class Explorer mission of National Aeronautics and Space Administration (NASA), it has been conducting digital imaging surveys of the whole sky in the following mid-IR μm wavelengths: 3.4 μm (W1), 4.6 μm (W2), 12 μm (W3) and 22 μm (W4).

Chapter 3

Results

In this chapter, we present the multi-frequency synthesis (MFS) maps, generated from our calibration and imaging techniques described in Chapter 2. The MFS maps are used to estimate the integrated flux densities of various components, as well as to characterise the morphology of the observed radio diffuse sources both which are important for the calculations necessary to explain the nature of these sources.

3.1 MeerKAT high-resolution image of NGC 6240

Our radio continuum image reveals a connected C-structure that extends into a loop to the west (see figures 3.1 & 3.2), previously published and introduced from the Very Large Array (VLA) high-resolution A and B-array L-band images (fig. 1.2; Baan et al. 2007 and Fig. 3a; Colbert et al. 1994). Using VLA, they were able to reveal the two embedded nuclei of NGC 6240 at 1.6 GHz. The same loop structure morphology is also seen in the MERLIN 1.4 GHz map illustrated in figure 1.3 (Beswick et al., 2001). For our high-resolution MeerKAT image at 1.28 GHz, we do not spatially resolve the embedded parent nuclei of NGC 6240 since the angular separation between the two nuclei is about 2 arcsec, which is within the 6 arcsec uniformly-weighted Point Spread Function (PSF).

3.1.1 Full band, high resolution images

Figure 3.1, exhibits the full band image of NGC 6240, separated from the calibration and imaging approach described in Section 2.3.1.

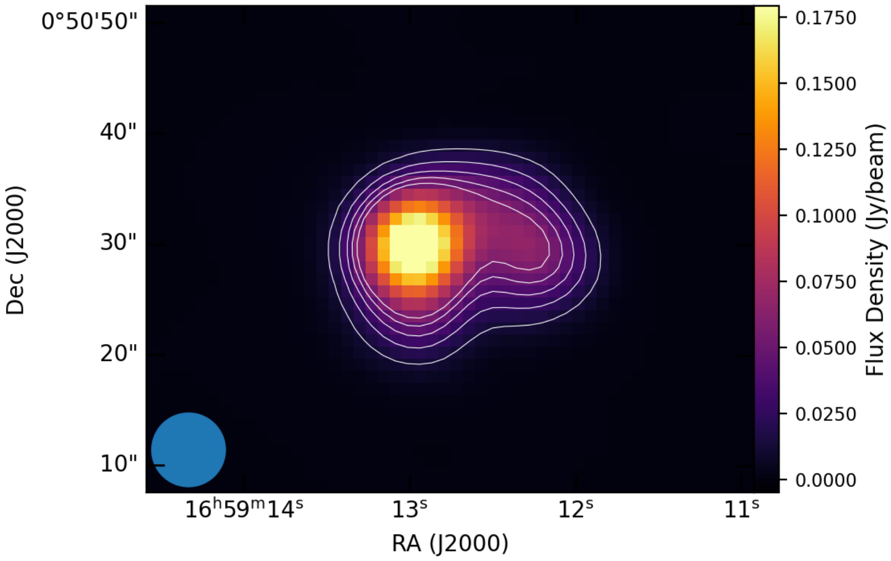

FIGURE 3.1: MeerKAT 1.28 GHz image of NGC 6240 (robust -0.3) at full band. The beam size of the image is $6''.7 \times 6''.7$ with position angle (PA) of 0.0 deg. The contour levels are set at 14.7, 26.4, 38.1, 49.8, and 61.5 mJy beam^{-1}.

3.1.2 Uniform weighting of NGC 6240 core

To obtain the continuum map shown in figure (3.2), we first highlighted the bright NGC 6240 structure in small scale form. And to best ensure the highest resolution of our source, we applied the density weighting called the uniform weighting algorithm using Casa. The pixel scale of the map is 1.1″ with local rms level of 30 μJy beam^{-1}. The loop structure to the west is believed to originate from a bubble front swept up by a superwind emanating mainly from the southern nucleus (Colbert et al., 1994; Baan et al., 2007), since the nucleus of the southern galaxy has been identified as the origin of the superwind outflow (Baan et al., 2007). This loop structure is composed of clumps of weak radio emission extending to the west (Colbert et al., 1994). This will further support the interpretation that the synchrotron emission in the western loop structure originates from superwind-driven outflows, emanating from the most prominent nucleus, the southern nucleus (Baan et al., 2007). Table 4.1 compares the radio structure properties of our high-resolution MeerKAT image with those from prior publications, these comparisons are discussed in more detail in chapter 4.

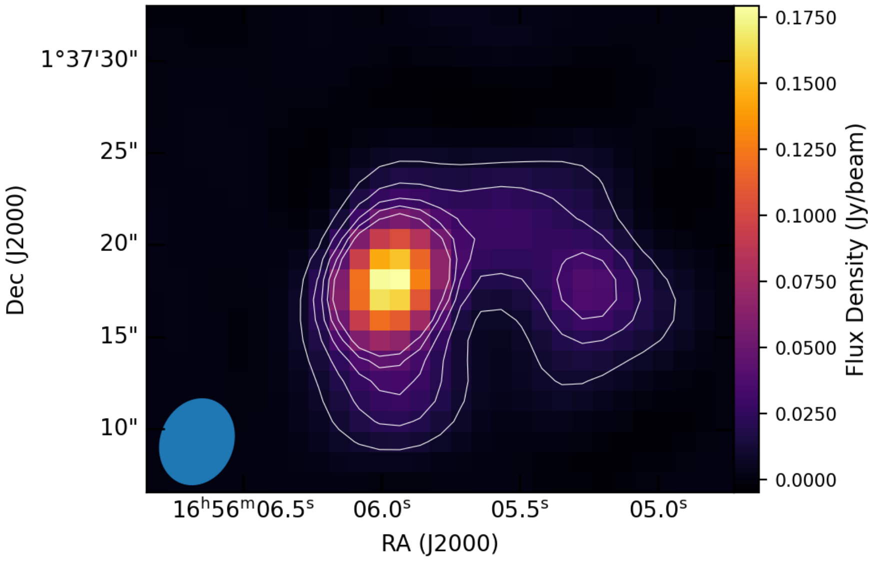

Figure 3.2: MeerKAT 1.28 GHz (uniform weighted) image of the radio loop emanating from the centre of NGC 6240, very much similar to images in figures 1.2 and 1.3. The beam size of the image is 4″.8 × 3″.9 with position angle (PA) of -22.1 deg. The contour levels are set at 11, 22, 33, 44 and 55 mJy beam^{-1}. The rms and peak values in this map are 30 μJy beam^{-1} and 179 mJy beam^{-1}.

The HST F673N image (see color map in figure 3.3) shows the ionized Hα gas filaments described by Heckman et al. (1987, 1990) and Colbert et al. (1994). This image reveals both strong and weak filaments, with weak filaments spreading out to the west and southwest while strong filaments spread out to the east and southeast respectively, in agreement with the results of Colbert et al. (1994). With improved sensitivity of our image, the filaments are well defined. The optical image was smoothed to the low resolution of 0.1 arcsec by using `Imsmooth` task in Casa, to best ensure the visibility of the faint Hα filaments, and we matched the frames (WCS) of the two images by aligning them, before pasting the contours of the radio emission over the optical image. The same procedure was applied to the X-ray image observed at 0.5 - 8 keV (see color map in figure 3.4; Nardini et al. 2013), except we did not smooth the X-ray image, which has a spatial resolution of 0.5 arcsec.

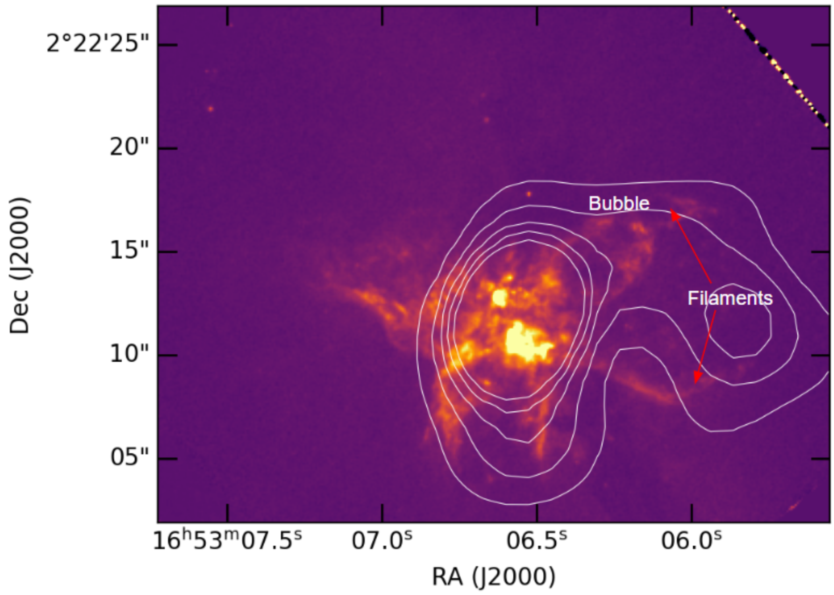

FIGURE 3.3: Overlay plot of MeerKAT 1.28 GHz radio emission contours on HST F673N optical image, observed with WFPC2 photometry mode and tuned to the narrow-band Hα emission. The colour map has a linear stretch. The contour levels for the radio emission are 11, 22, 33, 44 and 55 mJy beam^{-1}.

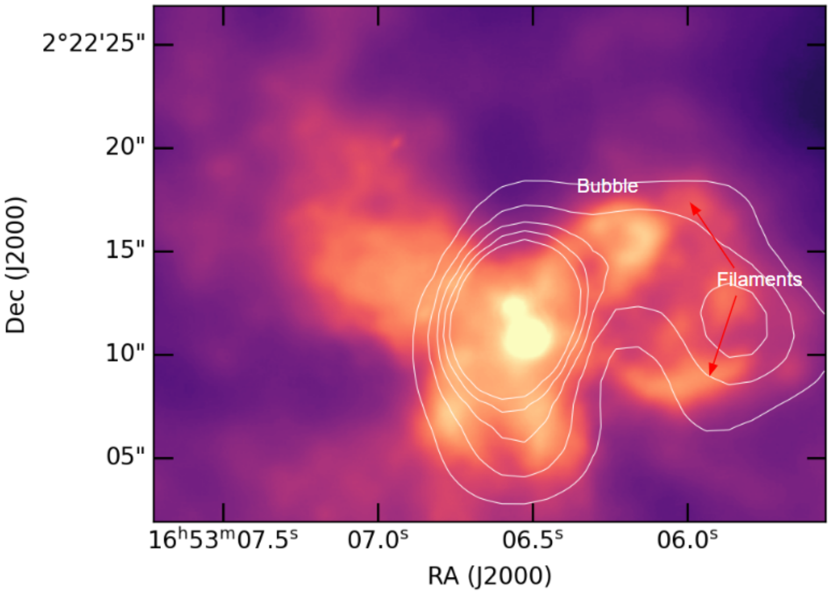

FIGURE 3.4: Overlay of MeerKAT 1.28 GHz radio emission contours on Chandra X-ray image. The X-ray image is in the 0.5 - 1.5 keV band, observed with ACIS-S, using the back-illuminated S3 chip. The colour map has a linear stretch. The contour levels for the radio emission are 11, 22, 33, 44 and 55 mJy beam^{-1}.

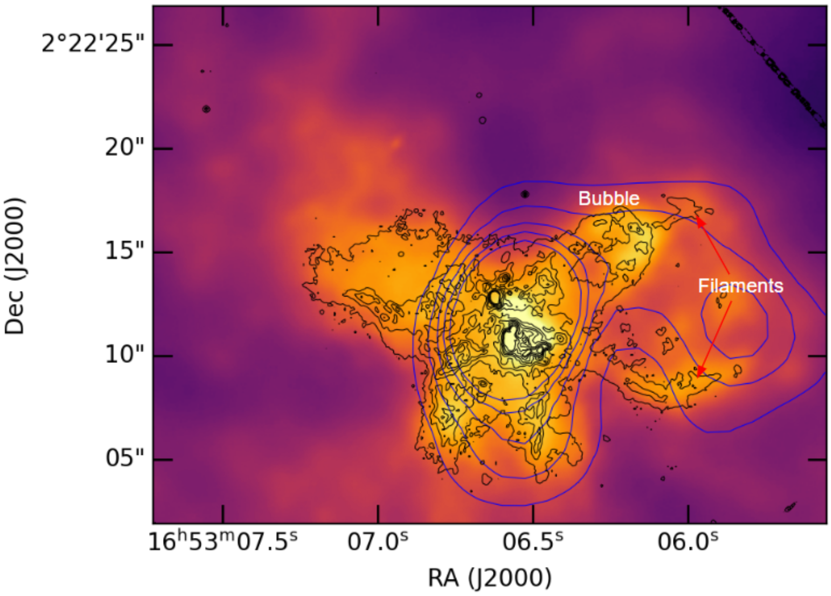

FIGURE 3.5: Chandra X-ray image (colour map) of the central region of NGC 6240 overlaid with the optical Hα bubble (black contours) and the western arm radio contours (blue). The colour map has a linear stretch. Levels for the blue contours are 11, 22, 33, 44 and 55 mJy beam^{-1}.

3.2 Extended radio continuum emission on $\sim$ 300 kpc scales

3.2.1 The extended diffuse emission

Our radio map reveals diffuse extended radio continuum surrounding NGC 6240. The map consists of various individual sources, most which are presumably background sources. The sources are illustrated in figure 3.6 (A - E), which shows the most interesting objects in proximity of NGC 6240.

Some of these sources have been detected in other bands, for example the point sources labeled A - D have been observed in optical and IR bands. Source E consists of a bright filament which seems to be linked to the identified shocks (1 and 2) through the bridges labeled 1 - 4. However, Source E and all its components have not been detected in any other bands yet although, there is a hint of it in the UVSS (see figure 3.11). The morphology of the emission illustrated in figure 3.6 is divided into two parts: Source E which lies in the eastern side of NGC 6240 and the diffuse emission extending from east to west of NGC 6240. This morphology is discussed more in chapter 4.

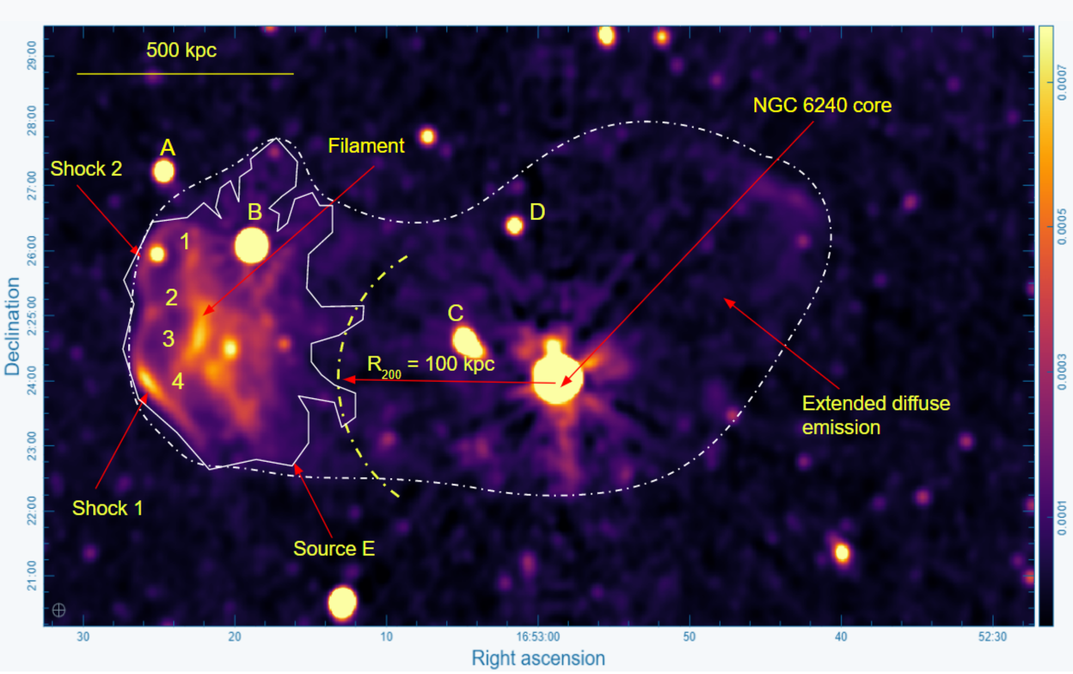

Figure 3.6: The 1.28 GHz map of the large-scale extended radio continuum around NGC 6240 smoothed to 10 arcsec at robust -0.3, with labeled components observed around NGC 6240.

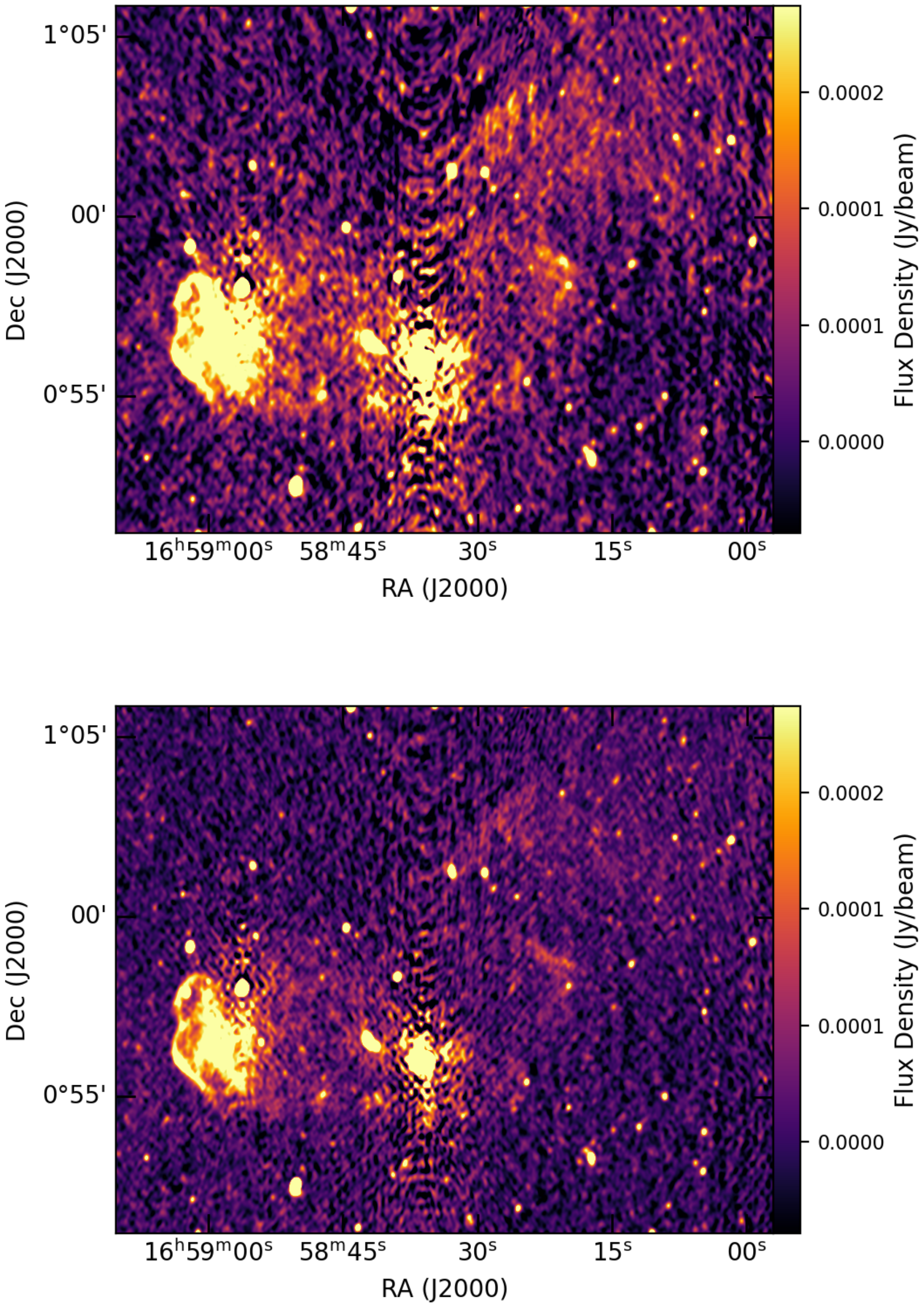

FIGURE 3.7: The large-scale extended radio continuum around NGC 6240 at 1016 MHz (top panel) and 1123 MHz (bottom panel).

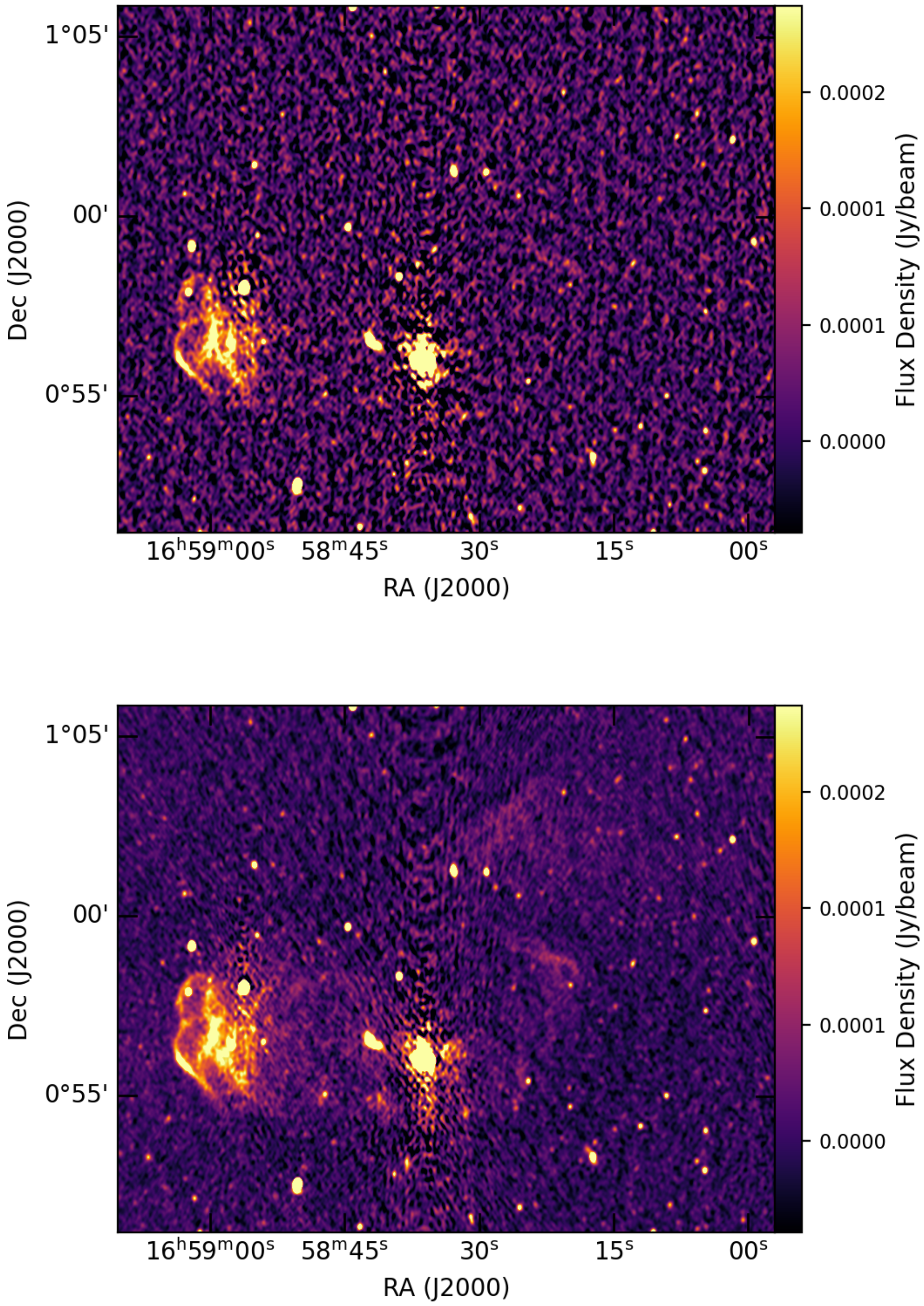

FIGURE 3.8: The large-scale extended radio continuum around NGC 6240 at 1230 MHz (top panel) and 1337 MHz (bottom panel).

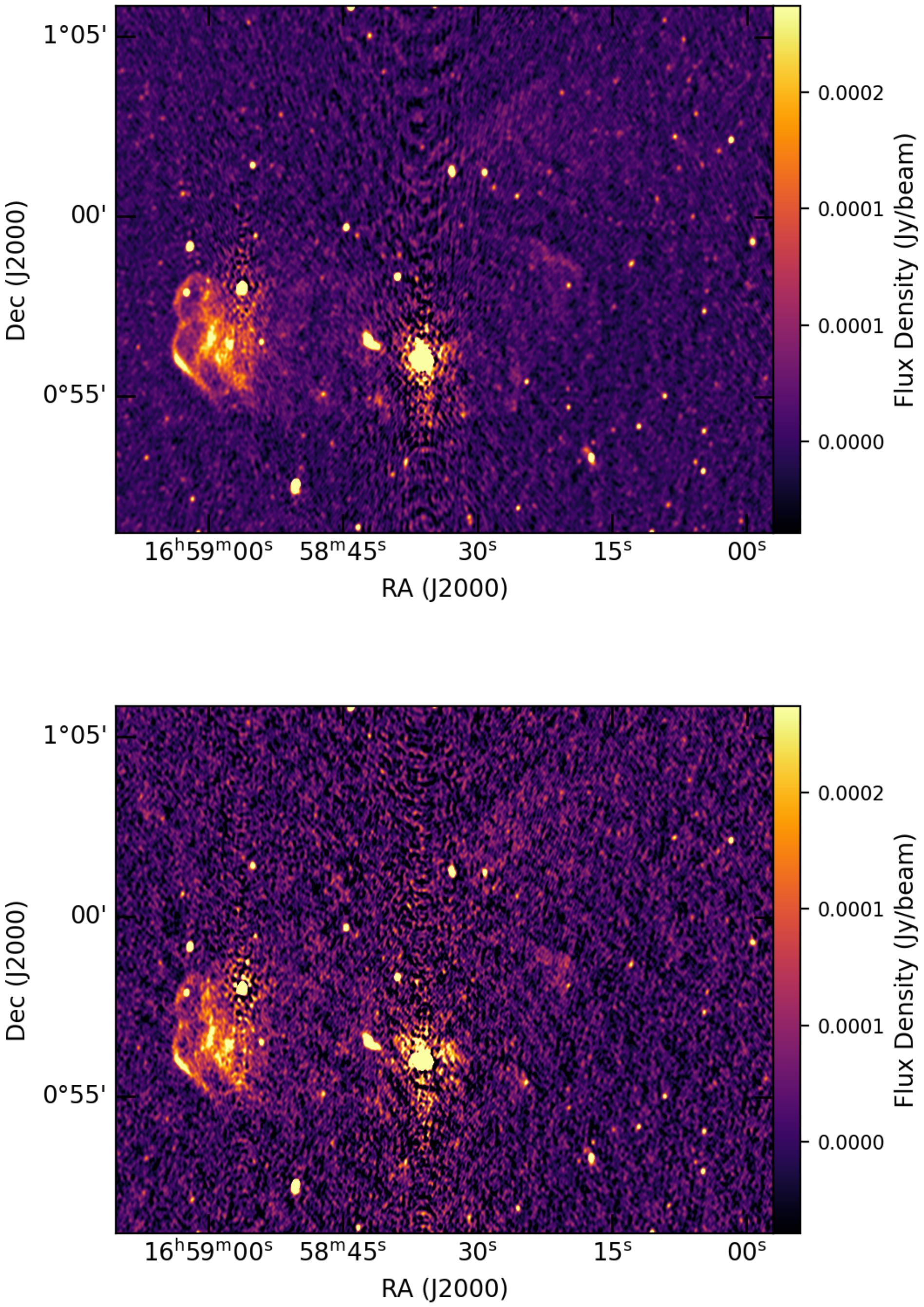

FIGURE 3.9: The large-scale extended radio continuum around NGC 6240 at 1444 MHz (top panel) and 1551 MHz (bottom panel).

3.2.2 Measurements of integrated flux density

While performing the calibration procedures, we took interest of the local rms values by drawing regions in empty locations of our image (at robust -0.3). From these regions, the lowest rms value we obtained is ~ 10 μJy beam^{-1}. We then used the lowest rms to calculate the threshold by multiplying it by 3σ, giving a threshold value of 30 μJy beam^{-1}.

Therefore, for each region of interest, the total flux density was estimated by summing all the emission within the 3σ level, using the Cube Analysis and Rendering Tool for Astronomy (CARTA) and CASA task `Imstat`, which both give a total flux density for a selected region of the map corrected for the synthesized beam.

The bright discrete and unresolved point sources (labelled A, B, C and D; fig 3.6) appears to be blended within the extended diffuse emission. However, these bright sources are superimposed in the extended diffuse emission, contaminating the fidelity of the extended diffuse emission. Therefore, these bright sources, which are unlikely to be related with the NGC 6240 extended emission were subtracted in our final map (see fig 3.12), using the source subtraction procedure explained in Section 2.3.2. The four sources could be contributing to the observed population of electrons, unfortunately, their redshifts information is currently unknown, hence we cannot be able to confirm whether they are associated with either the extended diffuse emission or the relic. The resulting flux densities of the extended diffuse emission, bright sources and the loop structure are tabulated in 3.1 and 4.1.

To estimate the flux density uncertainties, we use the following equation:

$$\Delta S = [(\sigma_{\rm amp} S)^2 + (\sigma_{\rm rms}\sqrt{n_{\rm beams}})^2]^{1/2}, \tag{3.1}$$

where S is the flux density, $\sigma_{\rm amp}$ is the flux calibration ($FC_{\rm err} \sim 10\%$, adopted from Parekh et al. 2020), the rms noise of the image is denoted by $\sigma_{\rm rms}$, and $n_{\rm beams}$ is the number of beams in the full extent of the source, which is given by the ratio of the solid angle of the source to that of the synthesized beam (Parekh et al., 2020).

TABLE 3.1: Flux density measurements at 1.28 GHz

Component	**Flux (mJy)**	**Error (mJy)**
Extended diffuse emission	13	± 2.09
Source E	49	± 4.95
A	3.1	± 0.323
B	60	± 6.00
C	4.5	± 0.467
D	1.62	± 0.178

Notes: Some residual PSF side-lobes can still be seen in figure 3.10, centred on the bright point source to the north-west, which is likely the largest source of uncertainty of our integrated flux measurement.

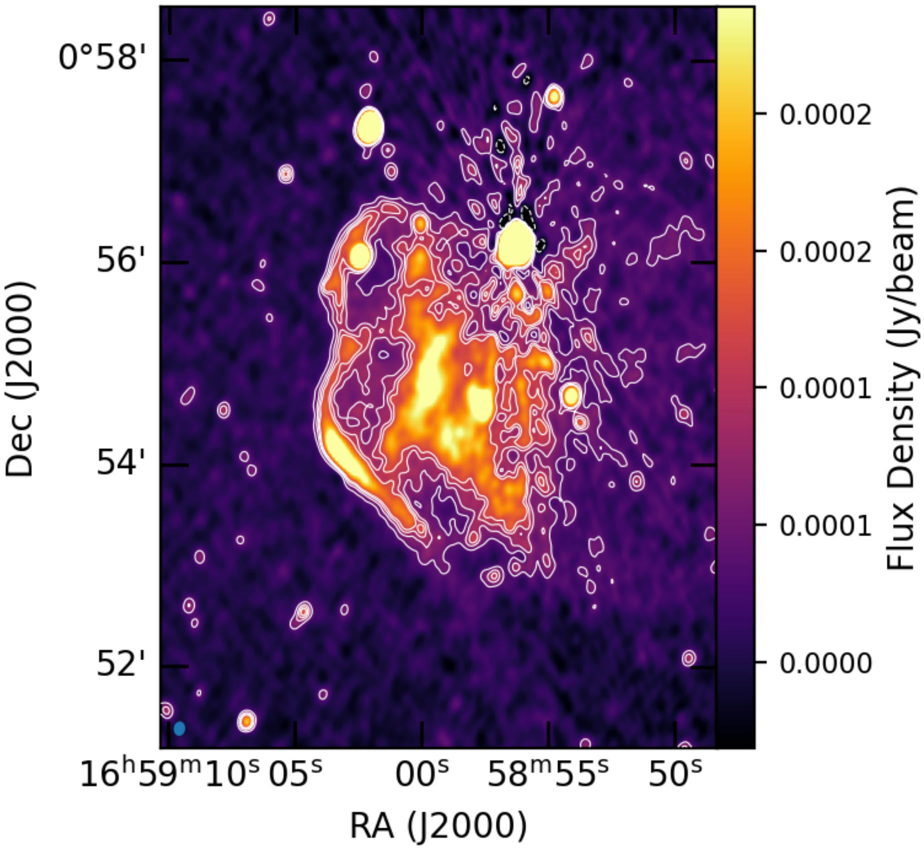

FIGURE 3.10: This figure shows the zoom-in on Source E, shown in figure 3.6. The beam size of the image is $6''.9 \times 6''.9$ with position angle (PA) of -7.45 deg. The contour levels are set at -31.4, 42.2, 72.9, 96.4, and 116 μJy beam^{-1}.

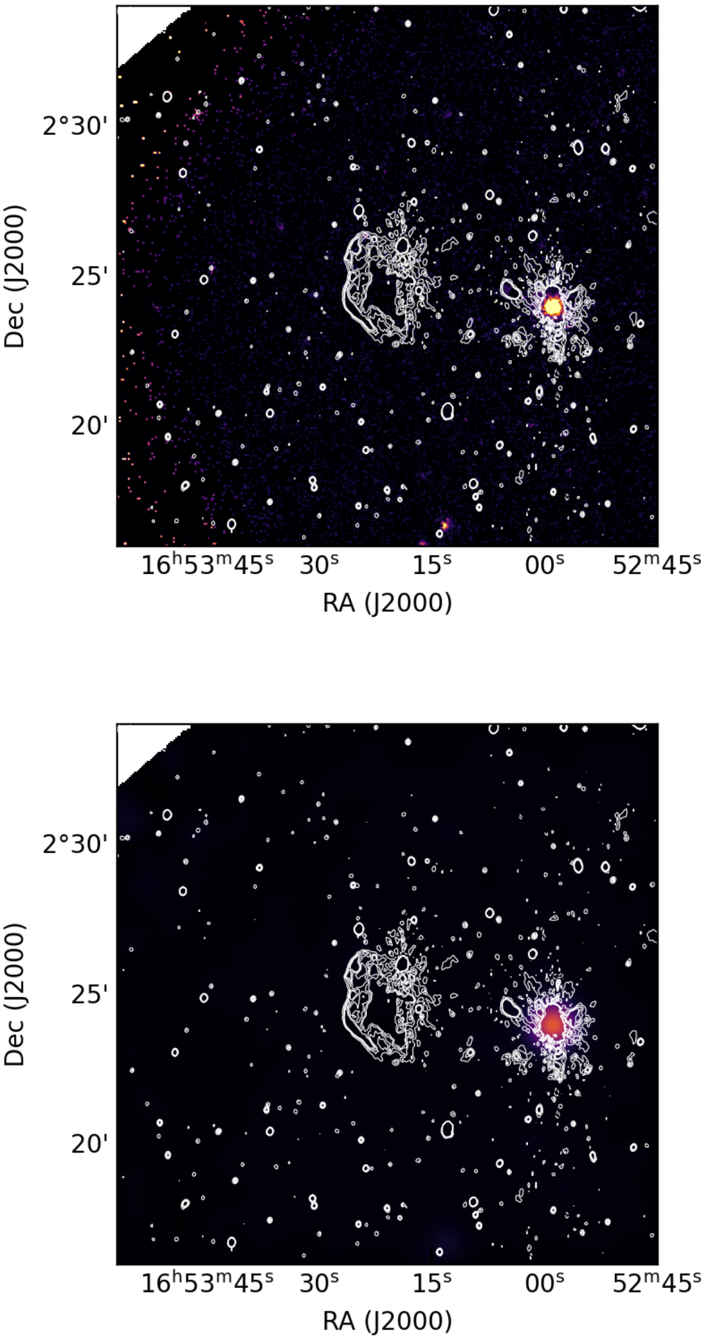

FIGURE 3.11: Overlay of MeerKAT 1.28 GHz radio emission contours on Swift X-ray image. The X-ray image is in the 0.2 - 10 keV band. The colour map in the top panel has a linear stretch and the colour map in the bottom panel is smoothed to 1 arcmin. The contour levels for the radio emission are -31.4, 42.2, 72.9, 96.4, and 116 μJy beam^{-1}.

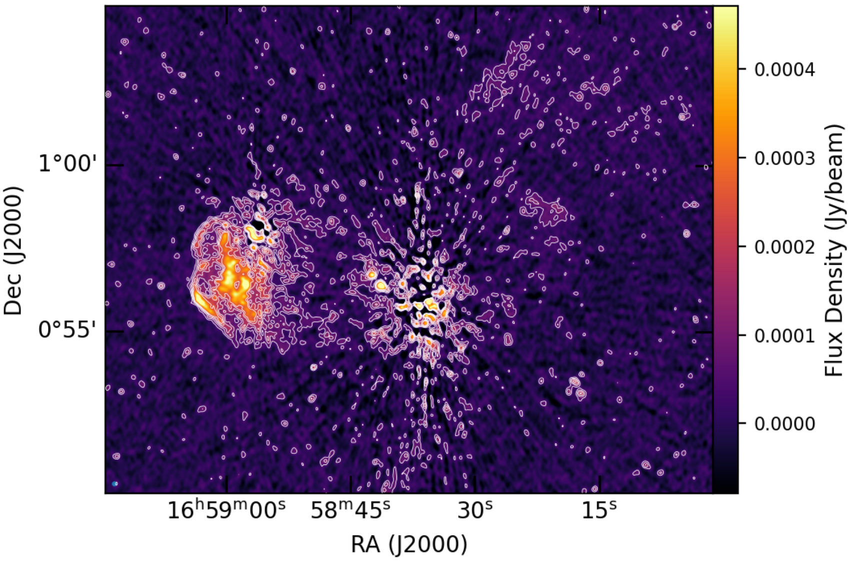

FIGURE 3.12: The large-scale extended diffuse emission around NGC 6240 after the subtraction of the bright discrete sources at robust -0.3. The apparent artefacts are mostly caused by calibration and imaging techniques, they are seen only around bright radio sources, and therefore, arise from these bright radio sources. The beam size of the image is $6''.9 \times 6''.9$ with position angle (PA) of -7.45 deg. The contour levels are set at 49, 98, 147, 196, and 245 μJy beam^{-1}.

3.2.3 Integrated spectral index

The spectral index of the radio sources are computed between two frequencies of the same region of the sky, and assumed to take the negative sign convention: $S_\nu \propto \nu^{-\alpha}$, where α is the spectral index and S_ν is the radiative flux density at a given frequency ν. Radio halos are typically characterized by their steepening radio spectra ($\alpha \gtrsim 1$)[1] ranging from 0.9 to 1.8, which is similar to the radio spectra of radio relics which range from 1.0 to 2.9 (Feretti et al., 2012).

Using 107 MHz bandwidth sub-band images centred at 1016, 1123, 1230, 1337, 1444 and 1551 MHz, we computed an integrated spectral index of ~ 2.9 for Source E. This is consistent with that of known relics in literature. We also computed the integrated spectral index using the lower and higher band frequencies (at 1016 and 1444 MHz) which is ~ 2.45. However, for accuracy reasons, we will use the integrated spectral index computed from all sub-band images since the first and last bands are not of sufficient quality. Due to calibration issues, we can not accurately compute the integrated spectral index of the extended diffuse emission, therefore we will adopt the spectral index values provided by (Feretti et al., 2012) for calculations.

3.2.4 Radio power at 1.28 GHz

To calculate the radio power of the extended diffuse emission and Source E, we use:

$$P_{1.28\text{GHz}} = \frac{4\pi D_{\text{L}}^2 S_\nu}{(1+z)^{1+\alpha}}, \tag{3.2}$$

where D_{L} (= 105 Mpc) is the luminosity distance at a redshift of $z = 0.0245$, S_ν is the source flux density at frequency ν, and $(1+z)^{1+\alpha}$ is known as the standard k-correction. The spectral index ($\alpha_{\text{sourceE}} \sim 2.9$ for Source E and $\alpha_{\text{ext}} \sim 1.0$ - 1.8 for the extended diffuse emission) in this equation is assumed to be of negative sign convention. The measured total flux density of the extended diffuse emission is ~ 62 mJy, split into ~ 13 mJy for the extended diffuse emission and ~ 49 mJy for Source E. Using the above values, we estimate the radio power of $\sim 1.67 \times 10^{22}$ W Hz^{-1} for the extended diffuse emission and $\sim 6.3 \times 10^{22}$ W Hz^{-1} for Source E at 1.28 GHz.

---

[1] Assuming $S_\nu \propto \nu^{-\alpha}$ throughout the thesis.

3.2.5 Comparing Source E with known radio phoenix/relics

In this section, we compare the properties of Source E with known relics to understand its nature by use of plots that demonstrates the correlation between the largest angular sizes (LAS) and M_{500} of relics/phoenix with their radio power at 1.4 GHz. The sources in the plots, as well as their LAS, redshift and M_{500} values were taken from the Galaxy Clusters Database[2] in addition to uniform resource citation (URC), van Weeren et al. (2019).

The morphology of Source E resembles that of known radio phoenix/AGN relics and radio shocks. For instance the morphology of Source E compares to that of the Toothbrush Cluster, and Abell 85 shown in figures 1.7 and 1.8. However, there is a LAS difference between Source E and the two sources mentioned above. We are attempting to figure out what the nature of the source is, and one piece of evidence is how it compares with known/already classified objects. Source E is in a much lower mass system ($\sim 1.1 \times 10^{11}$ $M_{\odot}$, estimated in Section 4.1.5) compared to the two sources mentioned above. de Gasperin et al. (2014) and Nuza et al. (2017) reported that there is a strong association between X-ray luminosity and radio power which shows that clusters that are more massive could produce more luminous radio relics.

The scaling mentioned above is explored in figures 3.13 and 3.14, which shows the radio power versus cluster mass of Source E with other well known radio relics and phoenices. From both figures 3.13 and 3.14, we can see that the most luminous radio relics and phoenices are hosted by clusters that are more massive. The similar trend is observed in the results of Nuza et al. (2017). Therefore, the low radio power of Source E is likely due to its lower mass (estimated in Section 4.1.5), and the location of NGC 6240 in this parameter space is qualitatively consistent with what we would expect based on the known correlation. However, it is also worth noticing that some of the more massive clusters host relics and phoenices with similar radio power as those with lower mass (e.g., Source E).

Nuza et al. (2017) reported that the normalization of radio power in relics/phoenix is much higher in more distant clusters, implying that at high redshift only the brightest relics/phoenix are detected in massive clusters. We also explore this trend by colorizing the data points of the radio relics and phoenices by their redshifts in figures 3.13 and 3.14. Here we see that, most radio relics and phoenices in lower masses exhibit lower redshifts with both high and low radio powers, whereas those in more massive clusters exhibit higher redshifts with higher radio powers, which is of course a sensitivity and angular resolution selection effect. The position of Source E in both figures 3.13 and 3.14 indicates that with MeerKAT and LOFAR we are also reaching previously unexplored dark matter halos with lower mass (e.g., Botteon et al. 2021), which have been missed by prior observing instruments.

Several authors have reported the correlation between largest linear size (LLS) and radio power of relics (e.g., Feretti et al. 2012; Bonafede et al. 2012). This is shown in figures 3.15 and 3.16, where we include the radio power of Source E versus largest angular size (LAS) with known radio relics and phoenices. In these figures, Source E appears to be broadly consistent with this correlation to that of known radio relics and phoenices, however, NGC 6240's low mass places it in a fairly isolated location of this parameter space, requiring further discoveries for meaningful statistical comparison.

---

[2] https://galaxyclusters.hs.uni-hamburg.de

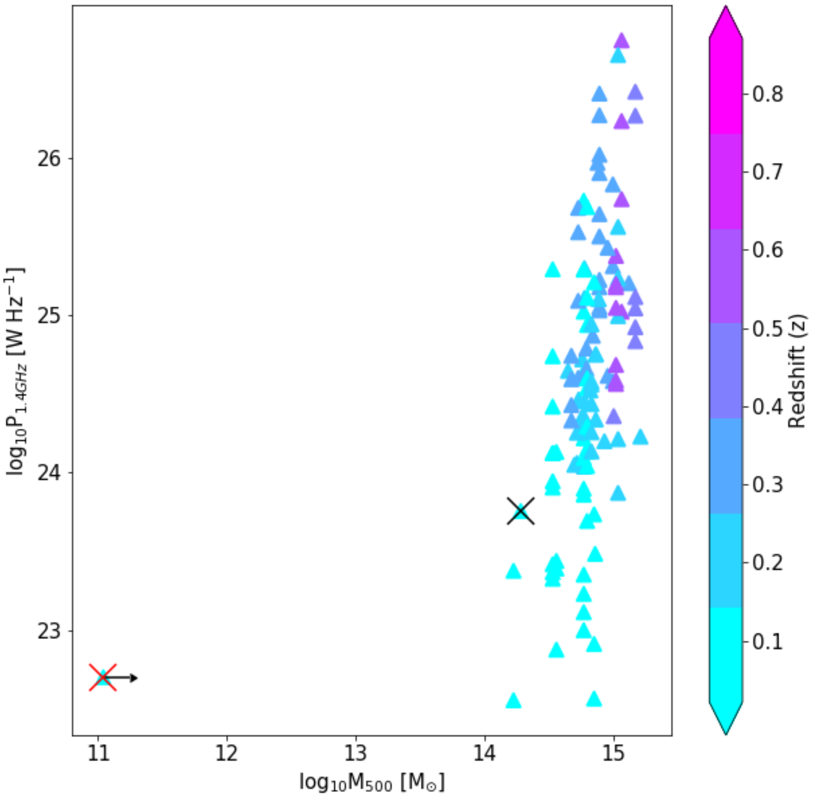

FIGURE 3.13: Radio relic $P_{1.4}$-M_{500} relation diagram. The different colors denote the redshifts of the sources. The red X mark is used to position Source E and the black X mark indicates the position of the radio relic detected with LOFAR in PSZ2G145.92-12.53 ($z = 0.03$). The mass of Source E is considered a lower limit, as denoted by the arrow (see Section 4.1.5 for more details).

Overall, the correlation drawn from these plots suggest that Source E can be classified within a known class of radio relics and phoenices.

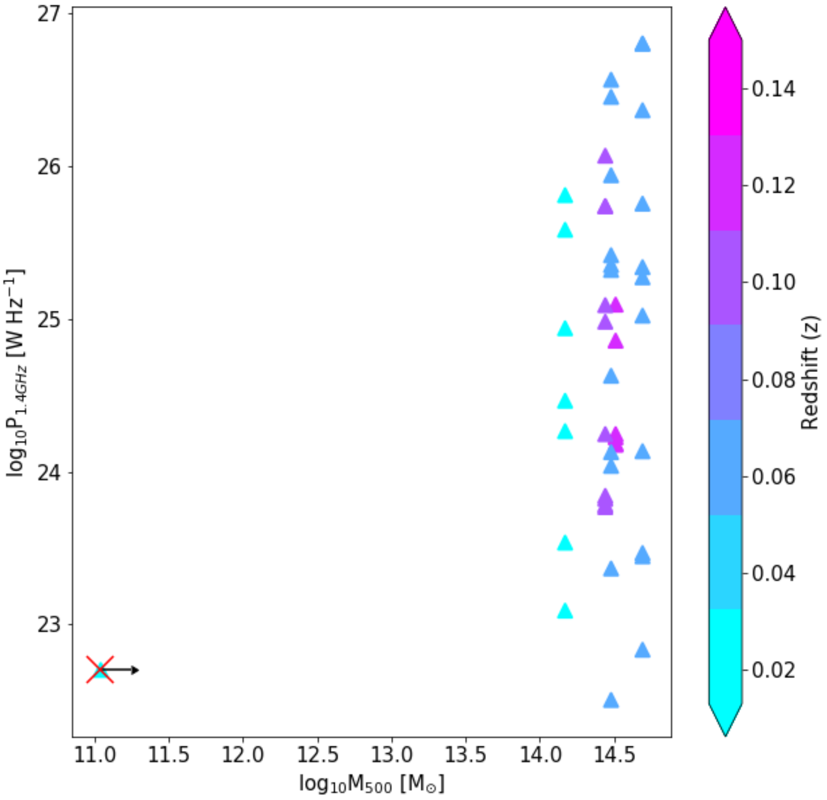

FIGURE 3.14: Radio phoenix $P_{1.4}$-M_{500} relation diagram. The different colors denotes the redshifts of the sources. The red X mark is used to position Source E. The mass of Source E is considered a lower limit, as denoted by the arrow (see Section 4.1.5 for more details).

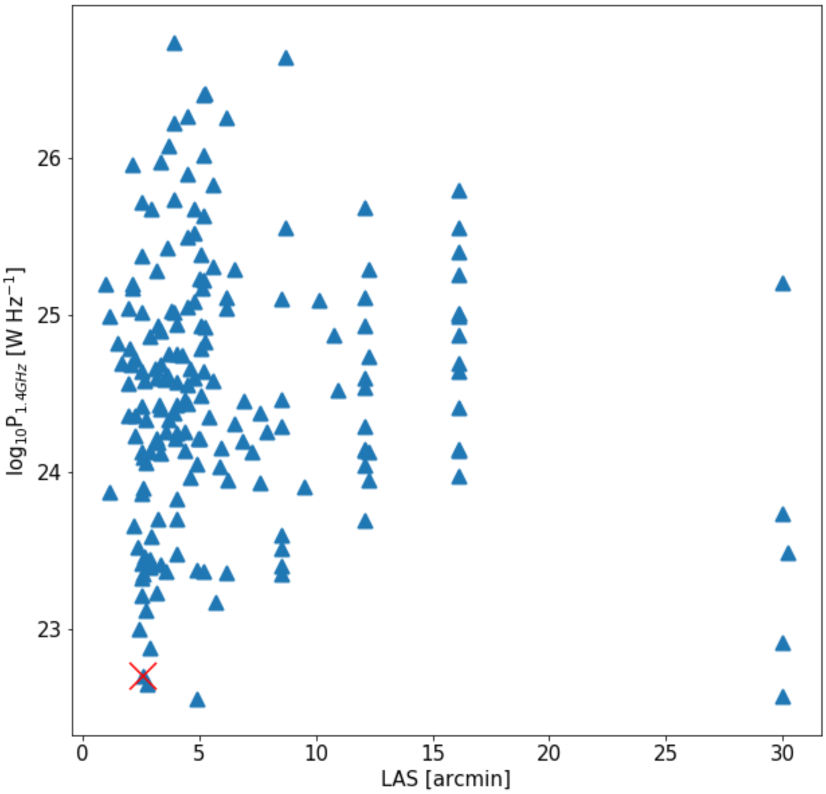

FIGURE 3.15: Radio power, $P_{1.4}$, vs. largest angular size, LAS, for the relic sample. The red X mark is used to position Source E. The radio relic detected with LOFAR is not included in this correlation because its largest angular size is unknown.

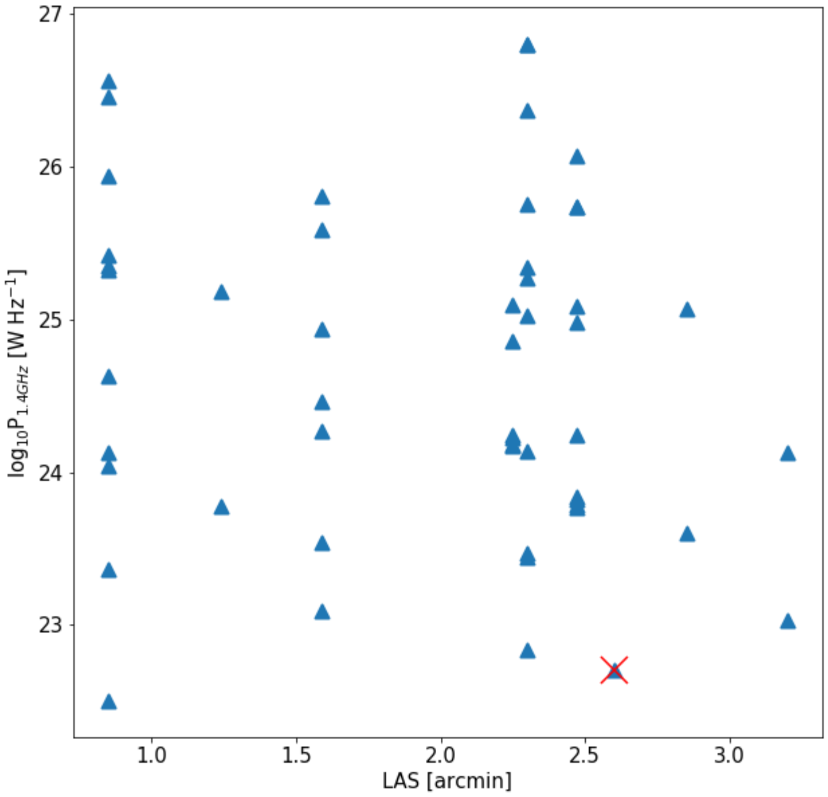

FIGURE 3.16: Radio power, $P_{1.4}$, vs. largest angular size, LAS, for the phoenix sample. The red X mark is used to position Source E. As can be seen, Source E is more consistent with regard to LAS, but still at edge of $P_{1.4}$ and at the very bottom corner of the parameter space, signalling the importance of discovery.

Chapter 4

Derived properties and discussion

4.1 Discovery of extended radio emission

Our MeerKAT images have made the discovery of extended diffuse emission centred on NGC 6240 with a projected extent of ∼ 300 kpc. The extended diffuse emission seems to permeate from the post-merger (Müller-Sánchez et al., 2018) centre of NGC 6240 (labelled NGC 6240 core; fig 3.6), and extends in a predominately east-west direction. At the eastern side of the post-merger centre, lies the extended radio source (labelled Source E; fig 3.6). Source E extends from north to south, consisting of two shock fronts (although they can be contiguous) at the eastern extreme (labelled Shock 1 and 2; fig 3.6), four bridges (labelled 1 - 4; fig 3.6) and a central filamentary structure.

Source E has the angular size of $\sim 4' \times 3'$, giving a physical length of ∼ 107 kpc and width ∼ 80 kpc (assuming a distance of 105 Mpc), whereas the angular size of the the extended diffuse emission is $\sim 10' \times 5'$, giving a linear size of ∼ 300 kpc at a distance of 105 Mpc. The geometry, location and size of Source E imply that it is a radio phoenix/shock/AGN relic associated with the NGC 6240 merger and past AGN activity, whereas that of the extended diffuse emission could be a halo, but this is difficult to decouple from the remnant jet emission, especially with bright central source and noticeable artefacts. The projected distance of Source E is ∼ 145 kpc from the centre of the NGC 6240 post-merger system, whereas that of the shock fronts at the edge of Source E is ∼ 225 kpc with respect to the centre.

4.1.1 Exclusion of the extended halo

Clearly, there are a number of interesting radio structures around the immediate core of NGC 6240 but due to calibration issues, we are unable to constrain the fidelity of the extended diffuse emission (halo). As shown in figure 3.12, there are calibration/imaging artefacts nearby bright radio sources, and the complex, spatially resolved structure of NGC 6240 itself, as well as the previously discussed effects of Hercules A beyond the primary beam. Therefore, we exclude the extended halo in our discussions and focus our attention mainly on Source E, which is mapped in high fidelity, and is arguably the radio feature of greatest scientific interest.

The results of this project provide a new view on the history of the post-merger system, NGC 6240, known as a key local representative of the ultraluminous infrared galaxies (ULIRGs). In the following sections we estimate physical quantities of NGC 6240, which are necessary to aid with the interpretation of the nature of the diffuse radio emission identified in our MeerKAT images for the first time.

4.1.2 Geometry assumption for emitting volume

We use volume calculations to estimate the emitting regions of the radio sources, which enables us to derive average estimates of magnetic field strengths in those regions (Bonafede, A. et al., 2009). The volume of the extended diffuse emission appears to be characterized by an ellipsoid with the major and minor axis,

$$V_{\rm ext} = \frac{4\pi}{3}abc \tag{4.1}$$

We assume that the semi-major axis is half the width of the extended diffuse emission (∼300/2 kpc), whereas the semi-minor axis is given by half the height of the extended emission (∼180/2 kpc), and the third axis is given by the mean between the major and minor axis (∼120 kpc; Bonafede, A. et al. 2009). Using the above values, we estimate a volume of 6.7×10^6 kpc^3 for the extended diffuse emission. For Source E we assume that the volume of the emitting regions is a prolate spheroid, for which the volume is given as,

$$V_{\rm sourceE} = \frac{4\pi}{3}ba^2, \tag{4.2}$$

where b = 54 kpc and a = 40 kpc, and we estimate an emitting volume of 0.36×10^6 kpc^3, similar with the emitting volumes of known relics/bubbles in literature (e.g,. Brienza et al. 2021).

4.1.3 Equipartition magnetic field

To estimate the equipartition magnetic field in the extended diffuse emission and Source E, we first assume that both the relativistic particles and magnetic field fills the entire volume of these radio sources and the energy content in their electrons is similar to that in their protons (e.g., Bonafede, A. et al. 2009). We adopt the minimum energy density (in erg cm^{-3}) formula from Govoni and Feretti (2004),

$$U_{\rm min} = \xi(\alpha,\nu_1,\nu_2) \times (1+k)^{4/7} \times (\nu_0)^{4\alpha/7} \times (1+z)^{(12+4\alpha)/7} \times (I_0)^{4/7} \times (d)^{-4/7}, \tag{4.3}$$

where $\xi(\alpha,\nu_1,\nu_2)$ is the equipartition constant which is a function of injection index α and frequency ranging from ν_1 to ν_2; k is the ratio of the energy in relativistic protons to that in electrons. The value of k depends on the mechanism of generation of relativistic electrons, therefore, we set k=1 for Source E and k=100 for the extended diffuse emission. I_0 (in mJy arcsec^{-2}) is the source's brightness at the frequency ν_0 (in MHz) and can be obtained by dividing the integrated flux density of the radio source (49 mJy for Source E and 13 mJy for the extended diffuse emission) by its solid angle ($210'' \times 157''$ and $585'' \times 300''$); z is the redshift of NGC 6240 at 0.0245; and d (in kpc) is the depth of the source (d=$\frac{107_{\rm kpc}+80_{\rm kpc}}{2}$ for Source E and d =$\frac{300_{\rm kpc}+154_{\rm kpc}}{2}$ for the extended diffuse emission).

The central frequency for MeerKAT L-band is 1283 MHz, therefore we set $\nu_0 = 1283$ MHz, and for a frequency range 10 MHz to 100 GHz (which covers our L-band), and the injection index of $\alpha_{\rm sourceE} \sim 2.9$ for Source E and $\alpha_{\rm ext} \sim 1.0$ - 1.8 for the extended diffuse emission, and using the relevant equipartition constants (see table 1; Govoni and Feretti 2004), we estimate that the $U_{\rm min}$ for Source E is $\sim 5 \times 10^{-13}$ erg cm^{-3} and $\sim$ 9 - 51 $\times 10^{-14}$ erg cm^{-3} for the extended diffuse emission respectively. The equipartition magnetic field is then obtained as,

$$B_{\rm eq} = \left(\frac{24\pi}{7}U_{\rm min})\right)^{1/2}. \tag{4.4}$$

Substituting the $U_{\rm min}$ values, we approximate that $B_{\rm eq}$ for Source E is ~ 2.3 μG and ~ 1 - 2.3 μG for the extended diffuse emission, consistent with that of known radio relics and halos (e.g., Parekh et al. 2020; Bonafede, A. et al. 2009; Govoni and Feretti 2004; Ensslin et al. 1997).

4.1.4 The lifetime of electrons

The characteristic lifetime of the synchrotron emitting electrons ($\gamma \sim 10^4$; GeV energy) due to electron synchrotron and IC energy losses (van Weeren et al., 2009) is given by,

$$t_{\rm age} = 1060\frac{B^{0.5}}{B^2 + B_{\rm IC}^2}[(1+z)\nu_{\rm b}]^{-0.5}[{\rm Myr}], \tag{4.5}$$

with B (=$B_{\rm eq}$) the magnetic field strength; $B_{\rm IC} = 3.25(1+z)^2$ the equivalent magnetic field strength of the microwave background, both in units of μG (e.g., Miley 1980; Slee et al. 2001); and $\nu_{\rm b}$ is the break frequency (in GHz), defined as the frequency above which the radio spectrum transitions from power law to exponential due to spectral aging, and usually exceeds ν_0, the observed frequency (Miley, 1980). Therefore, in our case we set $\nu_{\rm b} = 1.4$ GHz (the frequency at which the flux of the radio sources drops exponentially), and using the $B_{\rm eq}$ values, we estimate $t_{\rm age}$ to be ~ 75 Myr for the extended diffuse emission. For the case of Source E, if the energy density of the CMB ($U_{\rm CMB} = B_{\rm IC}^2/8\pi$) surpasses that of the magnetic field ($U_{\rm B} = B^2/8\pi$), then Inverse Compton (IC) losses dominates over synchrotron losses ($B = B_{\rm IC}$; Dunn et al. 2005), and for that case $B = B_{\rm IC}$ (= 3.4 μG in our case). Therefore, the estimated radiative age for Source E is ~ 79 Myr, consistent with the ages of known relic/bubbles in literature (e.g., Dunn et al. 2005).

These lifetimes are in agreement with the synchrotron lifetime of electrons, which ranges from $\sim 10^7$ - 10^8 years (Govoni and Feretti, 2004). This suggests that the main origin of the relativistic electrons need continuous injection processes and/ or re-acceleration processes in order to describe the long-lived diffuse synchrotron emission (Govoni and Feretti, 2004) seen in this case, which seems to be re-accelerated.

4.1.5 Mass and size of NGC 6240 dark matter halo

Under the greatly simplified assumption that the dark matter halo is virialized, we make use of the full examination of the correlation between central galaxies and their host dark matter halos, which is defined by the stellar mass-halo mass relation for $0 < z < 1$ from the work of Behroozi et al. (2010),

$$\log_{10}(M_{\rm h}(M_*)) = \log_{10}(M_1) + \beta\log_{10}\left(\frac{M_*}{M_{*,0}}\right) + \frac{\left(\frac{M_*}{M_{*,0}}\right)^{\delta}}{1+\left(\frac{M_*}{M_{*,0}}\right)^{-\gamma}} - \frac{1}{2}, \tag{4.6}$$

where M_1 is a characteristic halo mass, $M_{*,0}$ is a characteristic stellar mass, M_* is the stellar mass, β is the low mass-end slope, and δ and γ control the massive-end slope. For $0 < z < 1$ and unknown free absorption parameters ($\mu = \kappa = 0$), $M_{*,0}$, M_1, β and δ and γ values are given in table 2 of Behroozi et al. (2010), and the stellar mass of NGC 6240 ($M_{\rm stellar} \sim 2 \times 10^9$ $\rm M_\odot$) is adopted from Tecza et al. (2000), using the above we estimate the stellar mass-halo mass of $\rm M_h(M_*) \sim 1.1 \times 10^{11}$ $\rm M_\odot$. The estimated stellar mass-halo mass corresponds to $\rm M_{200}$ (the mass within a sphere with mean density above $200\rho_{\rm crit}$). However, as the diffuse radio emission and post-merger appearance suggest, NGC 6240 is very unlikely to reside in an isolated halo, but is more realistically part of a cluster environment with significantly larger mass. So in reality, the mass value will be higher, but we don't have an obvious way to measure it with observations in hand, therefore, we call the calculated mass above a lower limit.

To calculate r_{200}, we adopt the virial mass (the mass within $r_{\rm vir}$) equation from Coe (2010),

$$M_{\rm vir} = \frac{4}{3}\pi r_{\rm vir}^3 \Delta_{\rm c} \rho_{\rm crit}(z), \tag{4.7}$$

where $\rho_{\rm crit}(z)$ is the critical density of the universe at $z = 0$ ($\sim 9.1 \times 10^{-27}$ kg m^{-3}), $\Delta_{\rm c}$ is the overdensity constant and $r_{\rm vir}$ is the virial radius. For an overdensity constant of $\Delta_{\rm c} \sim 200$ (corresponding to our $\rm M_{200}$), using the above and solving for r_{200} we get $r_{200} \sim 100$ kpc. The r_{200} quantity indicates the radius in which the mean density (of the galaxy) is 200 times the cosmological background density at that redshift (Chun et al., 2020), and is comparable to the distance between the Source E shock front and NGC 6240 nucleus.

4.2 The eastern radio shock (Source E)

4.2.1 Size, projected distance and radio power

Source E is modelled as a prolate spheroid with semi-axes of lengths 40 kpc and 54 kpc, which yields an emitting volume of $\sim 0.36 \times 10^6$ kpc^3. It is located ~ 145 kpc east of the postmerger system of NGC 6240. Its projected distance (~ 145 kpc) with respect to the centre of NGC 6240, suggest that Source E can be classified within a known class of radio relics and phoenices (e.g., Kempner et al. 2004). The width of Source E is ~ 80 kpc and its length is ~ 107 kpc, respectively. The physical sizes of Source E are consistent with that of known AGN relics/radio phoenix. Slee et al. (2001) reported a radio phoenix/AGN relic found in A4038 with a large linear size of ~ 130 kpc, and Komissarov and Gubanov (1994) reported one from A2063 with a large linear size of ~ 40 kpc. The shape of Source E takes a form of an arc-like structure, and its radio power is estimated to be $\sim 6.3 \times 10^{22}$ W Hz^{-1} at 1.28 GHz, which is about 1 order of magnitude below the typical radio power of known AGN relics/radio phoenices, but matches that of the AGN relic/radio phoenix found in A4038 (Slee et al., 2001). The low radio power of these revived fossil plasma sources is believed to be related to their estimated distance from the central cluster (Feretti et al., 2012). Source E is much closer to the centre of NGC 6240, and it is believed that there are low efficiency shocks ($\mathcal{M} \lesssim 3$) towards the centre as compared to the peripheral regions where the Mach numbers ($\mathcal{M} \gtrsim 3$) are high enough to supply energy to radio emitting particles (Blasi and Gabici, 2003).

Within Source E, a filament is detected, extending from north to south and it appears to be as bright as Shock 1. The filament also appears to be associated with

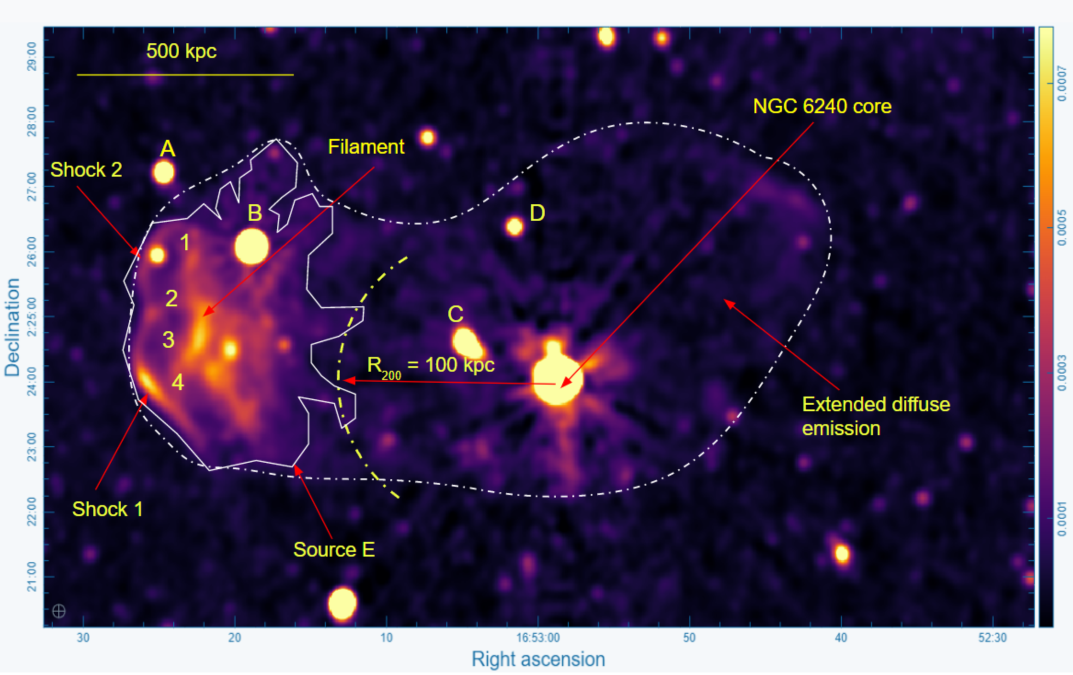

Figure 4.1: The reference figure shown in the results chapter.

the two shocks via the bridges shown in fig 3.6, and has a similar size to the eastern shock front. The filament's brightness and its association with the two shocks is discussed in more detail in subsection 4.2.5.

4.2.2 Spectral indices and magnetic fields of known radio phoenices/relics

The integrated spectral index computed for Source E is in agreement with the spectral index values for the relics found in galaxy clusters A85, A4038 and A13 which are computed between 1.385 and 1.465 GHz (Slee et al. 2001; Feretti et al. 2012). For the relic in A2744, Govoni et al. (2001) reported the spectral index of > 2 between frequencies 1365 and 1435 MHz. Studies have shown that various clusters hosting radio halos or relics, exhibit equipartition magnetic fields of order $\sim 1\ \mu$G (eg,. Govoni and Feretti 2004). For Source E, we estimated the magnetic field strength of $\sim 2.3\ \mu$G, which is similar to values estimated for known relics. For example, Govoni et al. (2001) derived a value of $> 1.9\ \mu$G for the relic in A2744.

4.2.3 Thermal and non-thermal pressure

Thermal pressure refer to the pressure exerted by the intergalactic medium (intragroup or intracluster medium depending on the environment) on the AGN lobes/jets. In contrary, non-thermal pressure refer to the pressure exerted by the AGN lobes/jets on the surrounding environment. For the non-thermal pressure, we adopt the minimum relativistic pressure formula from Cotton et al. (2020),

$$p_{\rm min} = \frac{13B^2_{\rm min}}{72\pi}(1+k)^{4/7}, \tag{4.8}$$

where $B_{\rm min}$ is the magnetic field strength of Source E ($\sim 2.3\ \mu$G) and k is the protron-to-electron ratio, which is set to k=1 for Source E. We then estimate the non-thermal pressure of $P_{\rm min} \sim 4.5 \times 10^{-13}$ dyne cm^{-2}, which is in agreement with the non-thermal pressure of known relics/bubbles (e.g., Slee et al. 2001; Brienza et al. 2021).

For the thermal pressure, we adopt the formula used by Brienza et al. (2021),

$$p_{\mathrm{th}} = 1.9 n_{\mathrm{e}} kT, \tag{4.9}$$

where the electron density is $\sim 2.5 \times 10^{-3}$ cm^{-3} and a temperature of 7.5×10^{6} K (0.65 keV), as obtained from the X-ray data by Nardini et al. (2013) for the hot halo gas in NGC 6240. Assuming $n_e \sim n_H$, the electron density was extracted from the emission measure ($EM = n_e^2 \eta \mathcal{V}$; Nardini et al. 2013), defined as the square of the number density of free electrons integrated over the volume of the plasma. We assume the same values hold for Source E since it is embedded in the halo, however, this is simply indication given the significant distance of Source E from available X-ray detections. Using the above, we estimate a thermal pressure of $P_{\mathrm{th}} \sim 4.9 \times 10^{-12}$ dyne cm^{-2}. However, it is believed that the pressure of intracluster medium falls by a factor of two as the bubble rises through it, and this factor results from the drop in the number of particles at the location of the bubble (e.g., Dunn et al. 2005; Brienza et al. 2021). Therefore, this drop by a factor of 2 results in a thermal pressure of $P_{\mathrm{th}} \sim 2.9 \times 10^{-12}$ dyne cm^{-2}, similar to the thermal pressure of known relics/bubbles (e.g., Dunn et al. 2005; Juett et al. 2008; Brienza et al. 2021).

We note that the thermal pressure of Source E exceeds that of the non-thermal pressure by one order of magnitude, implying that non-radiating particles, particularly protons, dominate the energetics of Source E structure (e.g., Brienza et al. 2021). This is also supported by the fact that the energy density of the $z = 0.0245$ CMB ($\sim 4.6 \times 10^{-13}$ erg cm^{-3}) exceeds that of the magnetic field ($\sim 2.1 \times 10^{-13}$ erg cm^{-3}), which suggest that Inverse Compton (IC) losses dominates over synchrotron losses. There are, of course, large uncertainties associated with derived properties, however, this exploration sets the scene for future, more precise analyses enabled multi-frequency observations of this discovery.

4.2.4 Radio shock(s) and Mach number

From the standard DSA formula (Eckert et al., 2016), the Mach number for Diffuse Shock Acceleration is given by,

$$\mathcal{M} = \left(\frac{2\alpha + 3}{2\alpha - 1} \right)^{1/2}. \tag{4.10}$$

Given the integrated spectral index of Source E to be $\alpha_{\mathrm{sourceE}} \sim 2.9$, and assuming that all the electrons are newly accelerated and ignoring cooling losses (Eckert et al., 2016), we attain a Mach number of $\mathcal{M} \sim 1.4$, similar with the Mach number of known relics (e.g., Parekh et al. 2020; Eckert et al. 2016; Hoang et al. 2017).

However, if we adopt the work of (Drury, 1991), the Mach number for Diffuse Shock Acceleration is given by,

$$\mathcal{M} = \left(\frac{2\alpha_{\mathrm{inj}} + 3}{2\alpha_{\mathrm{inj}} - 1} \right)^{1/2}, \tag{4.11}$$

where α_{inj} is the injection index, which is the average spectral index at the location of the shock. The injection index is flatter than the integrated spectral index by 0.5, which is the expected injection index of young cosmic ray electrons from the theory of DSA (Kardashev, 1962; Bell, 1978).

$$\alpha_{\text{int}} = 0.5 + \alpha_{\text{inj}}. \tag{4.12}$$

This works if we assume that the observed emission is dominated by aged electrons formerly accelerated by the same shock, then the radio spectrum is akin to the injection spectrum (see Equation 4.12), which using Equation 4.11 gives a Mach number of $\mathcal{M} \sim 1.5$, which is in agreement with values found for known relics (e.g., Eckert et al. 2016). Note that the Mach numbers are weak (i.e. $\lesssim 3$, low efficiency shocks) for both the fresh ($\mathcal{M} \sim 1.4$) and old ($\mathcal{M} \sim 1.5$) electrons.

4.2.5 The nature of Source E

In this section, we explore several physical models of the underlying nature of the shock front Source E, synthesizing the derived properties presented earlier.

First-order Fermi: Source E traces a complex shock surface along the line of sight

We consider the process of First-order Fermi, also known as the Diffuse Shock Acceleration (DSA). For this process, the acceleration occurs diffusively, that the particles in Source E scatter back and forth across the shock, gaining at each crossing and recrossing an amount of energy proportional to the energy itself, and the shock Mach number determines the acceleration efficiency (Feretti et al., 2012). It has been reported that this scenario requires an implausibly high efficiency of electron acceleration for low/weak Mach numbers ($\mathcal{M} \lesssim 3$; Kang and Ryu 2011; Botteon et al. 2020; ZuHone et al. 2021). Since we consider the electrons in Source E to be freshly accelerated, we derived a Mach number of $\mathcal{M} \sim 1.4$, which is very weak. Shock waves produced by powerful merger shocks typically exhibit Mach numbers ranging from $\mathcal{M} \sim 2$ - 3 (van Weeren et al., 2019). However, such merger shocks are insufficient to accelerate particles (cosmic) from the thermal pool to relativistic energies (Kang and Ryu, 2011; Kang et al., 2012). Therefore, the First-order Fermi process (DSA) is ruled out to explain the mechanism behind the nature of Source E. Basically, DSA is effective in accelerating thermal particles at high Mach numbers (Bell, 1978; Drury, 1983).

Radio Phoenix/Shock: Source E emission is generated by a re-accelerated population of fossil particles from a radio galaxy

Even though shocks with weak Mach numbers are ineffective in increasing particles from the thermal pond, they are sufficiently effective to re-accelerate cosmic rays from previous radio galaxy activity (Bonafede et al., 2014). In this scenario, we treat Source E as a synchrotron buoyant bubble that originated from prior active phase of a radio galaxy before its activity ceased (Shulevski et al., 2015). The birth of this synchrotron buoyant bubble is explained in AGN relic interpretation below.

The most commonly used approach for estimating the velocity of a rising bubble can be attained by equating the buoyancy forces and ram pressure on a bubble (Gull and Northover, 1973), which yields a terminal velocity of,

$$v_{\text{terminal}} = \sqrt{g \frac{4r}{3} \frac{2}{C}}, \tag{4.13}$$

where r is the radius of Source E ($\sim$ 40 kpc), g is the gravitational acceleration constant and C is the drag coefficient, $C_{\mathrm{drag}} \sim 0.75$, adopted from Churazov et al. (2001), who obtained it based on hydro-dynamical simulations of buoyant bubbles travelling through a compressible and stratified medium. Using the above values we estimate a terminal velocity of $\nu_{\mathrm{terminal}} \sim 540$ km s^{-1}. However, this terminal velocity expression can be adjusted using the Keplerian velocity at a specific distance from the central galaxy/cluster,

$$v_{\mathrm{b}} = \sqrt{\frac{r}{R}\frac{8}{3C}}.v_{\mathrm{k}}, \tag{4.14}$$

where R ($\sim$ 185 kpc) is the distance of Source E centre from the NGC 6240 nucleus, $v_{\mathrm{k}} = \sqrt{gR}$ is the Keplerian velocity at the distance of the Source E. Using the above values, we estimate the Keplerian velocity of $v_{\mathrm{k}} \sim 616$ km s^{-1}, which in turn gives the buoyancy velocity of $\nu_{\mathrm{b}} \sim 539$ km s^{-1}. This buoyancy velocity is similar to the buoyancy speeds of other known bubbles in literature (e.g,. Juett et al. 2008; Shulevski et al. 2015; Ogrean et al. 2011; Brienza et al. 2021). Therefore, the rising time of Source E can be estimated as,

$$t_{\mathrm{buoy}} = \frac{R}{\nu_{\mathrm{b}}}, \tag{4.15}$$

which gives us $t_{\mathrm{buoy}} \sim 335$ Myr, consistent with the time scales taken by other bubbles to rise buoyantly to their current positions (e.g., Ogrean et al. 2011; Brienza et al. 2021). Brienza et al. (2021) used the argument that the sound speed can provide the upper limit to the bubble velocity, which can be approached in case the bubble size is comparable with the height scale of the atmosphere. We adopt the adiabatic sound speed of $v_{c_{\mathrm{s}}} \sim 420$ km s^{-1}, derived from a hot halo gas of NGC 6240 with $kT \simeq 0.65$ keV (7.5×10^{6} K), and mean molecular weight $\mu \simeq 0.6$ (Nardini et al., 2013). The adopted sound speed implies a rising time of $t_{cs} \sim 186$ Myr for Source E, consistent with the minimum rising times for the bubbles reported by Brienza et al. (2021). These rising times are expected to be roughly consistent with the radiative age of relic/bubble obtained via spectral fitting (Slee et al., 2001). It is worth noting that the rising times of Source E are higher than the synchrotron lifetime of electrons, which is $\sim$ 100 Myr.

From the rising time of Source E, we can estimate its mechanical power using the formula adopted from Brienza et al. (2021),

$$P_{\mathrm{bubble}} = \frac{p_{\mathrm{th}} V_{\mathrm{bubble}}}{t_{\mathrm{buoy}}}, \tag{4.16}$$

where thermal pressure is $p_{\mathrm{th}} \sim 2.9 \times 10^{-12}$ dyne cm^{-2} and the volume of Source E is $V_{\mathrm{bubble}} \sim 0.36 \times 10^{6}$ kpc^{3}. Using the above values and the estimated rising time, we estimate the thermal power of $P_{\mathrm{bubble}} \sim 2.8 \times 10^{42}$ erg s^{-1} for Source E, which is similar to the power of other known bubbles (e.g., Dunn et al. 2005 ; Brienza et al. 2021). In contrast, the X-ray luminosity of NGC 6240 halo is $\sim 4 \times 10^{41}$ erg s^{-1} (Nardini et al., 2013), but physically decoupled from the thermal power.

The estimated Mach number for Source E is $\mathcal{M} \sim 1.4$ (very weak), and given that Source E is embedded in the radio halo, we can use the sound speed $v_{c_{\mathrm{s}}} \sim 420$ km s^{-1} derived from Nardini et al. (2013) together with the Mach number to estimate the velocity of the shock,

$$v_{\mathrm{shock}} = \mathcal{M} v_{c_{\mathrm{s}}} \approx 600 \text{ km s}^{-1}. \tag{4.17}$$

Assuming that this shock velocity remained constant, we then use this relation $R/v_{\rm shock}$, and estimate that the shocks took 300 Myr (0.3 Gyr) to travel from merger centre to their current locations (shown in figure 4.1). This shock timescale is comparable to that reported by Bonafede et al. (2014) for the NW relic emission with a large linear size of $\sim$ 2 Mpc in galaxy cluster PLCKG287.0+32.9. Furthermore, we estimate the time it took the shocks to cross the Source E/fossil cloud to their observed edge positions, using the formula adopted from Mhlahlo et al. (2017),

$$t_{\rm cross} = 32.6{\rm Myr}\left(\frac{L_{\rm cloud}}{100{\rm kpc}}\right)\left(\frac{v_{\rm shock}}{3000{\rm km\ s^{-1}}}\right), \tag{4.18}$$

where $L_{\rm cloud}$ (= 185 kpc) is the distance from Source E centre to the merger and $v_{\rm shock} \sim 600$ km s^{-1}, using these values we estimate the cross time of $t_{\rm cross} \sim 12$ Myr. This suggest that out of the 300 Myr, it only would have taken the shocks 12 Myr to cross the entire Source E/fossil cloud.

Now, it is worth noting that the time it took the shocks to reach their current position is shorter than the buoyancy rise time of Source E, implying that the population of fossil/mildly relativistic electrons was formerly present before the merger shocks propagated. The shocks are 35 Myr younger than the rising time of Source E, suggesting that the shocks traveled to their current peripheral positions 35 Myr later to re-trigger/re-accelerate pre-existing electrons of Source E or what is left of the AGN burst emission, and thus forming a radio phoenix and radio shock (e.g., Kempner et al. 2004 and van Weeren et al. 2019 for classification review) or turning Source E into a radio phoenix with a prominent radio shock.

The past AGN remnant phenomena can be supported by the ratio of the non-thermal pressure to thermal pressure of Source E ($p_{\rm min}/p_{\rm th} \sim 0.15$), which is less than 1, consistent with the typical ratio of non-thermal pressure to thermal pressure derived in FR-I radio galaxies (e.g., Croston et al. 2018; Brienza et al. 2021). This implies that Source E could be the remnant of the FR-I radio galaxy, whose activity has ceased/shutdown, hence it is no longer visible. It is also possible that this AGN remnant gained energy through the adiabatic compression by the merger shocks (e.g., Enβlin and Gopal-Krishna 2001) or it could be driven by the merger of the two dark matter halos and subsequent sloshing of baryons after that (Fabian, 1999).

Source E exhibits both the characteristics of a radio phoenix and that of a radio shock. However, Source E does not fall under the criteria of radio shocks in terms of its projected distance from the centre of NGC 6240 and its linear size. Source E is both smaller in size and closer to the centre compared to normal radio shocks, but it is located in a lower mass system ($\sim 1.1 \times 10^{11}$ M$_\odot$), and the plasma contained within it are lower by at least two orders of magnitude compared to known, classified radio shocks in literature, hence we also consider it a radio shock.

The above interpretation is supported by the work proposed by prior authors, for example, Bonafede et al. (2014) reported that since not all merging galaxy clusters consist of radio relics, then a shock wave is not enough to explain the radio emission by itself, it requires that a pond of pre-accelerated cosmic rays be present at the location of the relic. Sarazin (1999) proposed that it is difficult for low Mach number shocks to accelerate electrons from the ICM thermal pond in the presence of merging clusters, nevertheless, they may succeed in amplifying the energy of a pre-existing population of relativistic electrons to observable regimes. In galaxy clusters, relics are considered as the indication of re-accelerated fossil relativistic electrons, instead of direct injection from the thermal pool (Ensslin et al. 1997; Giacintucci et al. 2008; Kang and Ryu 2011; Kang et al. 2012; van Weeren et al. 2012; Pinzke et al. 2013). It was expected that the low Mach number shocks derived for Source E, would find it difficult to accelerate electrons from the intracluster medium thermal pool as NGC 6240 is a merging galaxy system.

The association between the filament and the two shocks

The logical explanation is that during the 12 Myr period, when the shocks were crossing Source E, they encountered the filament and engaged in some sort of interaction. The interaction was so strong that even after the crossing period was over, the interaction still holds by means of the four bridges shown in fig 3.6. This gives the filament the advantage to be more re-triggered/re-accelerated than the rest of Source E, since the filament seems to be feeding energy from the two shocks through the bridges.

Dynamic timescale of the shock

To calculate the dynamical time of the shocks, we adopt the following equation from Müller-Sánchez et al. (2018),

$$t_{\rm dyn} = \frac{D}{v_{\rm out}}, \tag{4.19}$$

where D is the size of the shocks and $v_{\rm out}$ is the shock velocity. The width of Shock 1 is $\sim$ 11 kpc and $\sim$ 4.6 kpc for Shock 2. With the estimated shock velocity of $\sim$ 600 km s^{-1}, we obtain $\sim$ 17 Myr for Shock 1 and $\sim$ 7 Myr for Shock 2, respectively. The timescales for both shocks are consistent with the timescale of the active phase of an AGN and also agrees with the age of the recent starburst in NGC 6240 (e.g., Müller-Sánchez et al. 2018).

AGN relic: Passively evolving fossil plasma from ceased AGN

Brocksopp et al. (2007) have reported that the behaviour of FR II radio galaxies is characterized by the release of highly laminar, collimated jets from the central core. These jets are able to travel supersonically away from the central core, and they decelerate as they move further away from the core due to ram pressure of the intergalactic medium (IGM; Brocksopp et al. 2007). This deceleration is believed to cause a bow shock, driven through the intergalactic medium, capable of inflating big cocoons of low density material and part of this large cocoons are what we observe as radio loops (Brocksopp et al., 2007). However, for our case we have shown (in scenario 2) that the ceased radio AGN that inflated the bubble was likely of FR I type (Fanaroff and Riley, 1974), using the non-thermal to thermal pressure ratio.

Taking the work of ZuHone et al. (2021) into consideration, it is possible that Source E not only traces the intracluster medium shocks but also non-uniform distribution of the seed cosmic ray electrons (CRe). We assume that the distribution of these cosmic ray electrons arose from the ceased AGN (presumably FR I radio galaxy) and perhaps other nearby galaxies, and the CRe were subsequently transported throughout by the gas motions influenced by the merger (e.g., ZuHone et al. 2021). Presumably, the central core AGN in the FR I radio galaxy fired jets out (in opposite directions), generating highly magnetized buoyant bubbles, as discussed in scenario 2. As they rise, the bubble's material is advected by the gas motions driven by the merger and in time the material of the bubble mixes with the intracluster medium, and therefore, giving rise to filamentary shape that resemble radio relics (e.g., Mathews and Brighenti 2008; ZuHone et al. 2021).

The ram pressure of the fired jets is believed to be balanced by the ram pressure of the receding external medium in front of the flow, and the interaction of the jet and its environment produces a powerful shock at the end of the jet and a bow shock in the external gas (Brocksopp et al., 2007). However, we do not detect any bow shock in our image, but it might have faded away over the years. It is believed that this bow shock compresses the bubble material and also to have the capability of re-accelerating relativistic particles (Markevitch et al., 2005; Brocksopp et al., 2007). Therefore, it is likely that the electrons in the relic are accelerated by both the merger shocks and the shocks from the old radio jet.

4.3 The extended diffuse emission

4.3.1 Radio power, morphology and size

As described in subsection 4.1.2, the extended diffuse emission is modelled as an ellipsoid with axes of lengths 90 kpc, 150 kpc and 120 kpc, which yields an emitting volume of $\sim 6.7 \times 10^6$ kpc^3. This volume covers a projected linear size of $\sim$ 300 kpc, which is within the sizes of known mini-radio halos (e.g., van Weeren et al. 2019). The radio mini-halo in Perseus was reported to have a linear size of $\sim$ 300 kpc, with an estimated radio power of $\sim 4.4 \times 10^{24}$ W Hz^{-1} at 1.5 GHz by Sijbring (1993). Giovannini and Feretti (2000) reported a mini-halo found in A2142, with a linear size of $\sim$ 270 kpc and a radio power of $\sim 6.6 \times 10^{23}$ W Hz^{-1} at 1.4 GHz. Another mini-halo with a linear size of $\sim$ 550 kpc and a radio power of $\sim 15.6 \times 10^{23}$ W Hz^{-1} at 1.4 GHz was reported by Bacchi et al. (2003). While the linear size of our extended diffuse emission agrees with that of mini-halos, its radio power differs significantly. We estimated a radio power of $\sim 1.67 \times 10^{22}$ W Hz^{-1} at 1.28 GHz for the extended diffuse emission, which is about one order of magnitude less to that of known radio mini-halos. As stated in subsection 4.1.1, we are unable to constrain the fidelity of the extended diffuse emission, therefore, we do not classify it.

The r_{200} scale of the dark matter halo is indicated in figure 3.6, and it shows that NGC 6240 is not positioned in the centre of the detected diffuse emission. Figure 3.6 also shows that about three quarters of the one-sided AGN relic is positioned within the r_{200}, which includes the entire filamentary structure but precludes the two shocks and some of the bridges. Therefore, the AGN relic extends fractionally beyond the r_{200}.

4.3.2 Compact radio sources within the diffuse emission

In figure 3.6, we detect discrete bright radio sources that are joined with both the extended diffuse emission and the relic. The first bright 4.5 mJy source (labelled C; RA $16^h\ 53^m\ 04.7^s$, DEC $2^\circ\ 24'\ 37''$) is located closer to the merger centre, the second bright 60 mJy source (labelled B; RA $16^h\ 53^m\ 19.0^s$, DEC $2^\circ\ 26'\ 05''$) is located closer to the relic, the third bright 3.1 mJy source (labelled A; RA $16^h\ 53^m\ 24.7^s$, DEC $2^\circ\ 27'\ 16''$) is located above the relic, and finally the fourth bright 1.62 mJy source (labelled D; RA $16^h\ 53^m\ 01.6^s$, DEC $2^\circ\ 26'\ 23''$) is located north of NGC 6240.

4.4 The loop structure to the west (western arm)

The integrated flux density our 1.28 GHz image shown in figure 3.2 is 384 mJy, with a peak value of 179 mJy beam^{-1}. This 1.28 GHz image is consistent with the prior L-band (A and B- array configuration) observations of the nuclear structure of NGC 6240 obtained by Baan et al. (2007) and Colbert et al. (1994). In fact, the integrated flux density in our 1.28 GHz high resolution map is very close to that obtained by Colbert et al. (1994), which is 386 mJy at 1.4 GHz. However, compared to the findings of Baan et al. (2007), our integrated flux density is higher by 13.5%, this may result from their use of a higher frequency (1.6 GHz) for their high resolution map. The latter suggest an increase of flux density at lower frequency which implies a steepening spectral index for the western arm (e.g., Colbert et al. 1994).

TABLE 4.1: Flux comparisons of compact NGC 6240 components

Component	**Frequency** (GHz)	**Flux** (mJy)	**Peak flux** (mJy beam^{-1})	**Observations**
Loop structure	1.28	110 ± 11	38.6	MeerKAT (2019)
W1-W4	1.6	49.3	-	VLA (1995)
W	1.48	100 ± 15	35	VLA(1991)

Notes: The components W1-W4 and W denotes the loop structure to the west (different labelling), and are reported in these papers Baan et al. (2007) and Colbert et al. (1994), respectively.

The emission of the loop structure seen in figure 3.2, exhibit a flux density of 110 mJy with a peak value of 38.6 mJy, giving a total luminosity of 1.45×10^{23} W Hz^{-1}, again in agreement with the findings of Colbert et al. (1994). Colbert et al. (1994) obtained a flux density of 100 mJy with a peak value of 35 mJy beam^{-1} for the loop structure. Whereas, at 1.6 GHz, Baan et al. (2007) found the flux density of the loop structure to be 49.3 mJy without any sharp peak value, suggesting that higher resolution may filter out the flux in the radio map. These comparisons are tabulated in table 4.1.

4.4.1 The western arm correlated with the optical and X-ray features

The spatial correlation (and anti-correlation) between the radio, optical and X-ray features (see figure 3.3 above), clearly illustrates that the filaments of the ionized Hα bubble permeate more to the southwest, southeast and south, all of them spreading out to the west of the radio loop structure and the extended structure below the nucleus of the southern galaxy, further supporting what Colbert et al. (1994) proposed regarding the origin of the loop structure to the west. The HST image shows the details of the superwind associated with the radio loop structure continuum to the west of NGC 6240, and consistent with the sub-arcsecond-resolution images reported by Gerssen et al. (2004). Müller-Sánchez et al. (2018) reported that the emission from the Hα bubbles to both the east and west of the nuclei, appears not to coincide with stellar continuum, implying that the bubbles originate from winds rather than tidal debris. Furthermore, the faint emission in the optical image coinciding with the radio diffuse clumps in the loop suggest that this diffuse clumps do not result from a local, off-nuclear starburst (Colbert et al., 1994). Evidently, the large-scale Hα structure towards the west, matches and complements the radio loop structure to the west, consistent with the results of Colbert et al. (1994) and Max et al. (2005).

Figures 3.4 and 3.5 show that most of the soft X-ray emission spatially correlates with the filaments of the Hα, exhibiting emission of two huge filaments that are orthogonal to the galactic plane with an extent of $\sim$ 6.5 kpc at $\sim 60°$ (Lira et al., 2002). The morphology of the bubble mainly rises from the northern filament, while the eastern side exhibits a morphology that is unclearly defined but composed of higher surface brightness and likely to result from more dense surrounding medium which decelerate and redirects the outflowing wind (Lira et al., 2002), which forms part of the [O III] cone powered by the AGN-driven outflow, reported by Müller-Sánchez et al. (2018). Clearly, the X-ray contours in figure 3.5 coincide very well with the Hα structures, and most of the soft X-ray emission follow most of the filaments in Hα bubble, while weak emission is seen on the southern filament, in agreement with the results of Lira et al. (2002), where they infer that the weak emission could be due to the presence of the dust lane. With the latter correlation between the optical and X-ray features, the most interesting part is that of the radio emission in relation to the two.

In figure 3.5, we overlaid our MeerKAT radio emission contours to the latter bands, the contours represent a synchrotron radio source along the loop structure to the west with a flux density of 110 mJy (see table 4.1). The loop structure directly aligns with the bubble seen in both the HST and Chandra image, and seems to be situated towards the upper region of the bubble(s), confirming the results of Lira et al. (2002), drawn out from the crude positional information from Figure 3(a) in Colbert et al. (1994). Furthermore, Lira et al. (2002) reported that the flux ratio of NGC 6240's bubble, from Hα to X-ray is about 1.2, consistent with the ratios determined by Strickland et al. (2002) for the different regions of the galactic wind in NGC 253. Therefore, this further supports the interpretation that the radio loop structure in NGC 6240 is caused by the galactic winds, since this bubble is associated with the radio loop structure. The correlation of optical, radio and X-ray emission in combination with the soft, thermal (Komossa et al., 2003), and non-thermal-plasma-like confirms that the extended emission seen in NGC 6240 is governed by starburst-driven superwinds emanating mainly from the southern nucleus.

Other authors have assumed that the relativistic electrons in the wind have originated from the nuclear radio cores of NGC 6240 (Colbert et al., 1994), taking this into consideration, the Hα filament seen emanating from the southern nuclear core, spreading out to the southwest of the radio loop structure could be a jet in the process of leaving the southern nuclear core. Müller-Sánchez et al. (2018) have found that the energetics of the Hα bubble are consistent with the injected energy from a star-formation episode that happened at most 9 Myr ago, and its time scale in not consistent with classic AGN flickering cycles but consistent with the age of the nuclear starburst in NGC 6240. Clearly, this mere recent activity seen closer to the nucleus is far younger than the large-scale diffuse emission reported earlier.

4.5 Summary

In this chapter, we analysed our MeerKAT results for the large-scale continuum environment of NGC 6240. The analysis begins with the calculations along with the measurements that we used to get some of the necessary quantities to help us to better understand the nature of our radio sources. These quantities include the volume occupied by the emission of the sources, the integrated radio spectral index, magnetic fields, radiative ages and radio powers of our sources. Additionally, we estimated the mass of the system, the pressure, Mach numbers and various velocities. With these calculations we were able to classify our sources, propose possible explanations of their nature and compare them to known sources in literature.

Our main source of interest is Source E, which we were able to categorize as a radio shock, phoenix and AGN relic. Using the energetics, size and location of Source E we were able to better discern its possible nature, which is likely governed by re-acceleration of fossil-plasma by merger shocks and old radio jets. However, future observations (especially at low frequencies) will help us determine the nature of Source E much better. We are in the process of obtaining further observational data on the source. For the extended diffuse emission we suggested that its nature might be that of turbulent re-acceleration model which is usually seen in halos, and we could not classify the nature of the extended diffuse emission, since we could not interpret the entire extended diffuse emission due to artefacts.

Our map consists of other interesting point sources, which have counterparts in the other bands but unfortunately we could not study them further as their redshifts are unknown. Another interesting source we focused on is the complex jet morphology of NGC 6240, commonly known as the western arm. We explored the western arm in our MeerKAT image, and compared it to its counterparts from the X-ray and optical bands, and confirmed the results proposed by prior authors. This lays the groundwork for the future multi-frequency study of the large-scale diffuse emission aided by SKA pathfinders.

Chapter 5

CONCLUSION

5.1 Summary

The aim of this thesis is to explore the large-scale environment of NGC 6240 at a lower frequency of 1.28 GHz, using the MeerKAT observing instrument. We investigate the extended radio diffuse emission around the postmerger system of NGC 6240 at a low redshift of $z = 0.0245$, and the diffuse radio sources embedded within the extended diffuse emission. This includes the radio phoenix/shock/AGN relic, and the nearby radio galaxies (discrete bright sources). In addition, we detect the complex jet morphology of NGC 6240 at 1.28 GHz.

We first present the complex jet morphology (known as western arm) of NGC 6240 at 1.28 GHz high resolution, observed with MeerKAT instrument. The complex jet morphology is then compared with the one obtained with Very Large Array (VLA) observations at 1.48 GHz and 1.6 GHz. The MeerKAT complex jet morphology image is uniform weighted with rms of 30 μJy beam^{-1}. Secondly, we present the image revealing the discovery of the extended radio continuum around NGC 6240 at 1.28 GHz. Within this extended radio continuum, we detect four radio galaxies and a new discovered diffuse radio source located in the east of the postmerger of NGC 6240. We also show the correlation between the radio emission of the loop structure to the west and the Hα bubble seen in the X-ray and optical bands.

Additionally, we compare Source E to a sample of known radio relics and radio phoenices. The inferences drawn from the plots suggest that Source E could be a potential radio shock/phoenix/AGN relic.

In Chapter 4, we provide the analysis of the newly discovered diffuse radio sources, as well as for the complex jet morphology of NGC 6240. However, we could not do a full analysis on the extended diffuse emission due to calibration issues but we do show some quantities that characterises it as a halo. Based on the physical size, geometry, energetics and location of these newly discovered diffuse radio sources, our analysis suggest that we detected a radio phoenix/shock/AGN relic. The extended diffuse emission is $\sim$ 300 kpc, with integrated flux density of $\sim$ 13 mJy, and total dark matter halo mass of $M_{200} \sim 1.1 \times 10^{11}$ $M_{\odot}$. The radio phoenix/shock/AGN relic exhibit the physical length of 107 kpc and width of 80 kpc, and a total flux density of $\sim$ 49 mJy. Both the extended diffuse emission and radio phoenix/shock/AGN relic give radio powers with order of magnitude 10^{22} W Hz^{-1}.

Our results shows that even in low mass systems, MeerKAT is capable of detecting radio halos where their formation is expected to be ultra-low due to the turbulent re-acceleration model. These results provide a spectacular demonstration of the AGN feedback: shocks propagating out to $\sim$ 145 kpc distances to re-distribute/re-energize the gas, well beyond the map baryonic distribution of gases in galaxies. The results also provide evidence that there is a high possibility of finding more sources of revived fossil plasma sources (relics) and some kind of radio shock in low mass systems, it being associated with AGN feedbacks (merger shocks and old jet shocks).

Furthermore, the extended halo is assumed to have a steep radio spectra, ranging from 1.0 - 1.8 and for the radio phoenix/shock/AGN relic we estimated an integrated spectral index of $\sim$ 2.9, suggesting the turbulent re-acceleration for the extended halo and re-acceleration of pre-existing relativistic electrons by merger shocks for radio phoenix/shock and old radio jet shocks for the AGN relic. However, major merger events are expected to supply the energy for turbulent-induced acceleration in galaxy clusters but, in the case of NGC 6240, the mass involved is three orders of magnitude smaller, indicating that the re-acceleration efficiency may unlikely generate radio emission via turbulence. This analysis calls to attention the significance of merger systems and their role in extended diffuse emissions, and we stress out that the origin of these diffuse radio sources is still puzzling to this present day.

5.2 Future work

One of the goals is to revisit the large-scale environment of NGC 6240 with the Giant Metrewave Radio Telescope (GMRT), Very Large Array (VLA) radio observations, as well as a MeerKAT UHF observation and surveys of similar objects in the low-redshift to determine how common this serendipitous discovery of a relic in low-mass dark matter halo really is.

We would like to explore the proposed merger shocks scenario for the origin of the radio relic, using radio observations that provide both high sensitivity to low surface brightness and high angular resolution at $\lesssim$ 1.4 GHz, which will permit a much comprehensive morphological study of both the extended diffuse emission and the radio relic.

As shown in subsection 4.2.3, there is a lack of extended X-ray emission detected from NGC 6240. Therefore, we would also like revisit NGC 6240 with a full resolution deep Chandra X-ray observations, which will enable us to spot the counterparts of the merger shocks and also provide temperature maps with high spatial resolution for the newly discovered extended diffuse emission and radio relic. We will also be able to see the correlation between the radio relic and the merger axis of NGC 6240.

Bibliography

Baan, W. A., Hagiwara, Y., and Hofner, P. (2007). Hiand OH absorption toward NGC 6240. *The Astrophysical Journal*, 661(1):173–184.

Bacchi, M., Feretti, L., Giovannini, G., and Govoni, F. (2003). Deep images of cluster radio halos. *Astronomy Astrophysics - ASTRON ASTROPHYS*, 400.

Bagchi, J., Jacob, J., Gopal-Krishna, Werner, N., Wadnerkar, N., Belapure, J., and Kumbharkhane, A. C. (2009). A diffuse bubble-like radio-halo source MRC 0116+111: imprint of AGN feedback in a low-mass cluster of galaxies. *Monthly Notices of the Royal Astronomical Society*, 399(2):601–614.

Barnes, J. E. and Hernquist, L. (1992). Dynamics of interacting galaxies. , 30:705–742.

Baum, S. A. and O'Dea, C. P. (1991). Multifrequency VLA observations of PKS 0745 – 191 –: the archetypal 'cooling flow' radio source? *Monthly Notices of the Royal Astronomical Society*, 250(4):737–749.

Beck, R. and Krause, M. (2005). Revised equipartition and minimum energy formula for magnetic field strength estimates from radio synchrotron observations. *Astronomische Nachrichten*, 326(6):414–427.

Behroozi, P. S., Conroy, C., and Wechsler, R. H. (2010). A comprehensive analysis of uncertainties affecting the stellar mass-halo mass relation for 0 <z< 4. *The Astrophysical Journal*, 717(1):379–403.

Bell, A. R. (1978). The acceleration of cosmic rays in shock fronts - II. , 182:443–455.

Benson, A., Bower, R., Frenk, C., Lacey, C., Baugh, C., and Cole, S. (2003). What shapes the luminosity function of galaxies? *The Astrophysical Journal*, 599(1):38–49.

Beswick, R., Pedlar, A., Mundell, C., and Gallimore, J. (2001). A MERLIN neutral hydrogen absorption study of the luminous infrared merger NGC 6240. *Monthly Notices of the Royal Astronomical Society*, 325(1):151–158.

Blasi, P. and Gabici, S. (2003). Shock Acceleration and Gamma Radiation in Clusters of Galaxies. In *International Cosmic Ray Conference*, volume 4 of *International Cosmic Ray Conference*, page 2051.

Bonafede, A., Brüggen, M., van Weeren, R., Vazza, F., Giovannini, G., Ebeling, H., Edge, A. C., Hoeft, M., and Klein, U. (2012). Discovery of radio haloes and double relics in distant macs galaxy clusters: clues to the efficiency of particle acceleration. *Monthly Notices of the Royal Astronomical Society*, 426(1):40–56.

Bonafede, A., Intema, H. T., Brüggen, M., Girardi, M., Nonino, M., Kantharia, N., van Weeren, R. J., and Röttgering, H. J. A. (2014). Evidence for Particle Reacceleration in the Radio Relic in the Galaxy Cluster PLCKG287.0+32.9. , 785(1):1.

Bonafede, A., Feretti, L., Giovannini, G., Govoni, F., Murgia, M., Taylor, G. B., Ebeling, H., Allen, S., Gentile, G., and Pihlström, Y. (2009). Revealing the magnetic field in a distant galaxy cluster: discovery of the complex radio emission from macs17.5 +3745. *A&A*, 503(3):707–720.

Borgani, S., Fabjan, D., Tornatore, L., Schindler, S., Dolag, K., and Diaferio, A. (2008). The chemical enrichment of the icm from hydrodynamical simulations. *Space Science Reviews*, 134(1-4):379–403.

Botteon, A., Cassano, R., van Weeren, R. J., Shimwell, T. W., Bonafede, A., Brüggen, M., Brunetti, G., Cuciti, V., Dallacasa, D., de Gasperin, F., and et al. (2021). Discovery of a radio halo (and relic) in a m 500 $<$ 2 $\times$ 1014 m cluster. *The Astrophysical Journal Letters*, 914(2):L29.

Botteon, A., van Weeren, R. J., Brunetti, G., de Gasperin, F., Intema, H. T., Osinga, E., Gennaro, G. D., Shimwell, T. W., Bonafede, A., Brüggen, M., and et al. (2020). A giant radio bridge connecting two clusters in abell 1758. *Monthly Notices of the Royal Astronomical Society: Letters*.

Bower, R. G., Benson, A. J., Malbon, R., Helly, J. C., Frenk, C. S., Baugh, C. M., Cole, S., and Lacey, C. G. (2006). Breaking the hierarchy of galaxy formation. , 370(2):645–655.

Bower, R. G., Lucey, J. R., and Ellis, R. S. (1992). Precision photometry of early-type galaxies in the Coma and Virgo clusters: a test of the universality of the colour–magnitude relation – II. Analysis. *Monthly Notices of the Royal Astronomical Society*, 254(4):601–613.

Bower, R. G., Schaye, J., Frenk, C. S., Theuns, T., Schaller, M., Crain, R. A., and McAlpine, S. (2016). The dark nemesis of galaxy formation: why hot haloes trigger black hole growth and bring star formation to an end. *Monthly Notices of the Royal Astronomical Society*, 465(1):32–44.

Brienza, M., Shimwell, T. W., de Gasperin, F., Bikmaev, I., Bonafede, A., Botteon, A., Brüggen, M., Brunetti, G., Burenin, R., Capetti, A., and et al. (2021). A snapshot of the oldest active galactic nuclei feedback phases. *Nature Astronomy*.

Brinchmann, J., Charlot, S., White, S. D. M., Tremonti, C., Kauffmann, G., Heckman, T., and Brinkmann, J. (2004). The physical properties of star-forming galaxies in the low-redshift universe. *Monthly Notices of the Royal Astronomical Society*, 351(4):1151–1179.

Brocksopp, C., Kaiser, C. R., Schoenmakers, A. P., and De Bruyn, A. G. (2007). Three episodes of jet activity in the Fanaroff–Riley type II radio galaxy B0925+420. *Monthly Notices of the Royal Astronomical Society*, 382(3):1019–1028.

Campbell, K. (2014). Meerkat delays likely to be of short duration. `https://www.polity.org.za/article/meerkat-delays-likely-to-be-of-short-duration-2014-07-11`.

Cantwell, T. M., Scaife, A. M. M., Oozeer, N., Wen, Z. L., and Han, J. L. (2016). A newly discovered radio halo in merging cluster MACS J2243.3-0935. *Monthly Notices of the Royal Astronomical Society*, 458(2):1803–1814.

Carilli, C. L. and Taylor, G. B. (2002). Cluster magnetic fields. *Annual Review of Astronomy and Astrophysics*, 40(1):319–348.

Cassano, R., Brunetti, G., Venturi, T., Setti, G., Dallacasa, D., Giacintucci, S., and Bardelli, S. (2008a). Revised statistics of radio halos and the reacceleration model. *A&A*, 480(3):687–697.

Cassano, R., Gitti, M., and Brunetti, G. (2008b). A morphological comparison between giant radio halos and radio mini-halos in galaxy clusters. *A&A*, 486(3):L31–L34.

Chun, K., Smith, R., Shin, J., Kim, S. S., and Raouf, M. (2020). The gas accretion history of low-mass halos within the cosmic web from cosmological simulations. *The Astrophysical Journal*, 889(2):173.

Churazov, E., Bruggen, M., Kaiser, C. R., Bohringer, H., and Forman, W. (2001). Evolution of buoyant bubbles in m87. *The Astrophysical Journal*, 554(1):261–273.

Clarke, T. E., Randall, S. W., Sarazin, C. L., Blanton, E. L., and Giacintucci, S. (2013). CHANDRAVIEW OF THE ULTRA-STEEP SPECTRUM RADIO SOURCE IN a2443: MERGER SHOCK-INDUCED COMPRESSION OF FOSSIL RADIO PLASMA? 772(2):84.

Coe, D. (2010). Dark matter halo mass profiles.

Colbert, E. J. M., Wilson, A. S., and Bland-Hawthorn, J. (1994). The Radio Emission from the Ultraluminous Far-Infrared Galaxy NGC 6240. , 436:89.

Cotton, W. D., Thorat, K., Condon, J. J., Frank, B. S., Józsa, G. I. G., White, S. V., Deane, R., Oozeer, N., Atemkeng, M., Bester, L., and et al. (2020). Hydrodynamical backflow in x-shaped radio galaxy pks 201455. *Monthly Notices of the Royal Astronomical Society*, 495(1):1271–1283.

Croston, J. H., Ineson, J., and Hardcastle, M. J. (2018). Particle content, radio-galaxy morphology, and jet power: all radio-loud agn are not equal. *Monthly Notices of the Royal Astronomical Society*, 476(2):1614–1623.

de Gasperin, F., Ogrean, G. A., van Weeren, R. J., Dawson, W. A., Brüggen, M., Bonafede, A., and Simionescu, A. (2015). Abell 1033: birth of a radio phoenix. *Monthly Notices of the Royal Astronomical Society*, 448(3):2197–2209.

de Gasperin, F., van Weeren, R. J., Brüggen, M., Vazza, F., Bonafede, A., and Intema, H. T. (2014). A new double radio relic in psz1 g096.89+24.17 and a radio relic mass–luminosity relation. *Monthly Notices of the Royal Astronomical Society*, 444(4):3130–3138.

Di Matteo, T., Springel, V., and Hernquist, L. (2005). Energy input from quasars regulates the growth and activity of black holes and their host galaxies. , 433(7026):604–607.

Dicke, R. H., Peebles, P. J. E., Roll, P. G., and Wilkinson, D. T. (1965). Cosmic Black-Body Radiation. , 142:414–419.

Donnert, J. M. F. (2011). On the diffuse non-thermal emission from galaxy clusters.

Dreher, J. and Feigelson, E. D. (1984). Rings and wiggles in hercules a. *Nature*, 308(5954):43–45.

Drury, L. O. (1983). REVIEW ARTICLE: An introduction to the theory of diffusive shock acceleration of energetic particles in tenuous plasmas. *Reports on Progress in Physics*, 46(8):973–1027.

Drury, L. O. (1991). Time-dependent diffusive acceleration of test particles at shocks. , 251:340–350.

Dunn, R. J. H., Fabian, A. C., and Taylor, G. B. (2005). Radio bubbles in clusters of galaxies. , 364(4):1343–1353.

Dwarakanath, K. S., Parekh, V., Kale, R., and George, L. T. (2018). Twin radio relics in the nearby low-mass galaxy cluster abell 168. *Monthly Notices of the Royal Astronomical Society*, 477(1):957–963.

Eckert, D., Jauzac, M., Vazza, F., Owers, M. S., Kneib, J. P., Tchernin, C., Intema, H., and Knowles, K. (2016). A shock front at the radio relic of Abell 2744. , 461(2):1302–1307.

Enβlin, T. A. and Gopal-Krishna (2001). Reviving fossil radio plasma in clusters of galaxies by adiabatic compression in environmental shock waves. , 366:26–34.

Ensslin, T., Biermann, P., Klein, U., and Kohle, S. (1997). Cluster radio relics as a tracer of shock waves of the large-scale structure formation. *Astronomy and Astrophysics*, 332.

Evans, A., Surace, J., Mazzarella, J., and Sanders, D. (2001). Molecular Gas Distribution in Double-Nucleus Ultraluminous Infrared Galaxies. In Wootten, A., editor, *Science with the Atacama Large Millimeter Array*, volume 235 of *Astronomical Society of the Pacific Conference Series*, page 313.

Fabbiano, G., Paggi, A., Karovska, M., Elvis, M., Nardini, E., and Wang, J. (2020). Revisiting the complex nuclear region of ngc 6240 with chandra. *The Astrophysical Journal*, 902(1):49.

Fabian, A. C. (1999). The obscured growth of massive black holes. , 308(4):L39–L43.

Fanaroff, B. L. and Riley, J. M. (1974). The morphology of extragalactic radio sources of high and low luminosity. , 167:31P–36P.

Feretti, L. (2002). Observational Properties of Diffuse Halos in Clusters. In Pramesh Rao, A., Swarup, G., and Gopal-Krishna, editors, *The Universe at Low Radio Frequencies*, volume 199, page 133.

Feretti, L., Brunetti, G., Giovannini, G., Govoni, F., and Setti, G. (2000). Non thermal emission from galaxy clusters: radio halos.

Feretti, L., Giovannini, G., Govoni, F., and Murgia, M. (2012). Clusters of galaxies: observational properties of the diffuse radio emission. *The Astronomy and Astrophysics Review*, 20(1).

Fyhrie, A., Glenn, J., Rangwala, N., Wheeler, J., Beck, S., and Bally, J. (2021). Molecular gas in the nuclear region of NGC 6240. *The Astrophysical Journal*, 922(2):208.

Gallimore, J. F. and Beswick, R. (2004). Parsec-scale radio structure of the double active nucleus of ngc 6240. *The Astronomical Journal*, 127(1):239–251.

Gerssen, J., van der Marel, R. P., Axon, D., Mihos, J. C., Hernquist, L., and Barnes, J. E. (2004). Hubble Space Telescope Observations of NGC 6240: A Case Study of an Ultraluminous Infrared Galaxy with Obscured Activity. , 127(1):75–89.

Gerssen, J., van der Marel, R. P., Axon, D. J., Mihos, C., Hernquist, L., and Barnes, J. E. (2001). HST Observations of NGC 6240. In Knapen, J. H., Beckman, J. E., Shlosman, I., and Mahoney, T. J., editors, *The Central Kiloparsec of Starbursts and AGN: The La Palma Connection*, volume 249 of *Astronomical Society of the Pacific Conference Series*, page 665.

Giacintucci, S., Markevitch, M., Brunetti, G., ZuHone, J. A., Venturi, T., Mazzotta, P., and Bourdin, H. (2014). Mapping the particle acceleration in the cool core of the galaxy cluster rx j1720.1+2638. *The Astrophysical Journal*, 795(1):73.

Giacintucci, S., Venturi, T., Brunetti, G., Dallacasa, D., Mazzotta, P., Cassano, R., Bardelli, S., and Zucca, E. (2009). Testing the radio halo-cluster merger scenario. The case of RXC J2003.5-2323. , 505(1):45–53.

Giacintucci, S., Venturi, T., Cassano, R., Dallacasa, D., and Brunetti, G. (2009). A giant radio halo in the massive and merging cluster abell 1351. *The Astrophysical Journal*, 704(1):L54–L57.

Giacintucci, S., Venturi, T., Macario, G., Dallacasa, D., Brunetti, G., Markevitch, M., Cassano, R., Bardelli, S., and Athreya, R. (2008). Shock acceleration as origin of the radio relic in a521? *Astronomy Astrophysics*, 486(2):347–358.

Giovannini, G. and Feretti, L. (2000). Halo and relic sources in clusters of galaxies. *New Astronomy*, 5:335–347.

Gitti, M., Ferrari, C., Domainko, W., Feretti, L., and Schindler, S. (2007). Discovery of diffuse radio emission at the center of the most x-ray-luminous cluster rx j1347.5-1145. *Astronomy Astrophysics*, 470(3):L25–L28.

Gitti, M., Tozzi, P., Brunetti, G., Cassano, R., Dallacasa, D., Edge, A., Ettori, S., Feretti, L., Ferrari, C., Giacintucci, S., Giovannini, G., Hogan, M., and Venturi, T. (2014). The ska view of cool-core clusters: evolution of radio mini-halos and agn feedback.

Gizani, N. A. B. and Leahy, J. P. (2003). A multiband study of Hercules A - II. Multifrequency Very Large Array imaging. , 342(2):399–421.

Govoni, F. and Feretti, L. (2004). Magnetic fields in clusters of galaxies. *International Journal of Modern Physics D*, 13(08):1549–1594.

Govoni, F., Feretti, L., Giovannini, G., Böhringer, H., Reiprich, T. H., and Murgia, M. (2001). Radio and x-ray diffuse emission in six clusters of galaxies. *Astronomy &amp Astrophysics*, 376(3):803–819.

Gull, S. F. and Northover, K. J. E. (1973). Bubble Model of Extragalactic Radio Sources. , 244(5411):80–83.

Heckman, T. (1997). Starburst-Driven Outflows in Galaxies. 6:156.

Heckman, T. M., Armus, L., and Miley, G. K. (1987). Evidence for Large-Scale Winds from Starburst Galaxies. II. an Optical Investigation of Powerful Far-Infrared Galaxies. , 93:276.

Heckman, T. M., Armus, L., and Miley, G. K. (1990). On the Nature and Implications of Starburst-driven Galactic Superwinds. , 74:833.

Heywood, I. (2020). oxkat: Semi-automated imaging of MeerKAT observations.

Hirschmann, M. (2011). Co-evolution of galaxies and black holes.

Hoang, D. N., Shimwell, T. W., Stroe, A., Akamatsu, H., Brunetti, G., Donnert, J. M. F., Intema, H. T., Mulcahy, D. D., Röttgering, H. J. A., van Weeren, R. J., Bonafede, A., Brüggen, M., Cassano, R., Chyży, K. T., Enßlin, T., Ferrari, C., de Gasperin, F., Gu, L., Hoeft, M., Miley, G. K., Orrú, E., Pizzo, R., and White, G. J. (2017). Deep LOFAR observations of the merging galaxy cluster CIZA J2242.8+5301. , 471(1):1107–1125.

Hoyle, F. and Tayler, R. J. (1964). The Mystery of the Cosmic Helium Abundance. , 203(4950):1108–1110.

Ishibashi, W. and Fabian, A. C. (2012). Active galactic nucleus feedback and triggering of star formation in galaxies. *Monthly Notices of the Royal Astronomical Society*, 427(4):2998–3005.

Ishibashi, W., Fabian, A. C., and Arakawa, N. (2021). Agn-driven galactic outflows: comparing models to observations. *Monthly Notices of the Royal Astronomical Society*, 502(3):3638–3645.

Ishibashi, W., Fabian, A. C., Ricci, C., and Celotti, A. (2018). Revisiting the 'forbidden' region: AGN radiative feedback with radiation trapping. *Monthly Notices of the Royal Astronomical Society*, 479(3):3335–3342.

Jaffe, W. J. and Rudnick, L. (1979). Observations at 610 MHz of radio halos in clusters of galaxies. , 233:453–462.

Johnson, M., McLaren, J., and Overby, D. (2016). Unconventional aqueous humor outflow: A review. *Experimental Eye Research*, 158.

Jonas, J. and MeerKAT Team (2016). The MeerKAT Radio Telescope. In *MeerKAT Science: On the Pathway to the SKA*, page 1.

Juett, A. M., Sarazin, C. L., Clarke, T. E., Andernach, H., Ehle, M., Fujita, Y., Kempner, J. C., Roy, A. L., Rudnick, L., and Slee, O. B. (2008). Achandraobservation of abell 13: Investigating the origin of the radio relic. *The Astrophysical Journal*, 672(1):138–145.

Kaastra, J. S., Bykov, A. M., Schindler, S., Bleeker, J. A. M., Borgani, S., Diaferio, A., Dolag, K., Durret, F., Nevalainen, J., Ohashi, T., Paerels, F. B. S., Petrosian, V., Rephaeli, Y., Richter, P., Schaye, J., and Werner, N. (2008). Clusters of galaxies: Beyond the thermal view. *Space Science Reviews*, 134(1-4):1–6.

Kahniashvili, T., Maravin, Y., Natarajan, A., Battaglia, N., and Tevzadze, A. G. (2013). CONSTRAINING PRIMORDIAL MAGNETIC FIELDS THROUGH LARGE-SCALE STRUCTURE. 770(1):47.

Kang, H. and Ryu, D. (2011). Re-acceleration of non-thermal particles at weak cosmological shock waves. *The Astrophysical Journal*, 734(1):18.

Kang, H. and Ryu, D. (2016). RE-ACCELERATION MODEL FOR RADIO RELICS WITH SPECTRAL CURVATURE. 823(1):13.

Kang, H., Ryu, D., and Jones, T. W. (2012). Diffusive shock acceleration simulations of radio relics. *The Astrophysical Journal*, 756(1):97.

Karachentsev, I. D. and Lipovetskii, V. A. (1969). Absorbing Material in Clusters of Galaxies. , 12:909.

Kardashev, N. S. (1962). Nonstationarity of Spectra of Young Sources of Nonthermal Radio Emission. , 6:317.

Kempner, J. C., Blanton, E. L., Clarke, T. E., Enßlin, T. A., Johnston-Hollitt, M., and Rudnick, L. (2004). Conference Note: A Taxonomy of Extended Radio Sources in Clusters of Galaxies. In Reiprich, T., Kempner, J., and Soker, N., editors, *The Riddle of Cooling Flows in Galaxies and Clusters of galaxies*, page 335.

Kenyon, J. S., Smirnov, O. M., Grobler, T. L., and Perkins, S. J. (2018). CUBICAL - fast radio interferometric calibration suite exploiting complex optimization. , 478(2):2399–2415.

Knowles, K., Baker, A. J., Bond, J. R., Gallardo, P. A., Gupta, N., Hilton, M., Hughes, J. P., Intema, H., López-Caraballo, C. H., Moodley, K., Schmitt, B. L., Sievers, J., Sifón, C., and Wollack, E. (2019). GMRT 610 MHz observations of galaxy clusters in the ACT equatorial sample. *Monthly Notices of the Royal Astronomical Society*, 486(1):1332–1349.

Kollatschny, W., Weilbacher, P. M., Ochmann, M. W., Chelouche, D., Monreal-Ibero, A., Bacon, R., and Contini, T. (2020). Ngc 6240: A triple nucleus system in the advanced or final state of merging. *A&A*, 633:A79.

Komissarov, S. S. and Gubanov, A. G. (1994). Relic radio galaxies: evolution of synchrotron spectrum. , 285:27–43.

Komossa, S., Burwitz, V., Hasinger, G., Predehl, P., Kaastra, J. S., and Ikebe, Y. (2003). Discovery of a Binary Active Galactic Nucleus in the Ultraluminous Infrared Galaxy NGC 6240 Using Chandra. , 582(1):L15–L19.

Kuo, P., Hwang, C., and Ip, W. (2004). The evolution of diffuse radio sources in galaxy clusters. *The Astrophysical Journal*, 604(1):108–115.

Lira, P., Ward, M. J., Zezas, A., and Murray, S. S. (2002). Chandra HRC and HST observations of NGC 6240: resolving the active galactic nucleus and starburst. , 333(3):709–714.

Lonsdale, C. J., Farrah, D., and Smith, H. E. (2006). *Ultraluminous Infrared Galaxies*, pages 285–336. Springer Berlin Heidelberg, Berlin, Heidelberg.

Machado, R. E. G., Tissera, P. B., Lima Neto, G. B., and Sodré, L. (2018). Properties of the circumgalactic medium in simulations compared to observations. *Astronomy Astrophysics*, 609:A66.

Magliocchetti, M., Popesso, P., Brusa, M., and Salvato, M. (2018). The environmental properties of radio-emitting AGN. *Monthly Notices of the Royal Astronomical Society*, 478(3):3848–3854.

Maltby, P., Matthews, T. A., and Moffet, A. T. (1962). The radio source hercules a. *Publications of the Astronomical Society of the Pacific*, 74:277.

Markevitch, M., Govoni, F., Brunetti, G., and Jerius, D. (2005). Bow shock and radio halo in the merging cluster a520. *The Astrophysical Journal*, 627(2):733–738.

Martinez Aviles, G. (2017). Diffuse radio sources in galaxy clusters. (2017AZUR4076).

Mathews, W. G. and Brighenti, F. (2008). Energetics of x-ray cavities and radio lobes in galaxy clusters. *The Astrophysical Journal*, 685(1):128–137.

Max, C. E., Canalizo, G., Macintosh, B. A., Raschke, L., Whysong, D., Antonucci, R., and Schneider, G. (2005). The core of ngc 6240 from keck adaptive optics andhubble space telescopenicmos observations. *The Astrophysical Journal*, 621(2):738–749.

Mazzotta, P. and Giacintucci, S. (2008). Do radio core-halos and cold fronts in non-major-merging clusters originate from the same gas sloshing? *The Astrophysical Journal*, 675(1):L9–L12.

McMullin, J. P., Waters, B., Schiebel, D., Young, W., and Golap, K. (2007). CASA Architecture and Applications. In Shaw, R. A., Hill, F., and Bell, D. J., editors, *Astronomical Data Analysis Software and Systems XVI*, volume 376 of *Astronomical Society of the Pacific Conference Series*, page 127.

Mhlahlo, N., Guennou, L., and Feretti, L. (2017). Shock acceleration in the cluster of galaxies aco2163.

Miley, G. (1980). The structure of extended extragalactic radio sources. , 18:165–218.

Miley, G. K. and Perola, G. C. (1975). The Large Scale Radio Structure of NGC 1275. , 45:223.

Murgia, M., Govoni, F., Markevitch, M., Feretti, L., Giovannini, G., Taylor, G. B., and Carretti, E. (2009). Comparative analysis of the diffuse radio emission in the galaxy clusters a1835, a2029, and ophiuchus. *A&A*, 499(3):679–695.

Müller-Sánchez, F., Nevin, R., Comerford, J. M., Davies, R. I., Privon, G. C., and Treister, E. (2018). Two separate outflows in the dual supermassive black hole system ngc 6240. *Nature*, 556(7701):345–348.

Nardini, E., Wang, J., Fabbiano, G., Elvis, M., Pellegrini, S., Risaliti, G., Karovska, M., and Zezas, A. (2013). The Exceptional Soft X-Ray Halo of the Galaxy Merger NGC 6240. , 765(2):141.

Nuza, S. E., Gelszinnis, J., Hoeft, M., and Yepes, G. (2017). Can cluster merger shocks reproduce the luminosity and shape distribution of radio relics? , 470(1):240–263.

Offringa, A. R., McKinley, B., Hurley-Walker, N., Briggs, F. H., Wayth, R. B., Kaplan, D. L., Bell, M. E., Feng, L., Neben, A. R., Hughes, J. D., and et al. (2014). wsclean: an implementation of a fast, generic wide-field imager for radio astronomy. *Monthly Notices of the Royal Astronomical Society*, 444(1):606–619.

Ogrean, G. A., Brüggen, M., van Weeren, R., Simionescu, A., Röttgering, H., and Croston, J. H. (2011). Evidence for a merger-revived radio phoenix in MaxBCG J217.95869+13.53470. *Monthly Notices of the Royal Astronomical Society*, 414(2):1175–1182.

Paggi, A., Fabbiano, G., Nardini, E., Karovska, M., Elvis, M., and Wang, J. (2022). Dissecting the extended x-ray emission in the merging pair NGC 6240: Photoionization and winds. *The Astrophysical Journal*, 927(2):166.

Pandge, M. B., Sonkamble, S. S., Parekh, V., Dabhade, P., Parmar, A., Patil, M. K., and Raychaudhury, S. (2019). Agn feedback in galaxy groups: A detailed study of x-ray features and diffuse radio emission in ic 1262. *The Astrophysical Journal*, 870(2):62.

Parekh, V., Dwarakanath, K. S., Kale, R., and Intema, H. (2016). A study of diffuse radio sources and x-ray emission in six massive clusters. *Monthly Notices of the Royal Astronomical Society*, 464(3):2752–2765.

Parekh, V., Thorat, K., Kale, R., Hugo, B., Oozeer, N., Makhathini, S., Kleiner, D., White, S. V., Józsa, G. I. G., Smirnov, O., and et al. (2020). Meerkat's discovery of a radio relic in the bimodal merging cluster a2384. *Monthly Notices of the Royal Astronomical Society*, 499(1):404–414.

Pasquali, A., de Grijs, R., and Gallagher, J. S. (2003). On the formation of star clusters in the merger NGC 6240. *Monthly Notices of the Royal Astronomical Society*, 345(1):161–174.

Penzias, A. A. and Wilson, R. W. (1965). A Measurement of Excess Antenna Temperature at 4080 Mc/s. , 142:419–421.

Perreault, T. (2021). Calibration. `https://science.nrao.edu/facilities/vla/docs/manuals/obsguide/calibration`.

Pinzke, A., Oh, S. P., and Pfrommer, C. (2013). Giant radio relics in galaxy clusters: reacceleration of fossil relativistic electrons? *Monthly Notices of the Royal Astronomical Society*, 435(2):1061–1082.

Planck Collaboration, Ade, P. A. R., Aghanim, N., Arnaud, M., Ashdown, M., Aumont, J., Baccigalupi, C., Banday, A. J., Barreiro, R. B., Bartlett, J. G., Bartolo, N., Battaner, E., Battye, R., Benabed, K., Benoît, A., Benoit-Lévy, A., Bernard, J. P., Bersanelli, M., Bielewicz, P., Bock, J. J., Bonaldi, A., Bonavera, L., Bond, J. R., Borrill, J., Bouchet, F. R., Boulanger, F., Bucher, M., Burigana, C., Butler, R. C., Calabrese, E., Cardoso, J. F., Catalano, A., Challinor, A., Chamballu, A., Chary, R. R., Chiang, H. C., Chluba, J., Christensen, P. R., Church, S., Clements, D. L., Colombi, S., Colombo, L. P. L., Combet, C., Coulais, A., Crill, B. P., Curto, A., Cuttaia, F., Danese, L., Davies, R. D., Davis, R. J., de Bernardis, P., de Rosa, A., de Zotti, G., Delabrouille, J., Désert, F. X., Di Valentino, E., Dickinson, C., Diego, J. M., Dolag, K., Dole, H., Donzelli, S., Doré, O., Douspis, M., Ducout, A., Dunkley, J., Dupac, X., Efstathiou, G., Elsner, F., Enßlin, T. A., Eriksen, H. K., Farhang, M., Fergusson, J., Finelli, F., Forni, O., Frailis, M., Fraisse, A. A., Franceschi, E., Frejsel, A., Galeotta, S., Galli, S., Ganga, K., Gauthier, C., Gerbino, M., Ghosh, T., Giard, M., Giraud-Héraud, Y., Giusarma, E., Gjerløw, E., González-Nuevo, J., Górski, K. M., Gratton, S., Gregorio, A., Gruppuso, A., Gudmundsson, J. E., Hamann, J., Hansen, F. K., Hanson, D., Harrison, D. L., Helou, G., Henrot-Versillé, S., Hernández-Monteagudo, C., Herranz, D., Hildebrandt, S. R., Hivon, E., Hobson, M., Holmes, W. A., Hornstrup, A., Hovest, W., Huang, Z., Huffenberger, K. M., Hurier, G., Jaffe, A. H., Jaffe, T. R., Jones, W. C., Juvela, M., Keihänen, E., Keskitalo, R., Kisner, T. S., Kneissl, R., Knoche, J., Knox, L., Kunz, M., Kurki-Suonio, H., Lagache, G., Lähteenmäki, A., Lamarre, J. M., Lasenby, A., Lattanzi, M., Lawrence, C. R., Leahy, J. P., Leonardi, R., Lesgourgues, J., Levrier, F., Lewis, A., Liguori, M., Lilje, P. B., Linden-Vørnle, M., López-Caniego, M., Lubin, P. M., Macías-Pérez, J. F., Maggio, G., Maino, D., Mandolesi, N., Mangilli, A., Marchini, A., Maris, M., Martin, P. G., Martinelli, M., Martínez-González, E., Masi, S., Matarrese, S., McGehee, P., Meinhold, P. R., Melchiorri, A., Melin, J. B., Mendes, L., Mennella, A., Migliaccio, M., Millea, M., Mitra, S., Miville-Deschênes, M. A., Moneti, A., Montier, L., Morgante, G., Mortlock, D., Moss, A., Munshi, D., Murphy, J. A., Naselsky, P., Nati, F., Natoli, P., Netterfield, C. B., Nørgaard-Nielsen, H. U., Noviello, F., Novikov, D., Novikov, I., Oxborrow, C. A., Paci, F., Pagano, L., Pajot, F., Paladini, R., Paoletti, D., Partridge, B., Pasian, F., Patanchon, G., Pearson, T. J., Perdereau, O., Perotto, L., Perrotta, F., Pettorino, V., Piacentini, F., Piat, M., Pierpaoli, E., Pietrobon, D., Plaszczynski, S., Pointecouteau, E., Polenta, G., Popa, L., Pratt, G. W., Prézeau, G., Prunet, S., Puget, J. L., Rachen, J. P., Reach, W. T., Rebolo, R., Reinecke, M., Remazeilles, M., Renault, C., Renzi, A., Ristorcelli, I., Rocha, G., Rosset, C., Rossetti, M., Roudier, G., Rouillé d'Orfeuil, B., Rowan-Robinson, M., Rubiño-Martín, J. A., Rusholme, B., Said, N., Salvatelli, V., Salvati, L., Sandri, M., Santos, D., Savelainen, M., Savini, G., Scott, D., Seiffert, M. D., Serra, P., Shellard, E. P. S., Spencer, L. D., Spinelli, M., Stolyarov, V., Stompor, R., Sudiwala, R., Sunyaev, R., Sutton, D., Suur-Uski, A. S., Sygnet, J. F., Tauber, J. A., Terenzi, L., Toffolatti, L., Tomasi, M., Tristram, M., Trombetti, T., Tucci, M., Tuovinen, J., Türler, M., Umana, G., Valenziano, L., Valiviita, J., Van Tent, F., Vielva, P., Villa, F., Wade, L. A., Wandelt, B. D., Wehus, I. K., White, M., White, S. D. M., Wilkinson, A., Yvon, D., Zacchei, A., and Zonca, A. (2016). Planck 2015 results. XIII. Cosmological parameters. , 594:A13.

Pluchino, S. and Bradaschia, F. (2020). Introduction to radio interferometry. `https://www.radio2space.com/introduction-to-radio-interferometry/`.

Richard-Laferrière, A., Hlavacek-Larrondo, J., Nemmen, R. S., Rhea, C. L., Taylor, G. B., Prasow-Émond, M., Gendron-Marsolais, M., Latulippe, M., Edge, A. C., Fabian, A. C., Sanders, J. S., Hogan, M. T., and Demontigny, G. (2020). On the relation between mini-halos and AGN feedback in clusters of galaxies. , 499(2):2934–2958.

Rubinur, K., Das, M., and Kharb, P. (2019a). Searching for dual agn in galaxies with double-peaked emission line spectra using radio observations. *Monthly Notices of the Royal Astronomical Society*, 484(4):4933–4950.

Rubinur, K., Das, M., Kharb, P., and Rahne, P. T. (2019b). Understanding galaxy mergers and agn feedback with uvit. *Proceedings of the International Astronomical Union*, 15(S356):345–347.

Ryle, M. and Vonberg, D. D. (1946). Solar Radiation on 175 Mc./s. , 158(4010):339–340.

Sanders, D. B. (2001). Ultraluminous Infrared Galaxies and the Origin of QSOs. *arXiv e-prints*, pages astro–ph/0109138.

Sanders, D. B., Soifer, B. T., Elias, J. H., Madore, B. F., Matthews, K., Neugebauer, G., and Scoville, N. Z. (1988). Ultraluminous Infrared Galaxies and the Origin of Quasars. , 325:74.

Sarazin, C. L. (1999). The Energy Spectrum of Primary Cosmic-Ray Electrons in Clusters of Galaxies and Inverse Compton Emission. , 520(2):529–547.

Shulevski, A., Morganti, R., Barthel, P. D., Murgia, M., van Weeren, R. J., White, G. J., Brüggen, M., Kunert-Bajraszewska, M., Jamrozy, M., Best, P. N., and et al.

(2015). The peculiar radio galaxy 4c 35.06: a case for recurrent agn activity? *Astronomy Astrophysics*, 579:A27.

Sijbring, L. (1993). *A radio continuum and H1 line study of the Perseus Cluster.* PhD thesis. date$_submitted : 2008Rights : UniversityofGroningen.$

Slee, O. B., Roy, A. L., Murgia, M., Andernach, H., and Ehle, M. (2001). Four extreme relic radio sources in clusters of galaxies. *The Astronomical Journal*, 122(3):1172–1193.

Smirnov, O. M. (2011). Revisiting the radio interferometer measurement equation. *Astronomy &amp Astrophysics*, 527:A106.

Smith, E. J., Davis Jr., L., Jones, D. E., Coleman Jr., P. J., Colburn, D. S., Dyal, P., Sonett, C. P., and Frandsen, A. M. A. (1974). The planetary magnetic field and magnetosphere of jupiter: Pioneer 10. *Journal of Geophysical Research (1896-1977)*, 79(25):3501–3513.

Steiner, J. (2006). The origin of the universe. *Estudos Avançados*, 20:231–248.

Strickland, D. K., Heckman, T. M., Weaver, K. A., Hoopes, C. G., and Dahlem, M. (2002). Chandraobservations of ngc 253. ii. on the origin of diffuse x-ray emission in the halos of starburst galaxies. *The Astrophysical Journal*, 568(2):689–716.

Tacconi, L. J., Genzel, R., and Sternberg, A. (2020). The evolution of the star-forming interstellar medium across cosmic time. *Annual Review of Astronomy and Astrophysics*, 58(1):157–203.

Tadhunter, C. (2008). An introduction to active galactic nuclei: Classification and unification. *New Astronomy Reviews*, 52(6):227–239. Active Galactic Nuclei at the Highest Angular Resolution: Theory and Observations.

Tasse, C., Hugo, B., Mirmont, M., Smirnov, O., Atemkeng, M., Bester, L., Hardcastle, M. J., Lakhoo, R., Perkins, S., and Shimwell, T. (2018). Faceting for direction-dependent spectral deconvolution. , 611:A87.

Tecza, M., Genzel, R., Tacconi, L. J., Anders, S., Tacconi-Garman, L. E., and Thatte, N. (2000). Stellar dynamics and the implications on the merger evolution in NGC 6240. *The Astrophysical Journal*, 537(1):178–190.

van Weeren, R. J., de Gasperin, F., Akamatsu, H., Brüggen, M., Feretti, L., Kang, H., Stroe, A., and Zandanel, F. (2019). Diffuse radio emission from galaxy clusters. *Space Science Reviews*, 215(1).

van Weeren, R. J., Intema, H. T., Lal, D. V., Andrade-Santos, F., Brüggen, M., de Gasperin, F., Forman, W. R., Hoeft, M., Jones, C., Nuza, S. E., Röttgering, H. J. A., and Stroe, A. (2014). A DISTANT RADIO MINI-HALO IN THE PHOENIX GALAXY CLUSTER. *The Astrophysical Journal*, 786(2):L17.

van Weeren, R. J., Röttgering, H. J. A., Bagchi, J., Raychaudhury, S., Intema, H. T., Miniati, F., Enßlin, T. A., Markevitch, M., and Erben, T. (2009). Radio observations of ZwCl 2341.1+0000: a double radio relic cluster. , 506(3):1083–1094.

van Weeren, R. J., Röttgering, H. J. A., Brüggen, M., and Hoeft, M. (2010). Particle acceleration on megaparsec scales in a merging galaxy cluster. *Science*, 330(6002):347–349.

van Weeren, R. J., Röttgering, H. J. A., Intema, H. T., Rudnick, L., Brüggen, M., Hoeft, M., and Oonk, J. B. R. (2012). The "toothbrush-relic": evidence for a coherent linear 2-mpc scale shock wave in a massive merging galaxy cluster? *Astronomy Astrophysics*, 546:A124.

Wagoner, R. V., Fowler, W. A., and Hoyle, F. (1967). On the Synthesis of Elements at Very High Temperatures. , 148:3.

Wechsler, R. H. and Tinker, J. L. (2018). The connection between galaxies and their dark matter halos. *Annual Review of Astronomy and Astrophysics*, 56(1):435–487.

White, S. D. M. and Rees, M. J. (1978). Core condensation in heavy halos: a two-stage theory for galaxy formation and clustering. , 183:341–358.

ZuHone, J., Ehlert, K., Weinberger, R., and Pfrommer, C. (2021). Turning agn bubbles into radio relics with sloshing: modeling cr transport with realistic physics.

ZuHone, J. A., Markevitch, M., Brunetti, G., and Giacintucci, S. (2012). Turbulence and radio mini-halos in the sloshing cores of galaxy clusters. *The Astrophysical Journal*, 762(2):78.

Zwicky, F. (1957). *Morphological astronomy.*